SUPERCONDUCTING PROXIMITY EFFECT IN INAS NANOWIRES

A DISSERTATION PRESENTED
BY

WILLY CHANG

TO
THE DEPARTMENT OF PHYSICS
IN PARTIAL FULFILLMENT OF THE REQUIREMENTS
FOR THE DEGREE OF
DOCTOR OF PHILOSOPHY
IN THE SUBJECT OF

PHYSICS

HARVARD UNIVERSITY
CAMBRIDGE, MASSACHUSETTS
JUNE 2014

Professor Amir Yacoby Willy Chang
Professor Charles M. Marcus

Superconducting Proximity Effect in InAs Nanowires

Abstract

First discovered by Holm and Meissner in 1932, the superconducting proximity effect has remained a subject of experimental and theoretical interest. In recent years, it has been proposed that proximity effect in a semiconductor with large g-factor and spin-orbit coupling could lead to exotic phases of superconductivity. This thesis focuses on proximity effect in one of the prime semiconductor candidates – InAs nanowires.

The first set of experiments investigates the superconducting phase-dependent tunneling spectrum of a proximitized InAs quantum dot. We observe tunneling resonances of Andreev bound states in the Kondo regime, and induce quantum phase transitions of the quantum dot ground state with gate voltage and phase bias – the latter being the first experimental observation of its kind. An additional zero-bias peak of unknown origin is observed to coexist with the Andreev bounds states.

The second set of experiments extends upon the first with sharper tunneling resonances and an increase in the device critical field. By applying an external magnetic field, we observe spin-resolved Andreev bound states in proximitized InAs quantum dots. From the linear splitting of the tunneling resonances, we extract g-factors of 5 and 10 in two different devices.

The third set of experiments utilizes a novel type of epitaxial core-shell InAs-Al nanowire. We compare the induced gaps of these nanowires with control devices proximitized with evaporated Al films. Our results show that the epitaxial core-shell nanowires possess a much harder induced gap – up to two orders of magnitude in sub-gap conductance suppression as compared to a factor of five in evaporated control devices. This observation suggests that roughness in S-N interfaces plays a crucial role in the quality of the proximity effect.

The fourth set of experiments investigates the gate-tunability of epitaxial half-shell nanowires. In a half-shell nanowire Josephson junction, we measure the normal state resistance, maximum supercurrent, and magnetic field-dependent supercurrent interference patterns. The gate dependences of these independent experimental parameters are consistent with one another and indicate that an InAs nanowire in good ohmic contact to a thin sliver of Al retains its proximity effect and is gate-tunable.

Contents

List of Figures

Acknowledgements

When Charlie decided to move to Copenhagen towards the end of my third year in grad school, I had a choice to stay in Harvard with a new advisor, or to move with Charlie to Denmark. Faced with a mid-career decision such as this, I was naturally hesitant about my options. So I did what any person would have done, which was to seek the advice of friends, colleagues, and family. Pablo Jarillo-Herrero, whom I've known since my days at Columbia, said to me "Well, you've lived in Asia, and you've lived in America. Now if you go to Europe, you'll be a complete man!"

Now, basic manners inhibits me from claiming to be a 'complete man', but my time in two continents have certainly gained me a thing or two. For one, I've had the tremendous privilege to work (and horse around) with two crews of colleagues. Two, it does every graduate student some good to learn how to set up a laboratory. When the old guard from Marcus lab graduated, I found myself across the Atlantic and assuming the responsibilities of maintaing capital equipment and instructing younger students on their operation. Sure, I was already proficient at operating the equipment, but I certainly did not know at that point in time, what every knob and button did. So, I did the next best thing: I pretended like I knew every nut and bolt. The funny thing is, the more I masqueraded, the more it became real knowledge. But it wasn't exactly the acting that taught me anything. It was the sense of ownership and the realization that you only had yourself and a handy manual to rely on that drives people to really learn. Charlie, for this experience, I am grateful. And if I may, without being rude or sounding like a retired know-it-all, I would tell younger and future graduate students to refrain from lamenting when given the tasks of cleaning pump oil out of bellows or crafting twenty voltage dividers. Good old elbow grease always has a thing or two to teach.

Technical skills aren't the only things I have to thank Charlie for. He inculcates amongst his students a no-nonsense-get-it-done attitude. Well, there were the youtube videos every once in a while. But we certainly went out there and got it done. It is easy to get lost in the minuscule details of experimental work that might or might not matter, and a graduate student certainly does not have the luxury of exploring every rabbit hole. Charlie would always say, "Go ballistically towards your target!" Another lesson from Charlie that I take to heart is the art of speaking. I don't know what the verbal equivalent of 'too long; didn't read' is, but I've learned that if you can't accurately convey what you want to say in one sentence and under ten seconds, no one's going to pay attention to you. Clarity, brevity, and precision are virtues in communication. This mantra is certainly applicable to group meetings where we are all guilty of occasional bouts of logorrhea. I'm still no master orator, but after five years I think I can get my message across well enough.

I would also like to thank my committee members Amir Yacoby and Bob Westervelt for putting up with my sporadic and last minute appearances at Harvard. Even in this day and age, coordinating across the Atlantic ocean can still be a challenge. Thank you for being extra accommodating. Of course, none of this would have been possible without the gallant efforts of Carolyn Moore who took care of all my logistical needs.

Next, I have to thank the Yankee crew and the Euro crew. But first of all, to Andrew Higginbotham, Ferdinand Kuemmeth, and Jess Martin, who straddled two continents with me. Higgy, for the countless hours of psychiatric counseling, and for being my partner in crime in the back streets of Copenhagen. Oh, and thanks for the McDonalds meal after I broke my finger. Ferdi, for your general quirkiness, endless brain teasers that are usually related to Bernoulli's principle, and showing everyone what it means to be a rock solid scientist. Without Jess, I don't think anyone would have made it. We'd all be unpaid and living on the streets of Vesterbro or in the hippie communes of Christiania. Her organizational skills were beyond excellent.

Angela Kou, for scouting out delicious things to eat and hence turning Boston from 'quite rubbish compared to New York' to 'passable when compared to New York'. Angie also served as co-conspirator in LISE 406 and the resident terrible shot for shooting the ceiling of a rifle range with a H&K MP5 submachine gun. I was also her freeloader when I became homeless from an electrical fire. Doug McClure, for being my mentor from the very beginning and drilling the workings of a dilution refrigerator into me. Vlad Manucharyan, my mentor in everything superconducting, and for telling me countless times "Willy, you see, superconductor hate magnetic field." Hugh Churchill, whose presence served as an anchor in the lab, and for Majorana versus Kondo discussions. Patrick Herring, for the boxing matches in the corridors. Patrick Gallagher, for fish shopping and letting me drive your Subaru WRX. Merritt Moore and Anna Shneidman for being wonderful teammates and making the initial push towards proximity effect in InAs nanowires. Of course, to Jim Medford, Christian Barthel, Maja Cassidy, Ruby Lai, Brandon Armstrong, Jason Wein, and Javad Shabani for contributing to the sense of camaraderie that was ever so prevalent in the old Marcus lab.

Now, the Euro crew. Morten Kjaegaard, for being the finest instructor in 'Copenhagen 101', and introducing dark and stormy (or was it the moscow mule?) to our favorite cocktail bar in Boston. Keep on trooping buddy. Sven Albrecht, my protégé, for relieving me of my duty, and keeping my blood pressure at appropriate levels at all times. Thomas Sand Jespersen, who is always calm and composed, for coming up with fantastic experimental ideas and being the team consultant. Peter Krogstrup, for making nanowires man. Damn good InAs nanowires, without which, I don't think I could have graduated. I have to thank Karsten Flensberg and Jens Paaske for numerous fruitful theory discussions and their wonderful sense of humor. Gediminas Kirsanskas, for more fruitful theory discussions when I don't want Karsten and Jens to learn of my ignorance, and for teaming up with me to give the inaugural combined QDev group meeting.

Mark Rudner, for your wonderful guitar and karaoke skills, especially when the song's in Mandarin. Johannes Beil, for being part of the transitional crew, holding up the fort when Jim was down, and the frequent leftist comments. Henri Suominen and Giulio Ungaretti, for all things involving dining and drinking, and random Japanese youtube videos. Marina Hesselberg, for random comedic comments and for wielding a kitchen knife in a manner that instills utmost confidence. Mingtang, for being another person who is familiar with the nuances of super-semi nanowire systems, and for being my replacement Asian in this strange, strange, Scandinavian land. Shivendra Upadhyay, for taking the AJA systems off my hands and whipping the cleanroom into shape. Without your efforts we'd might as well be picking up chips with our grubby fingers *sans* nitrile gloves. Kasper Grove-Rasmussen, for being another member of the transitional crew and for discussions on the Kondo-interpretation. Karl Peterson, for your thoughtful comments and extremely calm demeanor. You know you're a funny person if you can make Karl laugh. Christian Olsen, for showing me what I looked like when I'm hungover on a weekday. Of course, to the rest of the QDev crew for defining my experience in Copenhagen. I'm sorry, but there are simply too many of you guys to name individually.

I also have to thank a separate group of people who offered moral and social support. In most occupations, moral support is simply euphemism for 'no thanks to you'. But to a graduate student, moral and social support upholds the integrity of the mind and allows the student to retain some semblance of social etiquette. There are some dark, dark, dark times for every graduate student.

First of all, to Mikey Shulman, for being my partner in crime in the backstreets of Boston, and for sheltering me when my room burned down and I showed up at your doorstep with a chinese refugee bag full of soot covered clothes. And, in general, for being a darn good 'Bro'. I also have to thank 'Euro Haus' – Clemens Grassberger, Georg Kucsko, Camille Sindhu, Xavier Miro, Paula Accioly, and Konstantin Milbradt – for fist pumping away to Eurotrash at the inglorious Gypsy Bar. Jean Baccelli and Marie Christine Meyer, for inculcating in me a finer taste for wine and all things French and German. Mike Yee and Gairik Sachdeva, for being wonderful house mates in a wonderful apartment that doesn't spontaneously combust, unlike my previous one.

Andrew and Yingyan Tay (and now Amelia!), you may not know this, but you were an anchor for me throughout my time in graduate school. I have to thank you not only for letting me crash at your place when I visited New York, but also for giving me a sense of peace when I'm around you guys. Shirley Chen and Nick Haslett, my other set of anchors in New York, thank you for making me look at the larger picture when it comes to career options. Finally, to my friends and family back home who've put up with my incompetence at keeping in touch and tolerated me for behaving like a tourist in my home country. Thank you guys, and I'll see you in Singapore soon.

Chapter 1

Introduction

1.1 Superconductor-semiconductor systems

Superconductors and semiconductors are two classes of materials that have been subjects of intensive research. It is little wonder that they are held in such high regard. Superconductors are generally associated with dissipationless transport, the Meissner effect, and being excellent electromagnets. Semiconductors on the other hand, are associated with, and not limited to, variability in its carrier density, carrier charge polarity, effective carrier mass, g-factor, spin-orbit coupling, and a host of other material properties. By themselves, each material class is already fascinating. Together, they are even more tantalizing because of a peculiar property of superconductivity – it is contagious!

When a superconductor is placed in good electrical contact to a normal conductor, the normal conductor can take on superconducting-like qualities, such as the ability to transmit a dissipationless supercurrent and having a reduced density of states around the Fermi energy. This effect, known as the superconducting proximity effect and first observed by Holm and Meissner [1,2], offers numerous possibilities when applied to semiconductors.

More specifically, certain combinations of superconductor and semiconductor have received increasing interest from the condensed matter community. It has been proposed that coupling superconductors to topological insulators [3–5] or materials with high g-factor and spin-orbit coupling [6–10] can lead to exotic phases of superconductivity that may find application in topological quantum computation [11–17].

Needless to say, between being able to pass a supercurrent through a semiconductor to inducing p-wave superconductivity in a semiconductor, a lot of ground has to be covered. While experimental progress has been made by many teams over the past few years [18–22], the truth of the matter is, less conventional semiconductors (i.e. not Si and not GaAs) are less technologically developed, and material defects can lead to confusing experimental signatures. Moreover, imperfect proximity effect can cost a topological qubit its topological protection. My thesis work, hopefully a small contributory effort to this daunting endeavor, is thus to understand some of the fundamental characteristics of proximity effect in one of the prime semiconductor candidates – InAs nanowires.

1.2 InAs nanowires

There are numerous advantages for using InAs nanowires. First of all, they are known to possess the prerequisites for p-wave superconductivity – large g-factor [23] and large Rashba spin-orbit coupling [24–29]. The small effective mass of electrons in InAs doesn't hurt either, because it offers a certain degree of imperviousness to disorder. Second, they have been proven to be easily proximitized [30], most likely due to the presence of a surface accumulation layer that reduces the potency of any Schottky barrier between metallic leads and the surface of InAs nanowires [31, 32]. In terms of practicality, there exists an extensive library of knowledge on how to manipulate and contact these nanowires [33]. Third, these quasi-one-dimensional nanowires have the potential to become true one-dimensional conduction channels [34], thereby providing another crucial ingredient for p-wave superconductivity.

What is perhaps even more attractive about InAs nanowires comes from a recent development in materials growth by Krogstrup *et al.* InAs nanowires are commonly grown via chemical vapor deposition or molecular beam epitaxy (we use nanowires grown with the latter method). While the intrinsic structure of the nanowire crystal can be free of stacking faults and impurities, subsequent nanofabrication on these materials can adversely affect the quality of the nanowire. What Krogstrup *et al* have managed to accomplish is to grow a layer of crystalline Al – a commonly used superconductor – onto the InAs nanowire *in situ*, thereby eliminating the need to process the surface of the nanowire before proximitizing it with superconductors. The coherent and domain matched interface between S and N drastically enhances the quality of the proximity effect. Moreover, because the layer of Al can be as thin as a few nanometers, the critical parallel magnetic field of the proximitizing superconductor can be as high as 2 T [35], which, once again, satisfies another prerequisite for inducing p-wave superconductivity in the semiconductor.

1.3 Layout of the thesis

In this thesis I present the various proximity effect experiments that I have performed on InAs nanowires. I begin in Chapter 2 with a basic theoretical model of the superconducting proximity effect and relate its origins to Andreev reflection. The discussion then extends into measurable electronic transport properties of S-N and S-N-S devices. In these sections, I compare theoretical expectations with experimental data from earlier InAs nanowire devices that I have fabricated. Additional attention is then devoted to S-quantum dot-S devices (S-QD-S) because impurities in the nanowire and device imperfections tend to favor the formation of quantum dots (QD) when the carrier density is low. Many features of tunneling spectroscopy on discrete quantum dot levels can be easily confounded with signals of tunneling spectroscopy on Andreev bound states (ABS) from ballistic conductance channels. It is thus necessary to understand the mechanisms of quantum dots that are coupled to superconductors.

In Chapter 3 I detail the experimental investigation of spinful quantum dots coupled to superconducting leads. We tune the quantum dot into a strongly interacting regime where the charging energy is much larger than the superconducting pair potential and hybridization between the superconducting leads and the quantum dot is strong. This setup, also known as the Kondo regime, provides a rich insight into the interplay between charging energy that favors a doublet ground state, pair potential that favors a BCS-like singlet ground state, and Kondo correlation to the superconducting leads that favors a Yu-Shiba-Rusinov-like singlet ground state. In this system we observe three distinct zero-bias resonances. The first is understood as a quantum phase transition between the singlet and doublet ground states. The second is the emergence of a zero-bias Kondo resonance at fields larger than the critical magnetic field. The last is an additional zero-bias peak that coexists with superconductivity. Unfortunately, the origin of the last zero-bias peak remains unresolved.

Chapter 4 continues the quantum dot story with an experiment on S-QD-N devices. A few improvements were made over the previous experiment elucidated in Chapter 3 – a higher critical magnetic field and sharper tunneling resonances. These improvements allowed us observe spin-resolved ABSs in InAs nanowires. To the best of my knowledge, this is the second experimental observation of spin-split ABSs after earlier work by Lee *et al* in Ref. [36]. This observation allows us to directly measure the g-factor of our InAs nanowires.

While InAs and InSb nanowires have become the favored playground for many physicists, numerous experimental work have indicated that there remains a finite density of states within the induced gap of these semiconductors, i.e., a soft gap. The sought after property of topological protection in Majorana-based qubits can only protect if the zero energy mode is decoupled from quasiparticle states by a superconducting gap. In Chapter 5, I present experimental observations of a hard superconducting gap in novel epitaxial core-shell InAs-Al nanowires.

In Chapter 6 I focus on a specific variety of the epitaxial core-shell InAs-Al nanowires. When the shell covers only two or three facets of the hexagonal core, the InAs core retains the superconducting proximity effect but is no longer shielded by a large piece of metal from external electric fields. What this means is that it is now possible to tune the density of states in the InAs core, and hopefully to a regime where only a few and an odd number of sub-bands are occupied [37]. In this chapter I present gate dependent measurements of the supercurrent, normal state resistance, and magnetic field-dependent supercurrent interference pattern in epitaxial half-shell InAs nanowires.

As I wrap up the last of my experiments in Chapter 6, it seems rather presumptuous of me to attempt to conclude anything because I believe that these novel core-shell nanowires mark the beginning of a wide variety of experiments. So Chapter 7 will be spent on documenting a few experimental ideas that have been floating around during various meetings and discussions.

Finally, Appendices A and B detail, with as much humor and panache as I can muster upon a dry subject, the fabrication and electrical filtering techniques that I have employed in my experiments. The appendix on fabrication techniques will hopefully serve as a good reference for students who wish to pursue the way of InAs nanowires. Now, without further ado, let us begin!

Chapter 2

Superconducting Proximity Effect

2.1 Introduction

The superconducting proximity effect is a phenomenon that can be elegantly described in the language of Andreev reflection. Unfortunately, this subject is sparsely covered by Tinkham in *Introduction to Superconductivity* [38], one of the most popular textbooks on superconductivity (in fact, I can see at least one copy of the textbook on each QDev experimental setup that involves superconductors). Thankfully, there are many tutorial and review articles on the subject that I have found incredibly useful [39–42]. Another treasure trove of information can be found in Bretheau's thesis [43]. In this chapter I will briefly introduce the concepts of Andreev reflection and relate it's basic consequences to experimental observations in InAs nanowires.

2.2 BCS and BdG formalism

We begin by considering a regular s-type superconductor. Using the BCS mean-field approximation, we can write the effective Hamiltonian as

$$\begin{aligned} H = &\int dr \sum_{\sigma=\uparrow,\downarrow} \psi^\dagger_\sigma(r)\Big[\frac{p^2}{2m} - \mu + V(r)\Big]\psi_\sigma(r) \\ &+ \int dr \Big[\Delta(r)\psi^\dagger_\uparrow(r)\psi^\dagger_\downarrow(r) + \Delta^*(r)\psi_\downarrow(r)\psi_\uparrow\Big] \end{aligned} \tag{2.1}$$

, where $\psi^\dagger_\sigma(r)$ and $\psi_\sigma(r)$ are the creation and annihilation operators of an electron with spin σ and position r. The chemical potential is given by μ, $V(r)$ is the electrostatic potential, and $\Delta(r)$ is the superconducting pair potential.

We can rewrite this Hamiltonian into the Bogoliubov-de Gennes (BdG) equation by introducing a spinor field:

$$\Psi(r) = \begin{pmatrix} \psi_\uparrow(r) \\ \psi^\dagger_\downarrow(r) \end{pmatrix} \tag{2.2}$$

, which can be understood as a quasiparticle annihilation operator composed of a spin-up electron annihilation operator and a spin-down hole annihilation operator.

Eq. (2.1) then becomes

$$H = \int dr \Psi^\dagger(r) H_{BdG} \Psi(r) \tag{2.3}$$

, where

$$H_{BdG} = \begin{pmatrix} \frac{p^2}{2m} - \mu + V(r) & \Delta(r) \\ \Delta^*(r) & -\left[\frac{p^2}{2m} - \mu + V(r)\right] \end{pmatrix} \tag{2.4}$$

Now that we have the form of H_{BdG}, we can write down the Bogoliubov-de Gennes equation:

$$H_{BdG} \begin{pmatrix} u \\ v \end{pmatrix} = E \begin{pmatrix} u \\ v \end{pmatrix} \tag{2.5}$$

, where $u(r)$ and $v(r)$ are the electron and hole wavefunctions coupled via the pair potential $\Delta(r)$. For $\Delta(r) = 0$, as in a normal conductor, u and v are decoupled and the BdG equation becomes a regular single particle Hamiltonian for an electron and for a hole.

In a uniform superconductor with a constant pair potential $\Delta(r) = \Delta_0 e^{i\phi}$ and where $V(r) = 0$ ($\Delta_0 > 0$, and ϕ is the phase of the superconducting order parameter), the eigenfunctions of the BdG equation are quasiparticle plane waves of the form:

$$\begin{aligned} \varphi_k^+ &= \begin{pmatrix} u \\ v \end{pmatrix} e^{i\mathbf{k}\cdot\mathbf{r}} \\ \varphi_k^- &= \begin{pmatrix} -v^* \\ u^* \end{pmatrix} e^{i\mathbf{k}\cdot\mathbf{r}} \end{aligned} \tag{2.6}$$

The coefficients u and v are given by

$$\begin{aligned} u(r,\phi) &= e^{i\phi/2}\sqrt{\frac{1}{2}\Big(1+\frac{\hbar^2k^2/2m-\mu}{\sqrt{\Delta_0^2+(\hbar^2k^2/2m-\mu)^2}}\Big)} \\ v(r,\phi) &= e^{-i\phi/2}\sqrt{\frac{1}{2}\Big(1-\frac{\hbar^2k^2/2m-\mu}{\sqrt{\Delta_0^2+(\hbar^2k^2/2m-\mu)^2}}\Big)} \end{aligned} \tag{2.7}$$

, and the quasiparticle plane waves have eigenvalues

$$E_{k\pm} = \pm\sqrt{\Delta_0^2+(\hbar^2k^2/2m-\mu)^2} \tag{2.8}$$

Note that the wavevector $\mathbf{k}$ is only real at excitation energies above the superconducting pair potential, Δ_0. The lack of quasiparticle states at energies $|E| < \Delta_0$ is colloquially referred to as the superconducting gap.

We can derive the quasiparticle density of states, N_S, by equating it to the normal state density of states, N_N, in the relation: $N_S(E)dE = N_N(\epsilon)d\epsilon/2$, where $\epsilon = \hbar^2k^2/2m - \mu$. Assuming further that the normal density of states is constant and equal to the density of states at the Fermi level $N_N(\epsilon) = N_N(0)$ (as it is at zero temperature), we have

$$N_S(E) = \frac{1}{2}N_N(0)\begin{cases} \frac{|E|}{\sqrt{E^2-\Delta_0^2}} & \text{if } |E| > \Delta_0 \\ 0 & \text{otherwise} \end{cases} \tag{2.9}$$

As illustrated in Fig. 2.1, all negative energy eigenstates are occupied when the superconductor is in the ground state.

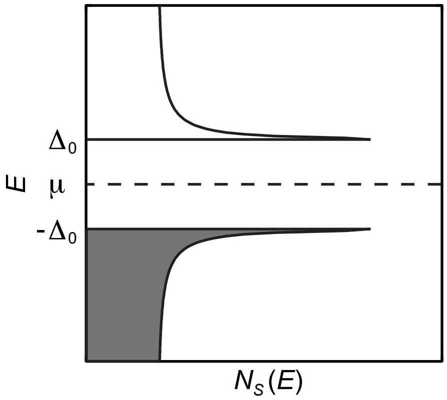

Figure 2.1: Quasiparticle density of states of a BCS superconductor. There is an absence of quasiparticle states around the Fermi level at zero temperature. All negative eigenvalue states are occupied when the superconductor is in the ground state. A minimum energy of Δ_0 is required to add or remove a single quasiparticle.

2.3 Andreev reflection

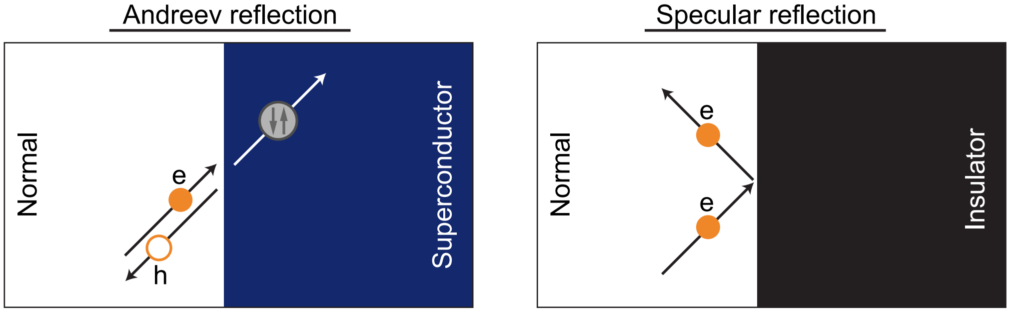

Figure 2.2: (Right panel) Regular specular reflection, where the electron scatters off a normal-insulator interface. (Left panel) Andreev reflection of an electron at the Fermi level. The electron is perfectly retro-reflected as a hole (all three components of momentum are reversed). The reflection leaves behind two electrons to form a Cooper pair in the superconductor. The process converts a dissipative current in the normal region to a supercurrent in the superconducting region.

Andreev reflection allows the conversion of a dissipative electrical current in the normal region to a dissipation-less supercurrent carried by Cooper pairs in the superconductor. The characteristics of Andreev reflection are:

1. Two-electron process: The gap in the quasiparticle spectrum of the superconductor prevents the transfer of single electronic states with $E < \Delta_0$. However,

second order processes are allowed when two electrons are transferred from the normal metal to the superconductor, thus forming a Cooper pair. The deficit of the second electron is equivalent to the reflection of the first electron as a hole.

2. Retro-reflection: The reflected hole (electron) is the time-reversed partner of the incident electron (hole). Electrons (holes) incident at the Fermi energy are perfectly retro-reflected, i.e. all three components of velocity change signs. Above the Fermi level, due to the single particle dispersion relation $E = \hbar^2 k^2/2m$, there is a wavevector mismatch between an incident electron and the reflected hole. The incident electron has energy and wavevector $(\mu + E, k_F + \delta k)$, while the reflected hole has $(\mu - E, k_F - \delta k)$, where $\delta k = E/\hbar v_F$ (we've assumed that $E \ll \mu$).

3. Phase coherent process: The reflected hole carries information on the phase of the incident electron, the macroscopic phase of the superconductor ϕ, and an energy dependent phase shift $\arccos(E/\Delta_0)$ (derived in the later parts of this section). The total phase shift is thus $\delta\phi = \phi + \arccos(E/\Delta_0)$. The extent of the proximity effect is thus largely affected by the phase coherence length of the normal metal.

4. Spin conservation: An incident spin up electron is transferred into the superconductor together with a spin down electron. Thus the reflected hole has spin up, since it represents the absence of a spin down electron.

To begin a description of Andreev reflection, we can rewrite Eqs. (2.6) and (2.7) into electron-like and hole-like solutions for the one-dimensional case (the electron/hole comparison will be obvious when one sets $\Delta_0 = 0$)

$$\begin{pmatrix} u_e \\ v_e \end{pmatrix} e^{\pm i k_e x} \qquad \begin{pmatrix} u_h \\ v_h \end{pmatrix} e^{\pm i k_h x} \tag{2.10}$$

, where the coefficients and wavevectors are now

$$\begin{aligned} u_{e,h}(\phi) &= e^{i\phi/2}\left\{\frac{1}{2}\left[1+\sigma_{e,h}\sqrt{1-\left(\frac{\Delta_0}{E}\right)^2}\right]\right\}^{1/2} \\ v_{e,h}(\phi) &= e^{-i\phi/2}\mathrm{sgn}(E)\left\{\frac{1}{2}\left[1-\sigma_{e,h}\sqrt{1-\left(\frac{\Delta_0}{E}\right)^2}\right]\right\}^{1/2} \\ k_{e,h} &= k_F\left(1+\sigma_{e,h}\mathrm{sgn}(E)\frac{\sqrt{E^2-\Delta_0^2}}{\mu}\right)^{1/2} \end{aligned} \tag{2.11}$$

Here, $\sigma_{e,h} = \pm 1$ for electron or hole, and E is the excitation energy given by Eq. (2.8) (the subscript k has been removed for simplicity).

With a little bit more algebra, the coefficients $u_{e,h}$ and $v_{e,h}$ can be written in a different way that might be more familiar to some readers. The energy dependent phase shift from Andreev reflection is also more obvious in the following format.

For $|E| < \Delta_0$,

$$\begin{aligned} u_{e,h}(\phi) &= \sqrt{\frac{\Delta_0}{2|E|}} e^{\frac{i}{2}(\phi+\sigma_{e,h}\operatorname{arccos}(E/\Delta_0))} \\ v_{e,h}(\phi) &= \operatorname{sgn}(E)\sqrt{\frac{\Delta_0}{2|E|}} e^{-\frac{i}{2}(\phi+\sigma_{e,h}\operatorname{arccos}(E/\Delta_0))} \end{aligned} \tag{2.11a}$$

and for $|E| > \Delta_0$,

$$\begin{aligned} u_{e,h}(\phi) &= \sqrt{\frac{\Delta_0}{2|E|}} e^{i\phi/2} e^{\sigma_{e,h}\operatorname{arccosh}(E/\Delta_0)/2} \\ v_{e,h}(\phi) &= \operatorname{sgn}(E)\sqrt{\frac{\Delta_0}{2|E|}} e^{-i\phi/2} e^{-\sigma_{e,h}\operatorname{arccosh}(E/\Delta_0)/2} \end{aligned} \tag{2.11b}$$

We now construct the wavefunction of an Andreev reflected electron by considering a N-S interface at $x = 0$. The superconducting order parameter is represented by $\Delta(x) = \Delta_0 e^{i\phi}\theta(x)$ where $\theta(x)$ is the Heaviside function. For the sake of simplicity, we further assume that the electron will not be specularly reflected. The simplified wavefunction is thus

$$\Psi = \left[A \begin{pmatrix} 1 \\ 0 \end{pmatrix} e^{ik_e^N x} + B \begin{pmatrix} 0 \\ 1 \end{pmatrix} e^{ik_h^N x} \right] \theta(-x) + \left[C \begin{pmatrix} u_e \\ v_e \end{pmatrix} e^{ik_e^S x} \right] \theta(x) \tag{2.12}$$

where the superscripts N and S on wavevector k denotes normal metal ($\Delta = 0$) and superconductor ($\Delta = \Delta_0 e^{i\phi}$). Enforcing continuity of the wavefunction at $x = 0$ gives $A = Cu_e$ and $B = Cv_e$. By definition, the probability of Andreev reflection is simply

$P(E) = |B/A| = |v_e/u_e|$, where the ratio between v_e and u_e is:

$$\frac{v_e}{u_e} = \begin{cases} e^{-i\phi}(E - \mathrm{sgn}(E)\sqrt{E^2 - \Delta_0^2})/\Delta_0 & |E| > \Delta_0 \\ e^{-i\phi}(E - i\sqrt{\Delta_0^2 - E^2})/\Delta_0 & |E| < \Delta_0 \end{cases} \tag{2.13}$$

$$\arg\left[\frac{v_e}{u_e}\right] = \begin{cases} \phi & E < -\Delta_0 \\ \phi + \arccos(E/\Delta_0) & |E| < \Delta_0 \\ \phi + \pi & E > \Delta_0 \end{cases} \tag{2.14}$$

In this example, the probability of Andreev is 1 when $|E| < \Delta_0$. Andreev reflection at energies smaller than the quasiparticle excitation gap also results in an energy dependent phase shift of $\arccos(E/\Delta_0)$. The energy dependent Andreev reflection probability and its corresponding phase shift is plotted in Fig. 2.3.

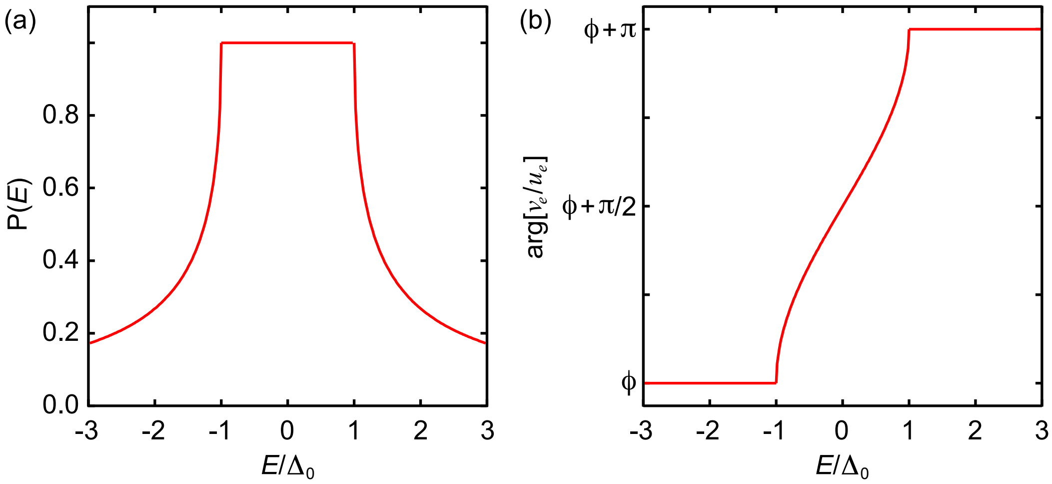

Figure 2.3: (a) Probability of Andreev reflection as a function of energy. Within the superconducting gap, there is perfect Andreev reflection. The reflection amplitude then drops rapidly once $|E|$ exceeds Δ_0. (b) Phase shift due to Andreev reflection. In addition to picking up the macroscopic superconducting phase, the reflected electron (hole) picks up an energy dependent phase shift $\arccos(E/\Delta_0)$. At the Fermi level this additional phase shift is $\pi/2$.

At sub-gap energies the wavevector in the superconducting side acquires an imaginary part and becomes an evanescent wave. Using the Andreev approximation:

$$E, \Delta_0 \ll \mu \tag{2.15}$$

we can approximate $k^S_{e,h}$ in Eq. 2.11 as

$$k_{e,h} = k_F + i\sigma_{e,h}\kappa \tag{2.16}$$

$$\kappa = k_F \frac{\sqrt{\Delta_0^2 - E^2}}{\mu} \tag{2.17}$$

Physically, κ^{-1} can be interpreted as the length scale on which the evanescent wave is damped.

The treatment of Andreev reflection at a N-S interface is greatly simplified in this example. In a realistic system, imperfections at the interface will result in a finite probability of specular reflection. For a full treatment of this problem, one would have to refer to previous work by Blonder, Tinkham, and Klapwijk in Ref. [44].

2.4 S-N-S Josephson junctions and Andreev bound states

Given that there exists a quasiparticle excitation gap, Δ, in BCS superconductors, one can imagine trapping bound states by creating two N-S interfaces around a normal metal. Following the example of Ref [41], let us consider the following one-dimensional S-N-S Josephson junction illustrated in Fig. 2.4. We assume that Andreev reflection

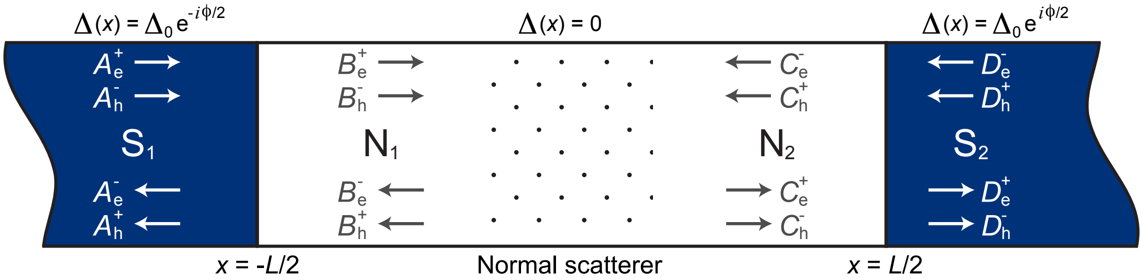

Figure 2.4: Schematic of a one-dimensional S-N-S Josephson junction. The left (S1) and right (S2) superconductors have superconducting order parameter $\Delta_0 e^{-i\phi/2}$ and $\Delta_0 e^{i\phi/2}$ respectively. The length of the normal region is L, and the two S-N interfaces are positioned such that the Josephson junction is spatially symmetric about $x = 0$. The two S-N interfaces are assumed to be perfect, i.e. the probability of Andreev reflection is unity. The normal region is split into N1 and N2 by a scatterer in the middle. The scatterer determines the transmission coefficient through the normal region and affects the Andreev bound state energy spectrum. The horizontal arrows in the figure depict left-going and right-going electron and hole wavefunctions.

is perfect at the interfaces ($x = \pm L/2$), and scattering occurs only in the disordered region in N. Treating Andreev reflection and normal scattering as spatially separated processes simplifies the problem at hand. Additionally, we want to ignore the effects of phase decoherence, so we will also assume that this is a short junction, $L < \xi_0$, where ξ_0 is the superconducting coherence length given by $\xi_0 = \hbar v_F/\Delta_0$ (v_F is the Fermi velocity).The pair potential in this case is

$$\Delta(x) = \begin{cases} \Delta_0 e^{-i\phi/2} & x < -L/2 \\ 0 & |x| < L/2 \\ \Delta_0 e^{i\phi/2} & x > L/2 \end{cases} \tag{2.18}$$

, where the macroscopic phase of each superconductor is conveniently chosen such that the superconducting phase difference across the S-N-S junction is ϕ.

In the normal region we have wavefunctions of the form (disregarding coefficients for the moment)

$$\begin{aligned}
\Psi_e^{\pm}(N_1) &= \begin{pmatrix} 1 \\ 0 \end{pmatrix} \sqrt{\frac{1}{k_e^N}} e^{\pm i k_e^N (x+L/2)} \\
\Psi_h^{\pm}(N_1) &= \begin{pmatrix} 0 \\ 1 \end{pmatrix} \sqrt{\frac{1}{k_h^N}} e^{\pm i k_h^N (x+L/2)}
\end{aligned} \tag{2.19}$$

where $k_{e,h}^N$ is given in Eq. (2.11) with $\Delta = 0$. The $+$ ($-$) superscript indicates a right (left) moving electron and a left (right) moving hole. The wavefunctions in N_2 are identical once $x + L/2$ is replaced with $x - L/2$. Similarly, we can write the wavefunctions in the superconducting region as

$$\begin{aligned}
\Psi_e^{\pm}(S_1) &= \begin{pmatrix} u_e(-\frac{\phi}{2}) \\ v_e(-\frac{\phi}{2}) \end{pmatrix} \frac{1}{\sqrt{k_e^S}} \left[1 - \left(\frac{\Delta_0}{E}\right)^2\right]^{-1/4} e^{\pm i k_e^S (x+L/2)} \\
\Psi_h^{\pm}(S_1) &= \begin{pmatrix} u_h(-\frac{\phi}{2}) \\ v_h(-\frac{\phi}{2}) \end{pmatrix} \frac{1}{\sqrt{k_h^S}} \left[1 - \left(\frac{\Delta_0}{E}\right)^2\right]^{-1/4} e^{\pm i k_h^S (x+L/2)}
\end{aligned} \tag{2.20}$$

Likewise, the wavefunction in S_2 is identical except for $-\phi/2 \to \phi/2$ and $x + L/2 \to x - L/2$. The coefficients and wavevector, $u_{e,h}(\phi)$, $v_{e,h}(\phi)$, and $k_{e,h}^S$, are defined in Eq. (2.11).

Now that we've constructed the wavefunctions in each region, let us move on to the scattering processes in the normal region and at the S-N interfaces. In the basis of the normal wavefunctions [Eq. (2.19)], we describe the incident and scattered wave by a vector of wave coefficients (also labelled in Fig. 2.4)

$$\begin{aligned}
\Psi_N^{in} &= \begin{pmatrix} B_e^+ \\ C_e^- \\ B_h^- \\ C_h^+ \end{pmatrix} \\
\Psi_N^{out} &= \begin{pmatrix} B_e^- \\ C_e^+ \\ B_h^+ \\ C_h^- \end{pmatrix}
\end{aligned} \tag{2.21}$$

We can then define a scattering matrix for the normal region, S_N, which relates the incident and scattered waves by the relation $\Psi_N^{out} = S_N \Psi_N^{in}$. S_N has the form

$$S_N = \begin{pmatrix} r_{11} & t_{12} & 0 & 0 \\ t_{21} & r_{22} & 0 & 0 \\ 0 & 0 & r_{11}^* & t_{12}^* \\ 0 & 0 & t_{21}^* & r_{22}^* \end{pmatrix} \tag{2.22}$$

Note that the 2×2 non-zero diagonal blocks of S_N are simply the unitary and symmetric s-matrices from a single-electron scattering problem.

We can also define a scattering matrix for the Andreev reflection process at the S-N interfaces ($|x| = L/2$) for $E < \Delta_0$. In this case we write $\Psi_N^{in} = S_A \Psi_N^{out}$. Assuming that the interface is ideal and no specular reflection occurs (i.e. perfect Andreev reflection), S_A takes on the form

$$S_A = e^{-i\arccos(E/\Delta_0)} \begin{pmatrix} 0 & 0 & e^{-i\phi/2} & 0 \\ 0 & 0 & 0 & e^{i\phi/2} \\ e^{i\phi/2} & 0 & 0 & 0 \\ 0 & e^{-i\phi/2} & 0 & 0 \end{pmatrix} \tag{2.23}$$

The elements of S_A are determined by matching coefficients of the wavefunctions on the N and S sides around $|x| = L/2$.

Using Eqs. (2.22) and (2.23) we arrive at the condition

$$\Psi_N^{in} = S_A S_N \Psi_N^{in} \tag{2.24}$$

which implies that

$$\mathrm{Det}(\mathbf{1} - S_A S_N) = 0 \tag{2.25}$$

, where **1** is the identity matrix. After some algebra, we arrive at the expressions

$$\mathrm{Det}[1 - E^2/\Delta_0^2 - t_{12}t_{21}^* \sin^2(\phi/2)] = 0 \tag{2.26}$$

$$E = \pm\Delta_0\sqrt{1 - \tau\sin^2(\phi/2)} \tag{2.27}$$

, where $\tau = t_{12}t_{21}^*$ is the transmission probability through the normal scatterer. The solution describes a pair of sub-gap states which we will label $|-\rangle$ for the ground state (negative energy) and $|+\rangle$ for the excited state (positive energy). When $\tau \neq 1$, the function is 2π-periodic in phase. However, in the case of perfect transmission, the spectrum of the ABS becomes $E = \pm\Delta_0 \cos(\phi/2)$, a 4π-periodic function, depicted with a dashed line in Fig. 2.5.

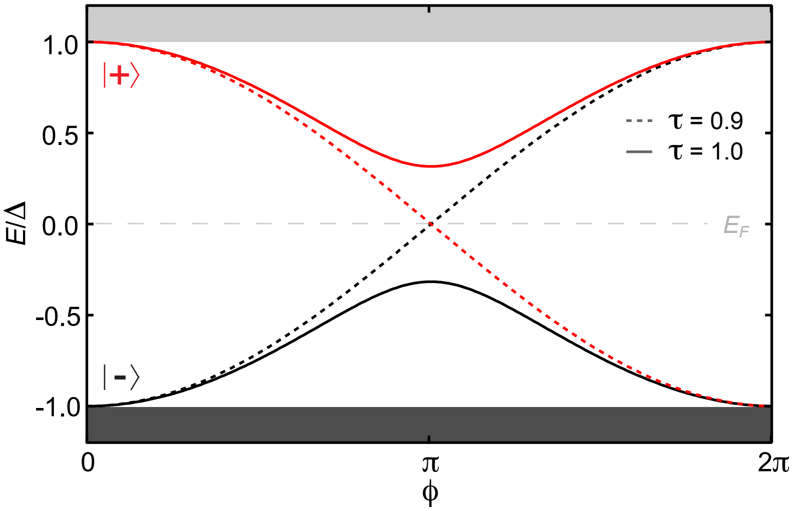

Figure 2.5: 2π-periodic phase dependent energy spectrum of Andreev bound states (ABSs). The spin degenerate ground and first excited states are labeled $|-\rangle$ and $|+\rangle$ respectively. Their energies depend on the transmission coefficient through the normal region when $\phi \neq 0 \mod (2\pi)$. In the limit of $\tau = 0$, the ABSs do not have phase dependence. In the special case of perfect transmission, the ABSs is instead described by the 4π-periodic expression $E = \pm\Delta_0 \cos(\phi/2)$. An infinitesimal deviation of the transmission coefficient from unity would double the periodicity.

So far we have considered only one conduction channel through a one-dimensional Josephson junction. A Josephson junction could have multiple transverse modes in the normal region. As long as their is no inter-modal scattering, these conduction channels are independent of each other and will each produce an orthogonal set of ABSs.

2.5 Electronic transport properties of S-N-S Josephson junctions

In this section we look at some of the basic electronic transport properties of S-N-S junctions. Fig. 2.6 shows a SEM micrograph of a typical S-InAs nanowire-S Josephson junction. The superconducting leads are evaporated Ti/Al films, and in this particular example, the junction is about 300 nm long. The device is fabricated on top of a degenerately doped Si substrate with a thermal oxide on the surface, so we can apply a global backgate, $V_{\rm BG}$, to the device.

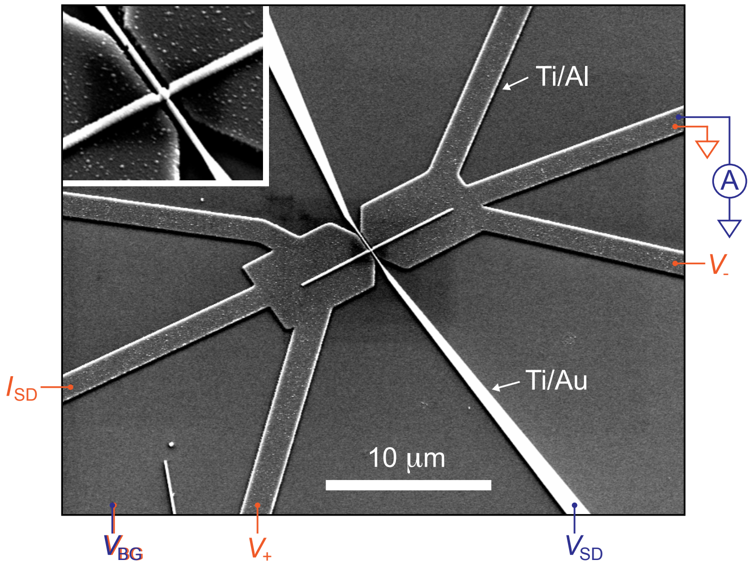

Figure 2.6: SEM micrograph of a S-InAs nanowire-S Josephson junction device. The superconducting contacts are made out of an evaporated Ti/Al film. There is an additional normal metal (Ti/Au) tunneling contact to the InAs nanowire between the superconducting contacts. Two measurement circuits are depicted in the diagram. A current bias through the S-nanowire-S junction is illustrated in orange, and a N-nanowire-S tunneling spectroscopy measurement is illustrated in blue.

An addition that is not typical of a Josephson junction is a normal metal (Ti/Au) tunnel probe in the middle of the junction (white electrode in the SEM micrograph).

This contact is a tunnel probe, and not an ohmic contact because the native oxide of the InAs nanowire is left partially intact. The oxide layer between the nanowire and the normal metal probe acts as a tunnel barrier.

Two types of measurements can be performed on this device. The first is a simple 4-probe current bias (I_{SD}), transport measurement. This measurement schematic is illustrated in orange in Fig. 2.6.

The second measurement utilizes the normal metal probe and the oxide tunnel barrier to perform direct tunneling spectroscopy of the nanowire. Here, we apply a voltage bias, V_{SD}, to the tunnel probe and measure the current through a grounded superconducting lead. The differential conductance from these measurements is directly proportional to the tunneling density of states in the nanowire. This measurement circuit is illustrated in blue in Fig. 2.6.

2.5.1 Supercurrent in short junctions

In the equilibrium state of a S-N-S Josephson junction, a zero-voltage supercurrent can flow through the normal region - this is the DC Josephson effect. The supercurrent is driven by a phase difference between the two superconducting contacts. It is 2π periodic, and it is given by the fundamental relation

$$I = \frac{2e}{\hbar}\frac{dF}{d\phi} \tag{2.28}$$

where F is the free energy of the Josephson junction. In a short junction ($L < \xi_0$) like the one discussed in the previous section, the supercurrent is carried by discrete bound states ($|-\rangle$ and $|+\rangle$), and is simply proportional to the phase derivative of the

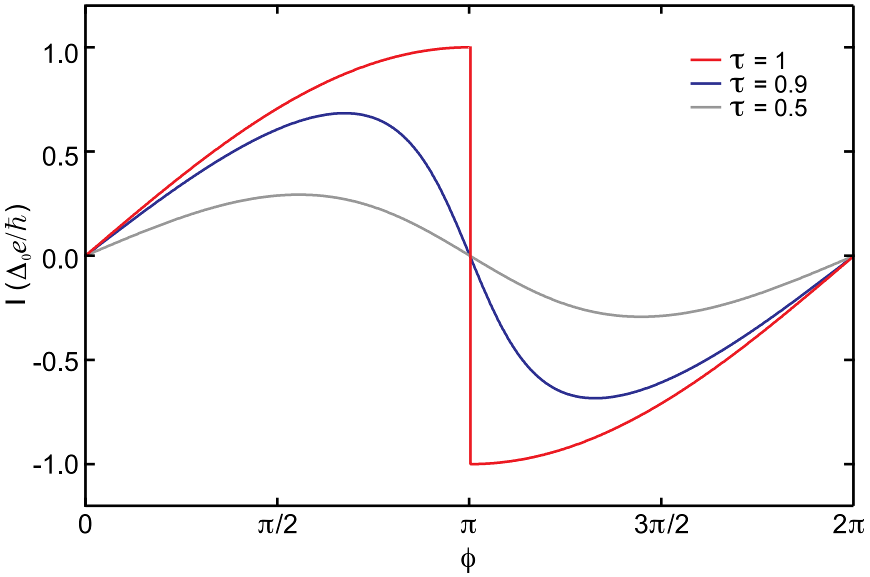

Figure 2.7: Supercurrent-phase relationship of a ground state ABS with various transmission coefficients through a short Josephson junction. When $\tau = 1$, the supercurrent is discontinuous at $\phi = \pi$. The function is smoothed out with diminishing values of τ and resembles a sinusoidal function when $\tau \ll 1$.

ABS energy

$$I = \frac{2e}{\hbar}\frac{dE}{d\phi} \tag{2.29}$$

Substituting Eq. (2.27) into Eq. (2.29), we get

$$\begin{aligned} I_{ABS,|-\rangle} &= \frac{e\Delta_0}{2\hbar}\frac{\tau\sin\phi}{\sqrt{1-\tau\sin^2(\phi/2)}} \\ I_{ABS,|+\rangle} &= -\frac{e\Delta_0}{2\hbar}\frac{\tau\sin\phi}{\sqrt{1-\tau\sin^2(\phi/2)}} \end{aligned} \tag{2.30}$$

One immediately sees that the ground state and the excited state carry supercurrents in opposite directions. At zero temperature, only the ground state is occupied, and so only it contributes to the supercurrent. However, at finite temperatures, the supercurrent depends on the thermal population and depopulation of the excited and ground states, thus modifying Eq. (2.30) by a factor of $[(1-f(E))-f(E)]$, where f is the Fermi-Dirac distribution, $f(E)=[1+\exp(E/k_{\mathrm{B}}T)]^{-1}$. The resultant supercurrent is

$$I_{ABS}=\frac{e\Delta_0}{2\hbar}\frac{\tau\sin\phi}{\sqrt{1-\tau\sin^2(\phi/2)}}\tanh\left(\frac{\Delta_0}{2k_{\mathrm{B}}T}\sqrt{1-\tau\sin^2(\phi/2)}\right) \tag{2.31}$$

We can further relate the supercurrent through a Josephson junction to its normal state conductance. In the multi-channel Landauer formalism, the normal state conductance can be expressed as

$$G_{\mathrm{N}}=\frac{2e^2}{h}\sum_{i=1}^{N}\tau_i \tag{2.32}$$

where the index i labels the transverse modes through the junction, and τ_i is the individual transmission coefficient. If the normal region of a short Josephson junction is a quantum point contact, where $\tau_i=1$ for $0<i\leq N$ and $\tau_i=0$ otherwise, Eq. (2.31) becomes

$$I(\phi)=G_{\mathrm{N}}\frac{\pi\Delta_0}{e}\sin(\phi/2)\tanh(\frac{\Delta_0}{2k_{\mathrm{B}}T}\cos(\phi/2)) \tag{2.33}$$

If, on the other hand, the normal region of the short Josephson junction is a tunnel junction with $\tau_i\ll 1$, we can approximate Eq. (2.31) as

$$I(\phi)=\frac{e\Delta_0}{2\hbar}\sum_{i=1}^{N}\tau_i\sin(\phi)\tanh(\frac{\Delta_0}{2k_{\mathrm{B}}T}) \tag{2.34}$$

Defining the critical current I_{C} as the maximum supercurrent carried across the

Josephson junction, Eq. (2.34) becomes the Ambegaokar-Baratoff formula

$$I_{\mathrm{C}}R_{\mathrm{N}} = \frac{\pi\Delta_0}{2e}\tanh(\frac{\Delta_0}{2k_{\mathrm{B}}T}) \qquad (2.35)$$

where R_{N} is the normal state resistance of the Josephson junction.

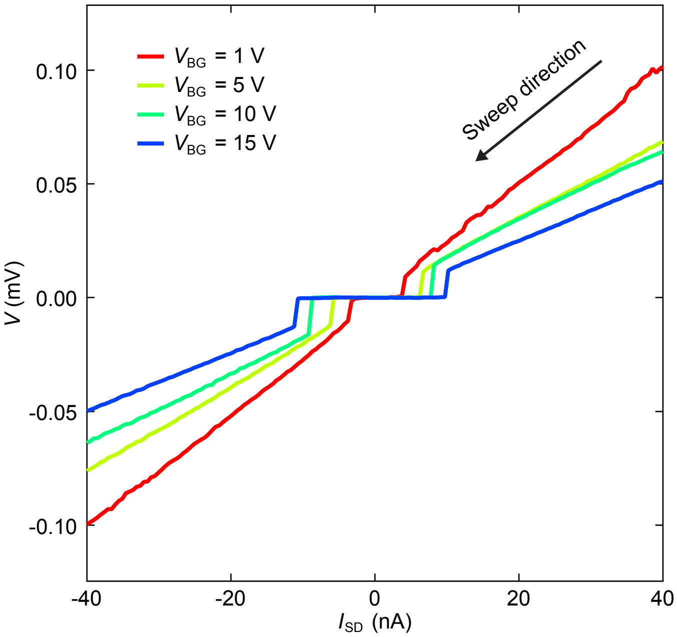

Figure 2.8: IV curves of an InAs nanowire Josephson junction at various backgate voltages.

If ‘N’ in the Josephson junction is a semiconductor, as it is for the device in Fig. 2.6, one expects a gate tunable normal state resistance, and therefore a gate tunable supercurrent. Fig. 2.8 shows four IV curves of the device taken at different backgate voltages. At the largest backgate voltage (V_{BG} = 15 V), the potential difference between the two ends of the Josephson junction is zero when the current bias is small ($|I_{\mathrm{SD}}| < 10$ nA). Above this threshold current, the IV curve switches abruptly to an IV curve of a regular Ohmic resistor. The current at which a Josephson junction switches from a resistive state to a superconducting state is conventionally referred to as the re-trapping current, I_{R}. Conversely, the current at which the junction switches from the superconducting state to a resistive state is referred to as the switching current, I_{S}.

In this particular example, the IV curves are acquired from positive to negative current bias (as indicated by the arrow in Fig. 2.8). As such, I_{S} is on the negative bias side and I_{R} is on the positive bias side. In principle, the switching and re-trapping currents are not the same as the critical current of a Josephson junction. The critical current is the theoretical limit of an ideal Josephson junction, whereas in experimental conditions the maximum supercurrent can be reduced by electrical noise, quasiparticle poisoning, and damping in the deivce. In fact, the switching and re-trapping currents need not have the same magnitude, as in an underdamped Josephson junction, where $I_{\mathrm{S}} > I_{\mathrm{R}}$ [38]. Nonetheless, I_{S} is used as a crude approximation for I_{C} in most experiments.

In Fig. 2.8, we see I_{S} and I_{R} reduce in magnitude as backgate voltage is lowered. At the same time, the gradients of the resistive branches of the IV curves increase, indicating a rising normal state resistances.

In Fig. 2.9(a), we show the differential resistance of the same device as a function of backgate voltage and current bias. Overlaid on the same graph, we plot the differential conductance of the device taken at a current bias above the supercurrent carrying branch of the Josephson junction (the data is represented by white dots and should be read off the right vertical axis). At high backgate voltages, the differential conductance of the device tracks the switching current fairly consistently. This agreement begins to deviate at lower backgate voltages below 4 V.

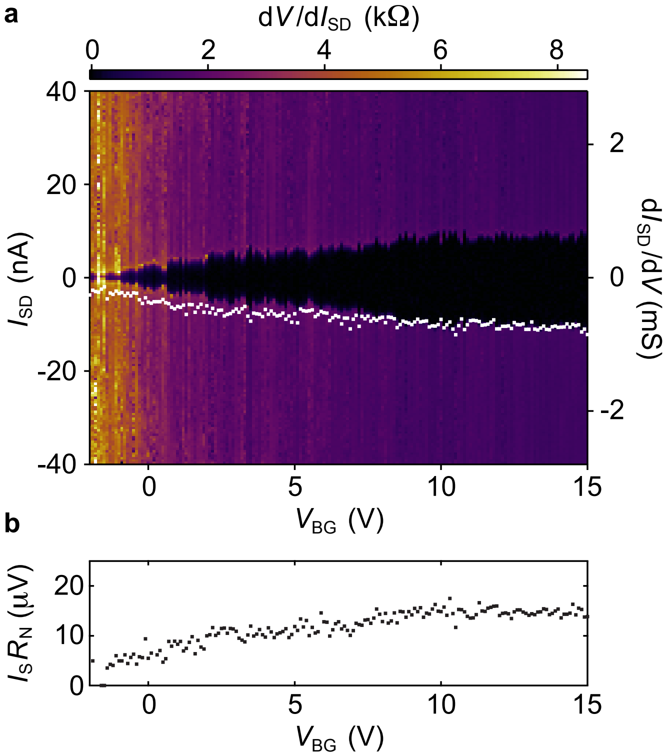

Figure 2.9: (a) Differential resistance of an InAs Josephson junction as a function of bias current and backgate voltage. The normal state differential conductance taken at high current bias is plotted against the right axis as white dots. (b) Product of the switching current and the normal state resistance, $I_S R_N$, as a function of backgate voltage.

We take the product of the switching current and the normal state resistance and plot it in Fig. 2.9(b). Once again, at higher backgate voltages, the product between the two quantities is fairly constant as V_{BG} is varied, and averages to about 14 μV. This product is considerably different from the theoretical expectation given by Eq. (2.35), with $\Delta_{Al} \sim 200$ μeV, the typical pair potential of bulk Al. However, this comparison is only valid for a ballistic S-N-S Josephson junction. The InAs nanowires used in these devices have typical elastic mean free paths of about 50 nm, significantly shorter than the junction length. As a result, the more relevant energy scale is the Thouless energy of the device, which we estimate to be $E_{Th} \sim 100$ μeV.

Furthermore, the opacity of the S-N interfaces can reduce the maximum supercurrent in a Josephson junction [45]. The characteristics of diffusive versus ballistic Josephson junctions are elaborated in greater detail in section 2.5.3. Also, considering that the switching current is only a lower bound estimate of the true critical current, it is no surprise that the product $I_{\mathrm{S}}R_{\mathrm{N}}$ is widely different from Δ_{Al}.

2.5.2 Multiple Andreev reflection - finite bias transport

A finite DC voltage across a Josephson junction will wind the phase difference across the two superconducting leads in the following manner:

$$V_{DC} = \frac{\hbar}{2e}\frac{d\phi}{dt} \tag{2.36}$$

It is evident then that the phase periodic supercurrent will oscillate and average to zero, thus making no contribution to DC electronic transport.

However, the quasiparticles in the superconducting leads can participate, and a dissipative current can flow. A quasiparticle from the left lead can tunnel into the normal region as an electron or a hole, and the electron or hole can retro-reflect at the two N-S interfaces multiple times while accumulating kinetic energy from the applied voltage bias. Each reflection transfers a charge of $2e$, until the electron/hole gains enough energy to escape into the quasiparticle excitation spectrum of the superconducting leads. This process is known as multiple Andreev reflection (MAR) [46, 47].

It is tempting to draw a cartoon similar to the one illustrated in Fig. 2.10, where the superconductors have a filled ‘valence’ band and an empty ‘conduction’ band, and the normal region has electronic states filled up to the Fermi level. However, one

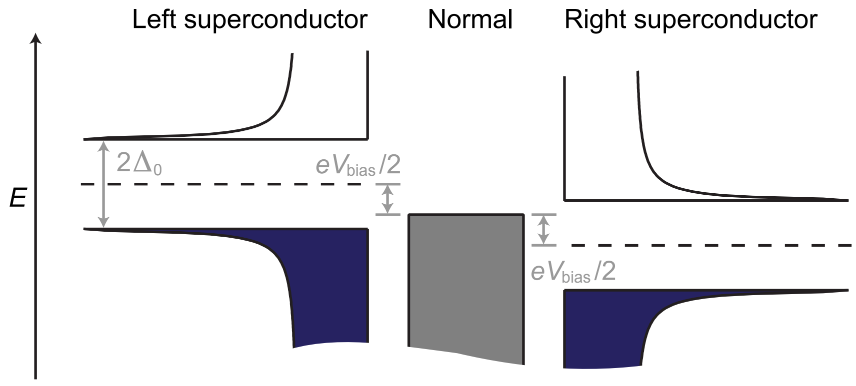

Figure 2.10: A common depiction of the density of states in a S-N-S Josephson junction. While convenient and simple, it can be misleading because the density of states diagram for the superconductor and the normal region represent two different things – quasiparticles for the former and electrons for the latter.

quickly runs into trouble because it is seemingly impossible to transfer an 'electron' from the filled valence band of left superconductor into the normal region. The problem is resolved once we recall that the BCS density of states depicted in such cartoons represent the density of states of quasiparticles, not electrons, whereas the cartoon of the normal conductor represents the density of states of electrons.

A quasiparticle tunneling from the edge of the filled negative energy states of a BCS superconductor has excitation energy Δ_0 (not $-\Delta_0$), and can become an electron or a hole in the normal conductor. Bearing this in mind, we can simplify the cartoon by removing the normal region in Fig. 2.11.

Fig. 2.11 is further simplified by leveling the chemical potential of both superconducting leads. The voltage bias across the junction is accounted for by raising the particle energy in increments of eV_{bias} every time it traverses the normal region. An n^{th} order MAR involves $(n-1)$ Andreev reflections and a transfer of charge ne. For a given voltage bias, the lowest allowed MAR order is:

$$n = \left\lceil \frac{2\Delta}{eV_{bias}} \right\rceil \tag{2.37}$$

The introduction of the next MAR mode manifests as a conductance peak in an electrical transport measurement.

While higher order process transfer more charge, their overall contribution to conduction decreases exponentially if the transmission coefficient of the junction, τ, is less than 1. An n^{th} order MAR has a transmission probability of τ^n.

In Fig. 2.12, we show the differential conductance of the device in Fig. 2.6 at finite bias voltages. When the potential difference is large, $|V| > 0.5$ mV, the differential conductance of the Josephson junction is roughly constant around 9.5 e^2/h. At smaller voltages, the differential conductance fluctuates until it reaches the superconducting state at $V = 0$. The first conductance peak occurs at $|V| = 280$ μV, and

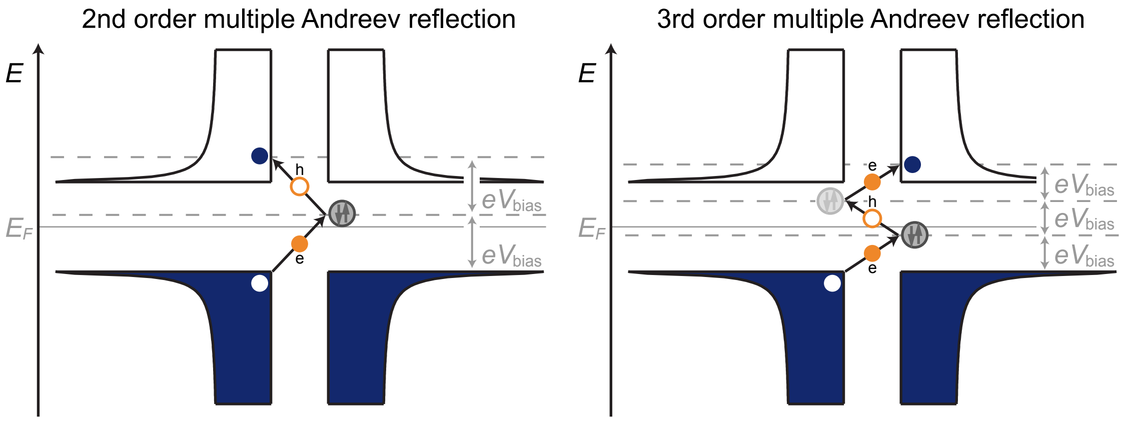

Figure 2.11: The left and right panels show a 2nd and 3rd order multiple Andreev reflection process respectively. The chemical potential of both leads are leveled. Instead, the DC voltage bias is accounted for by raising the energy of the electron/hole by eV_{bias} each time it traverses the normal region. A quasiparticle from the left lead is injected as an electron or hole in the normal region. The electron/hole then executes a series of bounces until it gains sufficient energy to overcome the superconducting gap. Each Andreev reflection adds or removes a Cooper pair from the superconducting leads.

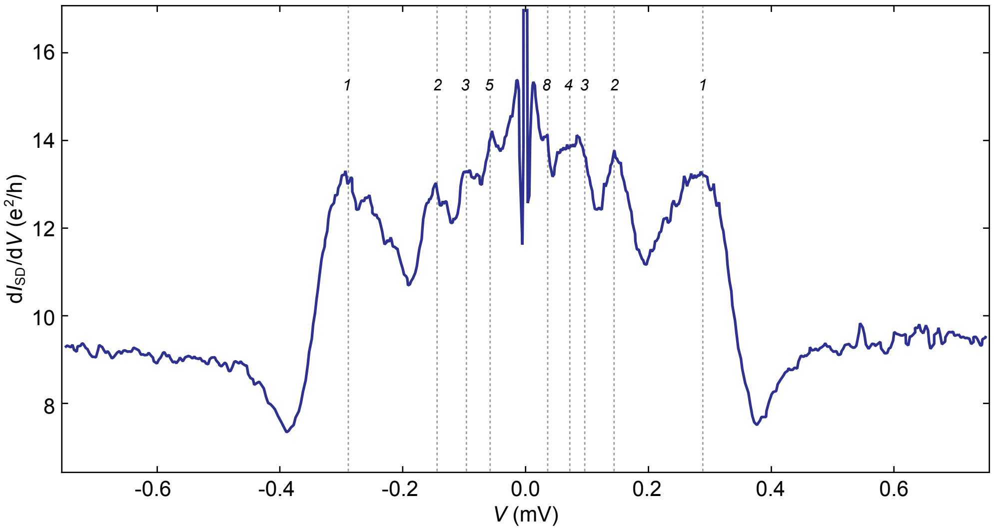

Figure 2.12: Differential conductance of an InAs Josephson junction as a function of potential difference across the junction. The first three MAR orders are recognizable as conductance peaks at voltages values of $2\Delta/en$, where n is an integer. Higher order processes are less visible and are not necessarily symmetric about zero voltage.

this conductance enhancement can be interpreted as the occurrence of the 1st order MAR. Using the relation in Eq. (2.37), we extract a superconducting pair potential of 140 μeV, and place guides (dotted vertical lines) in Fig. 2.12 to indicate the expected positions of higher order MAR conductance peaks. We find reasonable agreement between experiment and theory for the next two MAR orders. However, higher orders of MAR are not easily identified and the differential conductance signal is not symmetric about zero bias.

The absence of higher order peaks is expected of a disordered Josephson junction where τ is much smaller than 1. In the case of these devices, the scattering length in the InAs nanowire is estimated to be about 50 nm, and the junction length is 200 nm. A much better example of MAR in nanowires was demonstrated by J. Xiang *et al* in Ref. [48].

2.5.3 Tunneling spectroscopy of S-N-S junctions

In an ideal short S-N-S Josephson junction, where N is a ballistic conductor and the S-N interfaces are perfectly transparent, the density of states in the normal region is simple – a pair of Andreev bound states for each conduction channel, and their energies are given by the relation in Eq. (2.27). The normal region is populated by discrete states with energies at, or lower, than the superconductor pair potential, Δ.

However, in realistic systems, the sub-gap spectrum of the normal region is highly dependent on a variety of factors, namely the length of the junction, the elastic mean free path of N, and the interface transparency between S and N.

When the junction length is longer than the elastic mean free path, l_e, transport through the normal region becomes diffusive. This transport regime is commonly referred to as the 'dirty' limit. We can characterize diffusive transport in such a device with its diffusion coefficient, $D = l_e v_F / d$, where v_F is the Fermi velocity and d is the dimensionality of the normal region. We can also define the Thouless energy of the system, $E_{Th} = \hbar D/L^2$, where L is the length of the S-N-S junction. In the dirty limit, the S-N-S junction is best described by the quasi-classical theory developed by Eilenberger and Usadel [49, 50].

Unlike the ballistic S-N-S junction, the diffusive normal region takes on a true excitation gap, δ [51–55]. Analogous to a superconductor, there are no electronic states at energies within a $\pm\delta$ range of the Fermi level in the normal region. This gap is referred to as the minigap, since δ is smaller than Δ. In a diffusive Josephson junction, the Thouless energy, instead of the pair potential of the superconducting leads, becomes the relevant energy scale because it determines the characteristic time for an electron to travel between the S-N interfaces. It is hence expected for δ to be on the order of E_{Th}.

Thus far, the discussion has been limited to short Josephson junctions (L is smaller than the relevant phase coherence length in the system) and samples with perfect S-N interfaces. For ballistic junctions, the relevant phase coherence length is the superconducting phase coherence length of the leads, $\xi_{\mathrm{S}} = \hbar v_F/2\Delta$. For diffusive junctions, one could use the energy dependent decay length, $\xi_{\mathrm{N}} = \sqrt{\hbar D/E}$. Taking an upper limit of $E = \Delta$, this expression is simply a geometric mean of l_e and ξ_S. Since proximity effect originates from phase coherent Andreev reflections at S-N interfaces, the energy scales in the sub-gap spectrum of the normal region would decay as the length of the junction exceeds the coherence length. In addition, it has been shown theoretically that imperfect transmission through S-N interfaces can adversely affect the size of the minigap in a diffusive S-N-S junction [45].

Returning to the Josephson junction shown in Fig. 2.6, we engage the normal metal tunnel probe and investigate the excitation spectrum of the proximitized InAs nanowire. Fig. 2.13(a) shows the differential conductance of the device as a function of voltage bias, V_{SD}, and backgate voltage, V_{BG}. In the tunneling limit ($dI/dV_{\mathrm{SD}} \ll G_0 = 2e^2/h$), conductance through the tunnel probe is proportional to the density of states in the nanowire. We see that the density of states in the InAs nanowire is suppressed at small bias voltages, consistent with theoretical expectations of a minigap around the Fermi energy, and consistent with prior experimental work [56–58]. At higher bias voltages, the density of states rises, then dips again around $|V_{\mathrm{SD}}| = 200\ \mu$V. This secondary depression, symmetric about zero-bias, marks the superconducting gap of

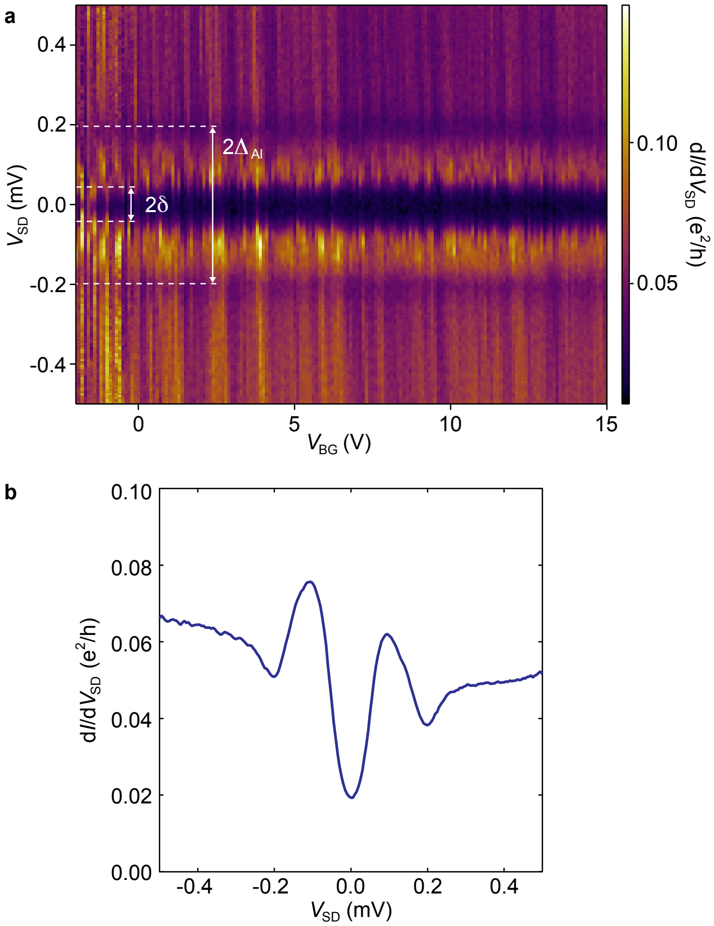

Figure 2.13: (a) Tunneling differential conductance through an InAs nanowire Josephson junction as a function of voltage bias and backgate voltage. The suppressed conductance between $|V_{\mathrm{SD}}| = \delta$ is the manifestation of a minigap in the InAs nanowire. Additional conductance dips at $|V_{\mathrm{SD}}| = 200$ mV marks the pair potential of the Al leads. (b) Differential conductance as a function of V_{SD}, averaged over multiple V_{BG} values.

the Al leads.

The size of the minigap is largely independent of V_{BG}, which tunes the chemical potential of the nanowire. This suggests that there is a high density of electrons in the InAs nanowire, and it can be treated as a 'dirty' metal. The minigap only begins to collapse at lower backgate voltages [to the left of Fig. 2.13(a)] where the nanowire begins to pinch-off. We average the differential conductance over multiple values of

V_{BG} and plot the result in Fig. 2.13(b). Using the half-width of the conductance dip around zero-bias, we estimate a minigap of 50 μeV. This value is in the same ballpark as the estimated Thouless energy of 100 μeV. It is reasonable to expect a less-than-perfect interface between the InAs nanowire and the Al leads, thereby contributing to the slight discrepancy between the two values [45]. Another deviation from theoretical expectation is the presence of a finite density of states at zero-bias. The large amount of quasiparticle states within the minigap cannot be satisfactorily explained by conventional theoretical models of inverse proximity effect and thermal excitation of quasiparticles. This observation turns out to be common amongst recent experimental systems in InAs and InSb nanowires [18–22, 59]. The origin of this 'soft' gap, and the eventual observation of a 'hard' gap in InAs nanowires, is discussed in greater detail in Chapter 5.

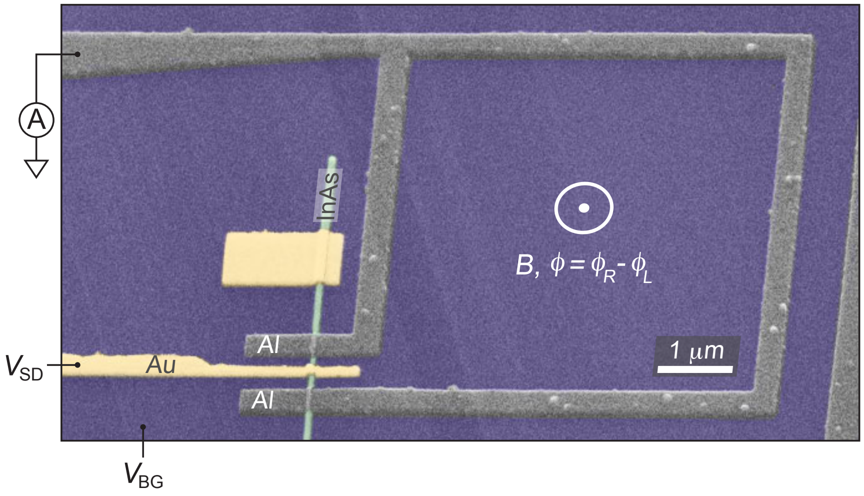

Figure 2.14: False colored SEM micrograph of an InAs Josephson junction with a normal metal tunnel probe and superconducting phase control. The superconducting contacts are Al and the normal metal tunnel probe is Au. The tunneling barrier is remnant native InAs oxide. A voltage bias is applied to the tunnel probe and the resultant current through the grounded superconducting leads is measured. Flux is applied through the 25 μm^2 loop via an external perpendicular magnetic field.

An important parameter unique to superconducting systems has been neglected so far – the superconducting phase difference, ϕ, across a S-N-S Josephson junction. In the ballistic limit, as described by Eq. (2.27), the sub-gap spectrum of the normal region is expected to be dependent on ϕ. It is not unreasonable to expect a similar phase dependence in the diffusive yet coherent transport regime. Indeed, such a phase dependence of the diffusive minigap has been predicted [60] and subsequently observed in proximitized Ag wires [61].

To explore the phase dependence of our InAs Josephson junctions, I introduce another device shown in Fig. 2.14. Similar to the previous Josephson junction, a normal metal tunnel probe contacts the InAs nanowire between two superconducting Al leads. Instead of applying a voltage or current bias across the two superconducting leads, the two leads are intentionally shorted together to form a loop (or rather, a square) of area 25 μm^2. What this geometry allows is the threading of magnetic flux through the loop, thus experimentally controlling the phase difference across the two S-N interfaces. An external perpendicular magnetic field of 72 μT corresponds to a reduced quantum of flux through the loop, $\Phi_0 = h/2e$, and subsequently corresponds to a winding of phase 2π across the junction. Once again, we apply a voltage bias to the tunnel probe and measure the differential conductance through the device in the tunneling regime.

With no external magnetic field applied to the loop, the differential conductance of the device as a function of V_{SD} and V_{BG} is shown in Fig. 2.15(a). The experimental signature is qualitatively similar to the previous device – a suppressed density of states at bias voltages of $|V_{\text{SD}}| < 70\ \mu\text{V} = \delta/e$, and a smaller one near $|V_{\text{SD}}| =$

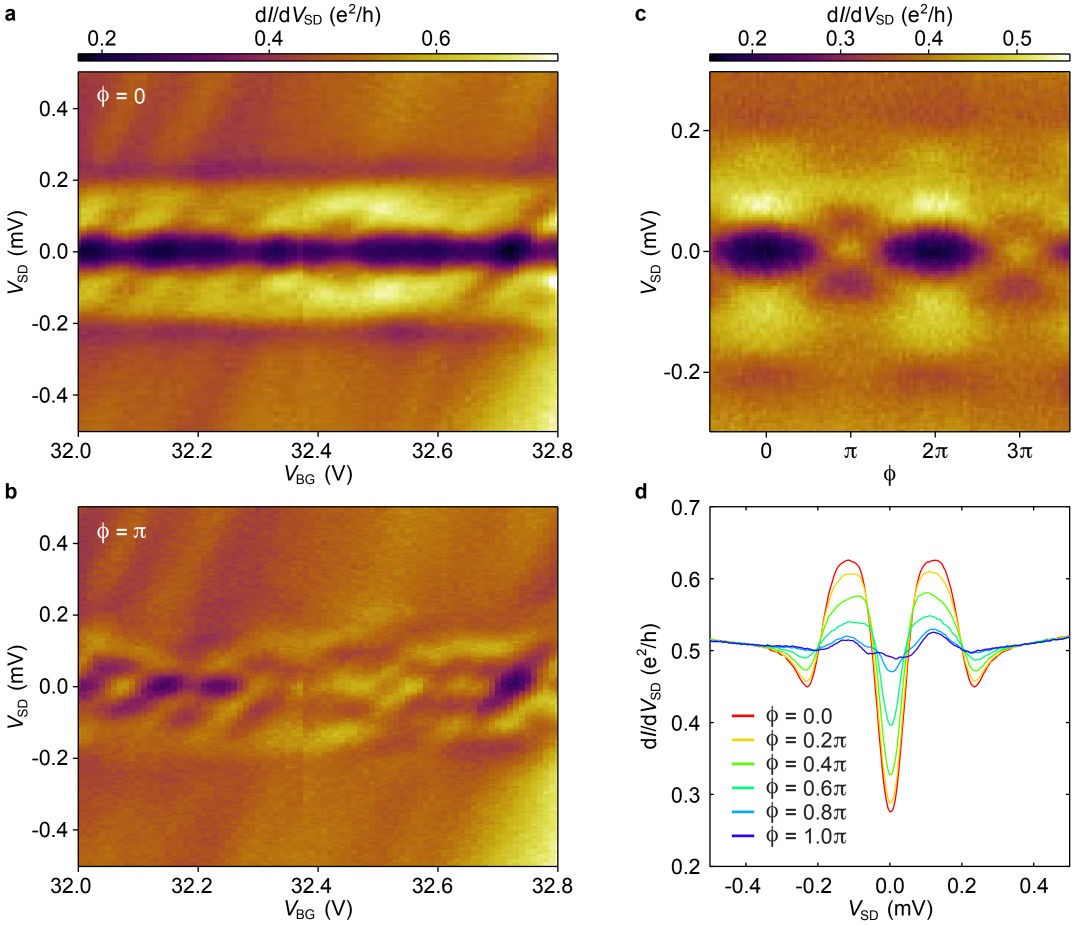

Figure 2.15: (a) and (b) Differential conductance of the proximitized nanowire as a function of V_{SD} and V_{BG} at $\phi = 0$ and at $\phi = \pi$ respectively. (c) 2π phase periodic dependence of the minigap. (d) Differential conductance at various phase values, averaged over multiple values in V_{BG}.

220 μV $= \Delta_{\mathrm{Al}}/e$. Parking V_{BG} at a fixed value, we turn on a minuscule magnetic field and measure the phase dependence of the minigap. Consistent with theoretical expectations, the minigap closes and reopens with a periodicity of 2π [Fig. 2.15(c)]. At phase $\phi = \pi$, the minigap vanishes at most backgate voltages [Fig. 2.15(b)]. Averaging across multiple values of V_{BG}, we see in Fig. 2.15(d) that the density of states near zero-bias returns to a value similar to the density of states at high biases above the superconducting gap of Al. Fig. 2.15(d) also shows the averaged traces

of other phase values. The behavior of our device is qualitatively similar to earlier experimental observations in Ag nanowires by le Sueur *et al* in Ref. [61].

Next, we examine the phase dependence of the secondary gap at $|V_{\mathrm{SD}}| = 220\ \mu\mathrm{V}$. This secondary gap is maximal at phase $\phi = 0$, and minimal at $\phi = \pi$ [see Fig. 2.15(d)], consistent with theoretical models in Ref. [62]. Also, as theory in Ref. [63] expects, this secondary gap is prominent when the Thouless energy of the device is similar to the pair potential of the superconducting leads.

2.6 Quantum dots with superconducting lead(s)

Like how proximity effect modifies the continuous spectrum of a normal conductor, the discrete spectrum of a quantum dot can take on superconducting correlations as well. In the most naive sense, one would not be wrong to expect the proximitized quantum dot to prefer to be occupied by an even number of electrons. However, the picture becomes complicated once charging energy and Kondo correlations come into play [64–67].

Following the example of Ref. [66], we can write an effective local Hamiltonian of a quantum dot coupled to one or more superconducting leads:

$$H_{\mathrm{eff}} = \sum_{\sigma} \left(\epsilon_d + \frac{U}{2} \right) d_{\sigma}^{\dagger} d_{\sigma} + \frac{U}{2} \left(\sum_{\sigma} d_{\sigma}^{\dagger} d_{\sigma} - 1 \right)^2 - \Gamma(\phi)(d_{\uparrow}^{\dagger} d_{\downarrow}^{\dagger} + \mathrm{h.c.}) \tag{2.38}$$

Here, ϵ_d is the orbital energy of the dot, U is the charging energy, d_{σ} is the annihilation operator of an electron on the dot with spin state σ, and Γ is the hybridization between the lead(s) and the dot. In the case of a quantum dot coupled to two superconducting leads, Γ is a 2π periodic function of the phase difference between the two leads: $\Gamma(\phi) = \Gamma_0 |\cos(\phi/2)|$ (assuming that the coupling to both leads are equal). The first two terms of the Hamiltonian describe a normal state isolated quantum dot with Coulomb interaction. The last term couples the quantum dot to the superconducting leads which energetically favor a double or empty occupancy of the quantum dot.

2.6.1 Large gap limit – weakly interacting quantum dot

In the large gap limit, the pair potential of the superconducting leads is the dominant energy. The charging energy of the dot is smaller than the superconducting gap, and is negligible or even zero. Coupling between the quantum dot and the superconducting leads only involves the condensate of Cooper pairs in the superconductor and not the continuous quasiparticle spectrum. In this limit, the discrete spectrum of the quantum dot is determined solely by the competition between charging energy and the superconducting gap (induced via the hybridization Γ).

We can write down the four eigenstates of H_{eff}:

$$\begin{aligned}
&|\uparrow\rangle \\
&|\downarrow\rangle \\
&|+\rangle = u\,|\uparrow\downarrow\rangle + v^*\,|\,0\rangle \\
&|-\rangle = -v^*\,|\uparrow\downarrow\rangle + u\,|\,0\rangle
\end{aligned} \tag{2.39}$$

In the absence of an external magnetic field, the two spin 1/2 states are degenerate and referred to as the magnetic doublet. The next two states are superpositions of the doubly occupied, $|\uparrow\downarrow\rangle$, and empty, $|0\rangle$, states of the quantum dot. $|+\rangle$ and $|-\rangle$ are the results of hybridization between the dot and the superconducting leads, and are referred to as the singlet states. The coefficients of their constituent states are given by:

$$\begin{aligned} u &= \frac{1}{2}\left[1 + \frac{\epsilon_d + U/2}{\sqrt{(\epsilon_d + U/2)^2 + \Gamma(\phi)^2}}\right]^{1/2} \\ v &= \frac{1}{2}\left[1 - \frac{\epsilon_d + U/2}{\sqrt{(\epsilon_d + U/2)^2 + \Gamma(\phi)^2}}\right]^{1/2} \end{aligned} \tag{2.40}$$

These four eigenstates are the Andreev bound states of a single level quantum dot, and they have energies:

$$\begin{aligned} E_{\uparrow,\downarrow} &= \epsilon_d + U/2 \\ E_{\pm} &= \epsilon_d + U \pm \sqrt{(\epsilon_d + U/2)^2 + \Gamma(\phi)^2} \end{aligned} \tag{2.41}$$

The $|-\rangle$ state is always lower in energy than the $|+\rangle$ state, and so the ground state of the quantum dot is either the magnetic doublet or the lower energy singlet. The parity of the ground state is determined by the competition between U, which prefers an odd number of electrons, and Γ, which prefers an even number of electrons. The quantum phase transition between the doublet and singlet ground states occurs at a phase boundary defined by:

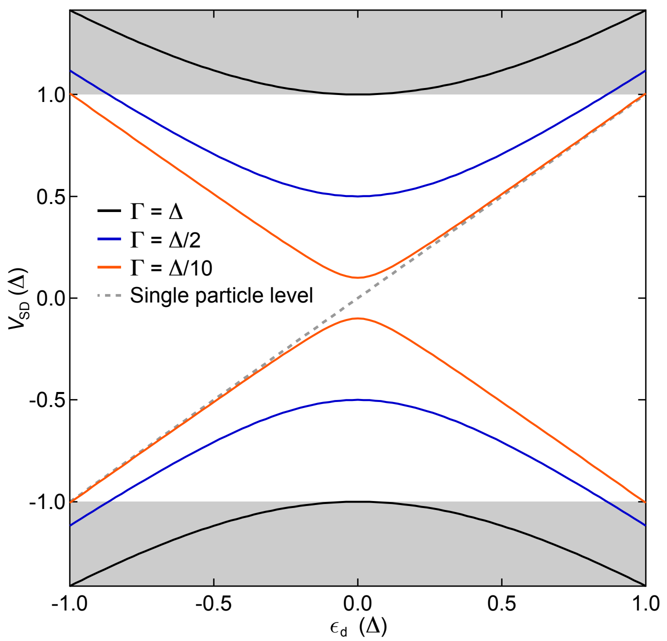

Figure 2.16: Calculated resonance levels of a quantum dot coupled to one or more superconducting leads. The normal state single particle level is represented by the gray dashed line. Orange, blue, and black lines represent the superconducting state resonance level with increasing hybridization to the superconducting leads.

$$(\epsilon_d + U/2)^2 + \Gamma(\phi)^2 = U^2/4 \tag{2.42}$$

This is known as the $0 - \pi$ transition.

It is perhaps more useful to re-express the energies of the ABSs in the framework of the addition spectrum, since tunneling spectroscopy registers energies at which an electron or hole can enter the dot. This action corresponds to a transition between states of different occupancy parity, and we can write the addition energies $\pm a$ and $\pm b$ as:

$$\begin{aligned} a &= E_- - E_{\uparrow,\downarrow} = U/2 - \sqrt{(\epsilon + U/2)^2 + \Gamma(\phi)^2} \\ b &= E_+ - E_{\uparrow,\downarrow} = U/2 + \sqrt{(\epsilon + U/2)^2 + \Gamma(\phi)^2} \end{aligned} \tag{2.43}$$

In the case of zero charging energy, the picture is very simple, and is illustrated in Fig. 2.16. Increasing coupling to the superconducting leads increases the separation between the symmetric tunneling resonances. Physically, the energy of the $|-\rangle$ ground state is lowered as hybridization with the leads increases.

We can compare this theoretical picture with experimental observation. Returning to the phase-controlled device in Fig. 2.14, we reduce the carrier density of the InAs nanowire by turning down the backgate. At magnetic fields above the critical field of the Al leads, we tune the device to a backgate region where no charging physics is evident and the tunneling conductance smoothly varies as a function of voltage bias and backgate voltage [Fig. 2.17(b)]. A zero-bias horizontal cut of the graph is superimposed, and it should be read against the right axis.

The zero-bias tunneling conductance fluctuates as a function of backgate, and we can identify four conductance peaks [indicated by colored arrows in Fig. 2.17(b)]. Four pairs of well resolved sub-gap resonances (SGRs) emerge at these conductance peak positions as magnetic field is turned off [Fig. 2.17(a)]. The four zero-bias conductance peaks in the normal state of the device can be interpreted as single particle orbitals crossing the Fermi level of the tunnel probe. The lack of Coulomb diamond resonances and even-odd structure suggests that the charging energy is negligible, if not zero. The InAs nanowire Josephson junction is thus occupied by a loosely confined quantum

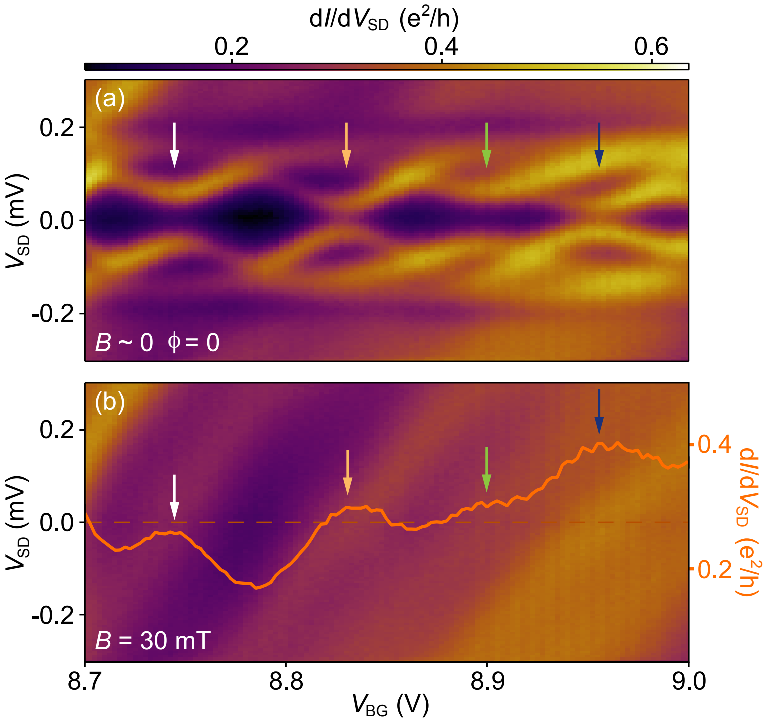

Figure 2.17: (a) Differential conductance of an InAs quantum dot in the $B = 0$ and $\phi = 0$ superconducting state. Four well-resolved pairs of tunneling resonances are identified by the colored arrows. (b) Tunneling spectrum of the quantum dot in the same bias voltage and backgate voltage range, but at $B = 30$ mT $> B_c$. Coulomb physics and even-odd structures are not evident. A zero-bias horizontal cut of the data is superimposed and read against the right axis (orange curve). Four conductance peaks in the gently undulating zero-bias trace coincide in V_{BG} position with the four pairs of tunneling resonances in the superconducting state.

dot between the two superconducting leads.

In the superconducting state, the orbitals hybridize with the superconducting leads and form singlet ground state ABSs. Their corresponding SGRs are qualitatively similar to theoretical calculations in Fig. 2.16. The fluctuating separation between the positive and negative bias resonances indicates different coupling strengths to the superconducting leads.

In Fig. 2.18 we focus on two qualitatively different ABSs. The large separation between the symmetric SGRs in the first ABS indicates a strong coupling to the superconducting leads [Fig. 2.18(a)]. When the single particle level is on resonance (by tuning V_{BG} to the point indicated by the green line), we see a strong phase modulation of the SGRs [Fig. 2.18(b)]. Specifically, the resonances meet at zero-bias when half a flux quantum is threaded through the superconducting loop. At this phase value, $\phi = \pi$, Andreev reflection between the two S-N interfaces interfere destructively and reduce the hybridization of the single particle orbital to exactly zero [for a reminder, refer to Eq. (2.43)]. This particular ABS is an example of symmetrical coupling of the single particle level to both superconducting leads.

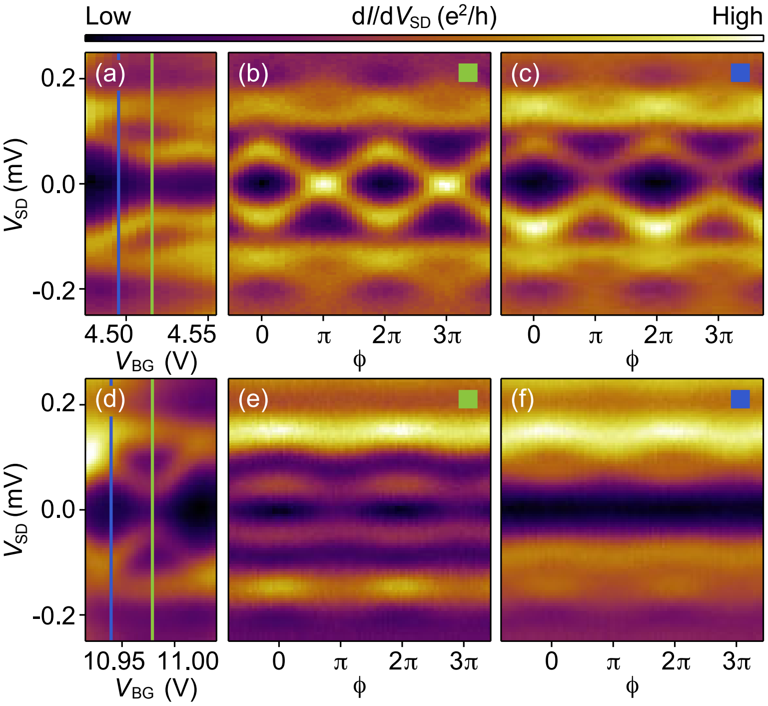

Figure 2.18: (a) and (d) Tunneling spectrum of ABSs that are symmetrically and asymmetrically coupled to the two superconducting leads. (b) and (e) Phase dependence of the corresponding ABSs when V_{BG} is on resonance with the single particle level. (c) and (f) Phase dependence of the corresponding ABSs when they are off-resonance.

When coupling to the two superconducting leads is asymmetrical, interference between the two Andreev reflection processes still reduces the total hybridization at phase π, but they don't cancel each other perfectly. As a result, the SGRs do not meet at zero-bias when the single particle level is on resonance and when $\phi = \pi$. An example can be seen in Figs. 2.18(d) – (f). In addition, this particular ABS also shows a weaker overall coupling to the leads since it has a smaller separation between the SGRs even at phase $\phi = 0$.

2.6.2 Large charging energy limit – strongly interacting quantum dot

In the large gap limit, the picture of a quantum dot coupled to superconducting leads is simple and the effective Hamiltonian can be solved analytically. This remains true even for dots with Coulomb interaction, as long as the charging energy is small ($U < \Delta$). For a quantum dot with small but finite charging energy, the ground state of the system can be the magnetic doublet, with the phase transition boundary given by Eq. (2.42). The spectrum of the quantum dot is entirely understood as a competition between the local energy scales, namely, Δ, Γ, and U. The diagram in Fig. 2.19(a) illustrates a situation where the quantum dot is tuned to the particle-hole symmetry point ($\epsilon_d + U/2 = 0$) of an odd Coulomb diamond, and $U > 2\Gamma$. The presence of the superconducting leads hybridizes the empty and doubly occupied states to form a BCS-like singlet state, $|-\rangle$.

In the opposite limit, where charging energy is large ($U > \Delta, \Gamma$), the picture becomes complicated and the effective Hamiltonian can no longer be solved analytically. Instead of forming a singlet state with the empty and doubly occupied states (which cost too much energy), the unpaired spin in the quantum dot can form Kondo-like

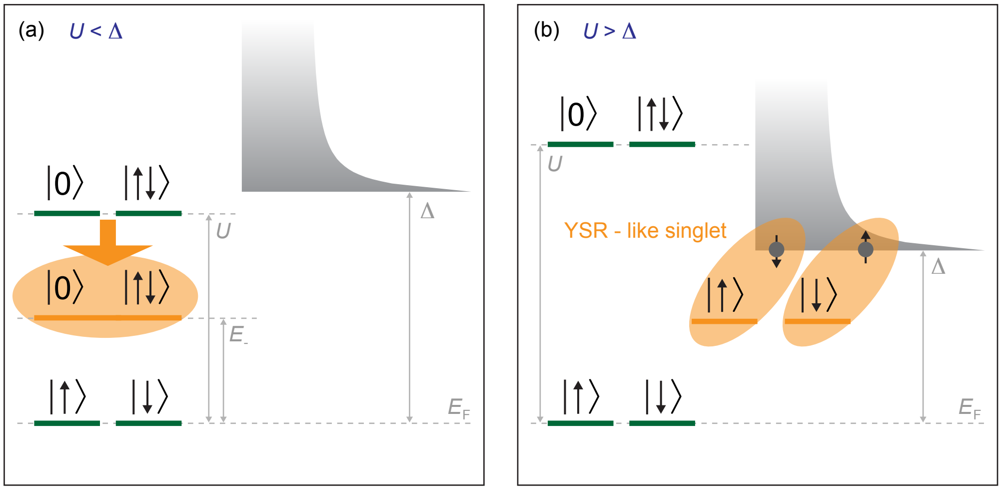

Figure 2.19: (a) Lowest energy states of a hybridized quantum dot with $U < \Delta$ (large gap limit). The first excited state is a BCS-like hybridization between the empty and doubly occupied states of a normal quantum dot. The resultant singlet state has energy $E_- < U$. (b) Lowest energy states of a hybridized quantum dot in the strong interaction limit, where $U > \Delta$. It is more energetically favorable for the magnetic doublet ground state to form singlet correlations with quasiparticles in the superconducting leads. This Yu-Shiba-Rusinov-like (YSR) singlet can be energetically competitive with the magnetic doublet to become the ground state of the system.

singlet correlations with quasiparticles in the superconducting leads [68]. In other words, the local magnetic moment in the odd parity quantum dot is screened by quasiparticles from the leads, much like a magnetic impurity embedded in a superconductor as described by Yu, Shiba, and Rusinov [69–71]. This new singlet state can have energies much lower than the superconducting gap, and modifies the conditions for the $0-\pi$ transition. The interplay between the quantum dot, the superconducting leads, and Kondo correlations is the theoretical subject of many studies [64–67], and the experimental subject of the next chapter.

Chapter 3

Tunneling Spectroscopy of Quasiparticle Bound States in a Spinful Josephson Junction

W. Chang[1,2], V. E. Manucharyan[3], T. S. Jespersen[2], J. Nygård[2], and
C. M. Marcus[1,2]*

[1]*Department of Physics, Harvard University, Cambridge, Massachusetts 02138, USA*

[2]*Center for Quantum Devices, Niels Bohr Institute, University of Copenhagen,
Universitetsparken 5, 2100 Copenhagen Ø, Denmark*

[3]*Society of Fellows, Harvard University, Cambridge, Massachusetts 02138, USA*

---

[*] This chapter is adapted with permission from Phys. Rev. Lett 110, 217005 (2013). ©(2013) by the American Physical Society

3.1 Introduction

In this experiment, tunneling spectroscopy was performed on a segment of InAs nanowire confined between two superconducting leads. We demonstrate both phase and gate control of sub-gap states in a Kondo-correlated Josephson junction ($k_B T_K \sim \Delta$) [72]. We also report the first evidence of a singlet to doublet QPT induced by the superconducting phase difference. Our InAs nanowire Josephson junction has an additional normal metal tunnel probe which allows the measurement of the density of states via tunneling in the region between the superconducting contacts (Al).

By using normal metal, we avoid the complication of having to deconvolve the density of states of the probe from the tunneling conductance. At magnetic fields above the critical field of Al, tunneling into the InAs quantum dot with odd electron occupancy showed Kondo resonances [73] with associated Kondo temperatures, $T_K \sim$ 1 K. Near zero field, tunneling into the nanowire revealed the superconducting gap of the Al leads, $\Delta \simeq 150\,\mu$eV, and a pair of sub-gap resonances (SGR) symmetric about zero bias. For certain parameters in gate and phase, the SGRs intersect each other at zero bias, which we interpret as a level-crossing QPT. However, no such crossing occurred upon suppressing Δ to zero with an applied magnetic field. Instead, the SGRs evolve smoothly into Kondo resonances, and this transition is typically accompanied by the appearance of a separate zero-bias resonance of unknown origin.

3.1.1 Yu-Shiba-Rusinov states

Spin impurities in superconductors can drastically modify the state of its host, for instance, by suppressing the transition temperature and by inducing sub-gap states [74]. Using a hybrid superconductor-semiconductor device, one can investigate this process with precise experimental control at the level of a single impurity [72]. Exchange interaction between the single quantum spin impurity and quasiparticles modifies the order parameter locally, thereby creating Yu-Shiba-Rusinov sub-gap states [69–71, 75, 76]. For weak exchange interaction, a sub-gap state near the gap edge emerges from singlet correlations between the impurity and the quasiparticles. Increasing exchange interaction lowers the energy of the singlet state and increases a key physical parameter, the normal state Kondo temperature T_K. At $k_B T_K \sim \Delta$ (Kondo regime), where Δ is the superconducting gap, the energy gain from the singlet formation can exceed Δ, resulting in a level-crossing quantum phase transition (QPT) [74, 77–79]. The QPT changes the spin and the fermion parity of the superconductor-impurity ground state, and is marked by a peak in tunneling conductance at zero bias [80].

A mesoscopic superconductor-quantum dot-superconductor Josephson junction [Figs. 3.1(a) and 3.1(b)] is an ideal device to study Yu-Shiba-Rusinov states because it provides a novel control knob that tunes the exchange interaction via the superconducting phase difference across the junction, ϕ. A physical picture of the phase tunability of exchange interaction is the following: A spin 1/2 impurity is created by trapping a single electron in the lowest available orbital of the dot (assuming large level spacing) with a Coulomb barrier [Fig. 3.1(c)] [73, 81]. At the electron-hole (e-h) symmetry point, the spinful state, $|1, 0\rangle$, costs less than both the empty, $|0, 0\rangle$, and the doubly occupied, $|2, 0\rangle$, states by the charging energy U ($U > \Delta$ suppresses charge fluctuations at energies below Δ). Here, $|n_{dot}, n_{lead}\rangle$ denotes the electron (quasiparti-

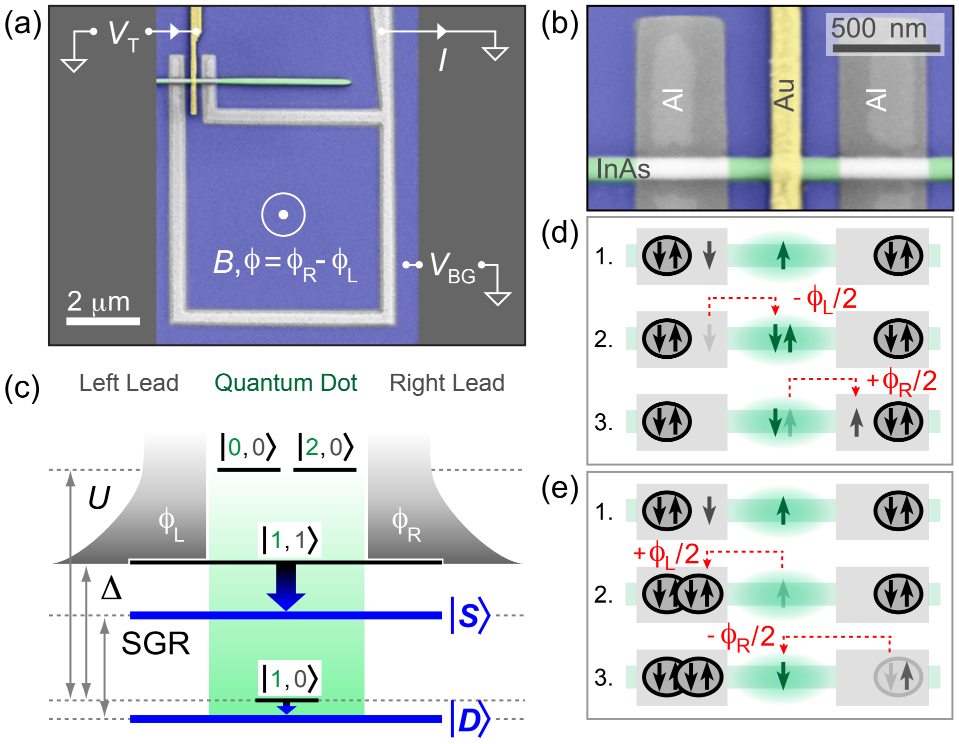

Figure 3.1: (a), (b) False colored scanning electron micrographs of a lithographically identical device. (c) Lowest energy states of a single orbital quantum dot at the electron-hole symmetry point for $k_B T_K \ll \Delta$. The states are labeled by their electron/quasiparticle occupation number in the format $|n_{dot}, n_{lead}\rangle$. Exchange interaction dresses the states $|1,0\rangle$ and $|1,1\rangle$ as the doublet, $|D\rangle$, and the singlet, $|S\rangle$, states respectively. Transition between $|D\rangle$ and $|S\rangle$ produces a sub-gap resonance (SGR). (d), (e) Phase sensitive spin-flip processes coupling the $|1,1\rangle$ states $|\uparrow,\downarrow\rangle$ and $|\downarrow,\uparrow\rangle$ via virtual occupation of (d) $|2,0\rangle$ and (e) $|0,0\rangle$.

cle) occupancies of the dot (leads), with arrows giving spin orientations when needed. Spin-flip scattering connects the degenerate states $|\uparrow,\downarrow\rangle$ and $|\downarrow,\uparrow\rangle$ via the virtual population of states $|2,0\rangle$ [Fig. 3.1(d)] or $|0,0\rangle$ [Fig. 3.1(e)]. These two scattering channels cause an effective (super-) exchange interaction between quasiparticles and the spinful dot. Compared to scattering via $|2,0\rangle$, scattering via $|0,0\rangle$ differs by a phase factor $\exp(-i\phi)$ because it is accompanied by a Cooper pair transfer [Fig. 3.1(e)]. At $\phi = \pi$ these two scattering channels interfere destructively, making the exchange coupling minimal at $\phi = \pi$ and maximal at $\phi = 0$. Consequently, both the singlet excited state, $|S\rangle$, and the doublet ground state, $|D\rangle$, acquire a phase modulation, albeit only in higher order processes for the latter [64, 66, 67, 82–86].

3.1.2 Previous works

The ground state of spinful Josephson junctions have been investigated by previous experiments [87–92]. Phase-biased junctions with weak coupling showed negative supercurrent [87, 88], consistent with theoretical predictions of the weak phase-modulation of $|D\rangle$ [82–84], while for strong coupling, positive supercurrent was observed [89, 90]. The latter was interpreted in terms of a QPT associated with the interchange of states $|S\rangle$ and $|D\rangle$ at $k_B T_K \sim \Delta$ [90–92]. Meanwhile, other experiments have performed tunneling spectroscopy on spinful Josephson junctions without phase control [93–96], or with phase control but away from the Kondo regime [97]. This leaves the effect of phase on sub-gap states in the Kondo regime unaddressed. Tunneling spectroscopy in similar devices has also been used recently to examine signatures of Majorana end states [18–20].

3.2 The device

Epitaxially grown InAs nanowires approximately 100 nm in diameter were deposited on a degenerately doped Si substrate with a 100 nm thermal oxide. They were then contacted by two ends of a superconducting loop (5/100 nm Ti/Al) with area $\sim 25\,\mu\text{m}^2$ [Figs. 3.1(a) and 3.1(b)]. For this loop area, the flux period, $h/2e$, corresponds to a perpendicular magnetic field period of $72\,\mu$T. A third normal metal tunnel probe (5/100 nm Ti/Au) contacted the nanowire at the center of the 0.5 μm long junction. By adjusting ammonium polysulfide etch times, high (low) transparency was achieved for the barrier between Al (tunnel probe) and InAs [33]. The device was measured in a dilution refrigerator with a base temperature of 20 mK, through several stages of low-pass filtering and thermalization.

3.3 Measurements

When superconductivity in the entire device was suppressed by an applied magnetic field, B, diamond patterns characteristic of weak Coulomb blockade (CB) were observed in transport between the loop and the normal lead [Fig. 3.2(a)]. Consecutive diamonds alternate in size, indicating that the orbital level spacing, ξ, is comparable to the charging energy, $U \simeq 200\,\mu\text{eV}$. The smaller (odd occupancy) diamonds contain backgate-independent (V_{BG}) zero-bias ridges that split at higher magnetic fields (refer to Fig. 3.5) typical of the Kondo effect [73, 98]. From the temperature dependence of the zero-bias ridges, we estimate T_K to be in the range of 0.5-1 K (refer to Fig. 3.7). Poor visibility of the odd diamonds suggests strong coupling to the superconducting leads ($\Gamma_S \geq U$), and the amplitudes of the Kondo ridges indicate an asymmetry between superconducting and normal contacts [99]. While the estimated asymmetry, $\Gamma_N \sim \Gamma_S/10$, will likely broaden the tunneling resonances, it is sufficient to qualitatively treat the Au lead as a weak tunneling probe.

In the superconducting state ($B \sim 0$), gap-related features were observed at tunnel-probe voltages, $V_{\text{T}} \simeq \pm 150\,\mu V \simeq \pm\Delta/e$, consistent with the gap of Al. SGRs symmetric about zero bias were also observed [Fig. 3.2(b)]. Comparison of Figs. 3.2(a) and 3.2(b) shows that the positioning (in V_{BG}) of SGRs in the superconducting state

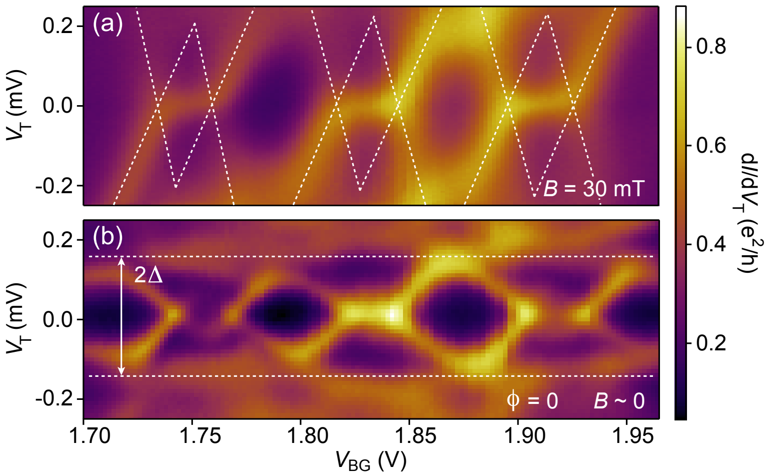

Figure 3.2: Differential conductance as a function of tunnel-probe voltage, V_{T}, and backgate voltage, V_{BG}. (a) Normal state data, $B = 30$ mT. (b) Superconducting state data, $B \sim 0$ and $\phi = 0$. Coulomb diamonds in (a) and superconducting gap in (b) are highlighted with dotted lines.

coincides with CB and Kondo features in the normal state. The SGRs and their symmetric partners converge towards each other and sometimes overlap in an odd CB valley. In contrast, they are pushed towards the gap edge in the even CB valleys. Cuts of the data in Fig. 3.2 are shown Fig. 3.5.

Based on their qualitative dependence on V_{BG} and ϕ, three categories of SGRs in the case of a spinful dot were identified. (i) For small charging energy, $U < (\Delta, \Gamma_S)$, SGRs do not cross the zero-bias axis for any V_{BG} or ϕ [Figs. 3.3(a), 3.3(d), and 3.3(g)]. The SGR energy is maximal at $\phi = 0$ and minimal at $\phi = \pi$ [Fig. 3.3(d) and 3.3(g)]—this is the conventional phase dependence of non-interacting Josephson junctions (see section 2.6.1). (ii) For large charging energy, $U > \Delta$ (for estimation methods, refer to Fig. 3.6), the SGRs overlap, crossing zero bias twice as a function of V_{BG} [Fig. 3.3(c)]. Between zero-bias crossings, the phase dependence of SGR energies is the opposite of the conventional behavior, that is, minimal at $\phi = 0$ and maximal at $\phi = \pi$ [Fig. 3.3(i)]. We call this a π-shifted phase dependence. Outside the intersections

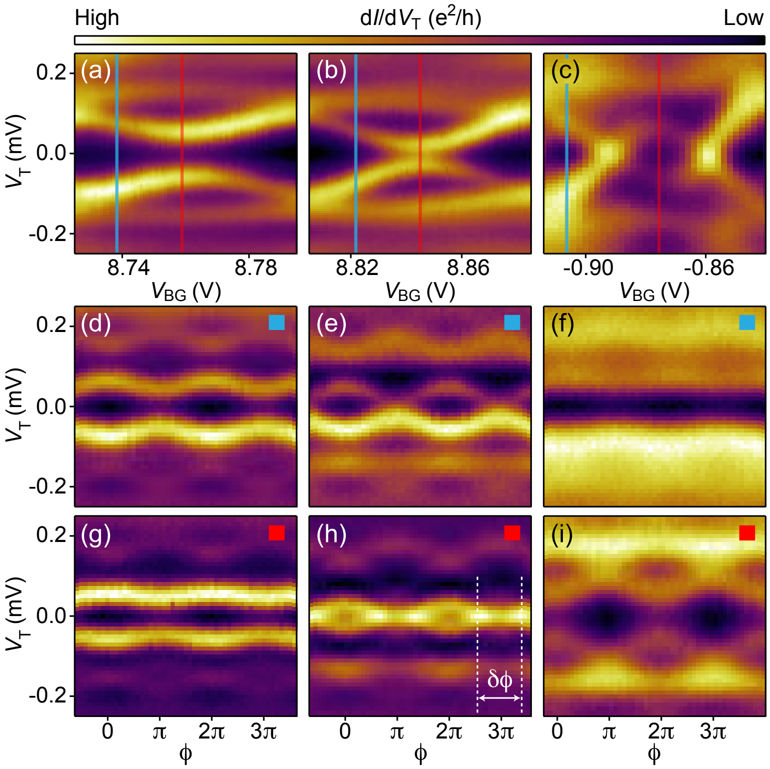

Figure 3.3: Three sub-gap resonances (SGRs) arranged in columns of increasing U. (a)–(c) $V_{\rm BG}$ dependence of the SGRs at $\phi = 0$. The lower rows show the corresponding phase dependence off (d)–(f) and on (g)–(i) the electron-hole symmetry point. (d)–(g) Conventional phase dependence, (h) hybrid phase dependence, (i) π-shifted phase dependence.

in $V_{\rm BG}$, the phase dependence of SGR energy is conventional [Fig. 3.3(f)]. (iii) For moderate charging energy $U \sim \Delta$ [Figs. 3.3(b), 3.3(e), and 3.3(h)], SGRs do not intersect for any $V_{\rm BG}$ at $\phi = 0$ [Fig. 3.3(b)]. Phase dependence away from the e-h symmetry point is conventional [Fig. 3.3(e)], but close to the symmetry point, the pair of SGRs intersects twice per phase period of 2π [Fig. 3.3(h)]. Crossings occur at $\phi = \pi \pm \delta\phi/2$, where $\delta\phi < \pi$ is the phase difference between the two closest crossings [Fig. 3.3(h)]. With this type of SGR, the phase dependence depends on the phase value itself: it is conventional for $\phi \sim 0$, and π-shifted for $\phi \sim \pi$.

In Fig. 3.4 we examine the magnetic field evolution of three π-shifted SGRs at

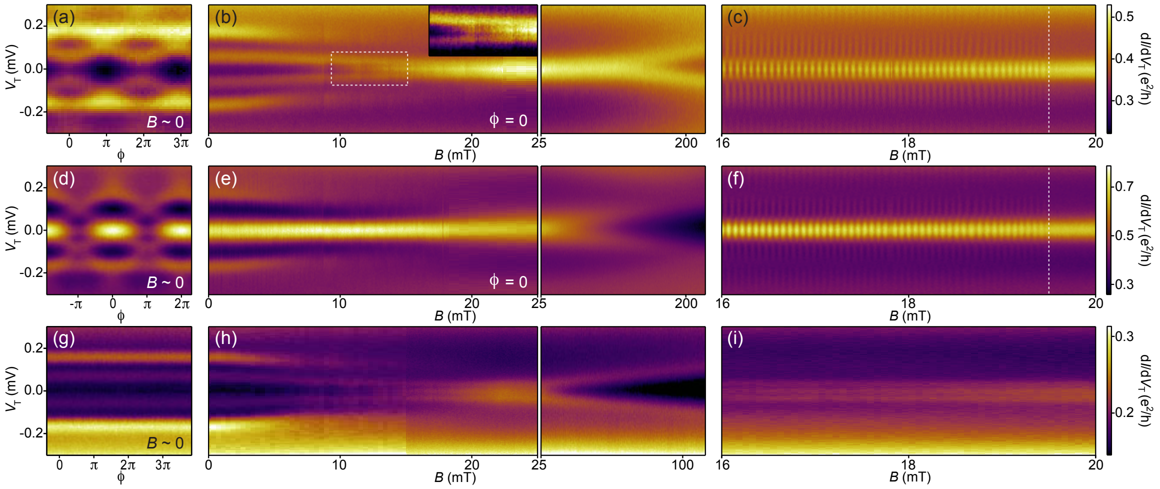

Figure 3.4: Arranged in the order of decreasing T_K, each row shows the evolution of a SGR at the electron-hole symmetry point as a function of phase and magnetic field. The left column shows phase dependence at $B \sim 0$, the center column shows magnetic field dependence at $\phi = 0$, and the right column shows the magnetic field and phase dependence around $B = 18$ mT. To obtain the phase constant panels (b) and (e), we select $\phi = 0$ data points from the full data set. The oscillations of the SGRs disappear abruptly at $B = 19.5$ mT (dotted lines) in both (c) and (f). Inset in (b) is a closeup of the region outlined with dotted lines. A third resonance, pinned at zero bias, is clearly visible in the high contrast color scale.

their e-h symmetry points. The first SGR [Figs. 3.4(a)–3.4(c)] is identical to the one shown in Fig. 3.3(c). Selecting $\phi = 0$ from the full data set shown in Fig. 3.12, the well separated SGRs gradually approach zero-bias and merge into a Kondo resonance in the normal state [Fig. 3.4(b)]. Temperature dependence of the normal-state Kondo peak gives $T_K \simeq 1\,\mathrm{K}$ [73] (refer to Fig. 3.7). Taking $g \sim 13$ from normal-state CB data (refer to Fig. 3.8), the splitting of the Kondo peak at ~ 140 mT is consistent with this value of T_K [100] [Fig. 3.4(b)]. In the other two cases (bottom two rows of Fig. 3.4), Kondo peaks split at lower fields of $B \sim 50$ mT [Fig. 3.4(e)] and $B < 20$ mT [Fig. 3.4(h)], suggesting lower Kondo temperatures.

In the second case [Figs. 3.4(d)–3.4(f)], SGRs overlap at zero-bias for $\phi = 0$, but are separated for $\phi = \pi$ [Fig. 3.4(d)]. The overlapping SGRs at zero field evolve continuously into a Kondo resonance as the field is increased into the normal state regime [Fig. 3.4(e)]. Phase dependent oscillations of the SGR vanish abruptly at a critical value of field, $B_c = 19.5\,\mathrm{mT}$ [Fig. 3.4(f)]. The same critical field is observed in Fig. 3.4(c), and also in higher density regimes of the device (refer to Fig. 3.9).

The last case has no phase-dependence [Fig. 3.4(g)], presumably because of poor coupling to one of the superconducting contacts. However, its V_{BG} dependence allows us to establish that this SGR is indeed a π-shifted type (see Fig. 3.11). Here, in contrast to the first two cases, the pair of SGRs evolve continuously and directly into split Kondo peaks without ever merging or crossing at zero bias [Figs. 3.4(h) and 3.4(i)].

Close inspection of Fig. 3.4 reveals an unexpected and intriguing feature: a narrow needle-like resonance pinned at zero bias. In Fig. 3.4(b), this “needle” is absent at $B = 0$ but appears for $B > 10$ mT while the leads are still superconducting. In Fig. 3.4(d) the needle is hidden by the SGRs at $\phi = 0$, yet it is clearly visible at $\phi = \pi$. In this case, the needle exists at $B = 0$, and merges into the normal-state Kondo resonance at higher field (most easily seen in Fig. 3.12(f) where $\phi = \pi$). In Fig. 3.4(h), the needle appears at $B > 10$ mT, similar to the case in Fig. 3.4(b), despite a large difference in Kondo temperatures. In fact, the strength of the needle appears uncorrelated with T_K of the normal-state Kondo peak (see Fig. 3.13). The needle is also distinct from the normal state Kondo resonance as seen in Figs. 3.4(h) and 3.4(i), where three separate peaks can be identified: The two peaks flanking the central needle appear to emerge from the SGR at the low-field end and evolve continuously into the split Kondo peaks at the the high-field end. We find that the needle only appears between the two V_{BG} intersection points of π-shifted SGRs, which in turn corresponds to an odd Coulomb diamond (refer to Fig. 3.14). Finally, the needle appears brighter at $\phi = 0$, when the separation between the two SGR is the smallest [Figs. 3.4(c) and 3.4(d)].

3.4 Discussion

We now compare theoretical expectations for SGRs [67] to experimental observations. At the e-h symmetry point of a spinful quantum dot with suppressed charge fluctuations, the phase-tunable exchange interaction detaches a singlet state $|S\rangle$ down from the gap edge [Fig. 3.1(c)]. Since quantum interference weakens the exchange interaction at $\phi = \pi$ [Figs. 3.1(d) and 3.1(e)], a π-shifted SGR is indeed expected (phase modulation of the energy of $|D\rangle$, being a higher-order effect, is much weaker than that of $|S\rangle$) [64, 66, 85, 86]. This is consistent with our experiment, as seen, for example, in Fig. 3.3(i). Strong coupling to the leads, reflected in the large T_K, should further result in a SGR that is well separated from the gap edge at $\phi = 0$ [78, 79]. Detuning V_{BG} towards a neighboring even diamond increases charge fluctuations and mixes either $|0, 0\rangle$ or $|2, 0\rangle$ into $|S\rangle$, thereby lowering its energy. Consequently, one expects a level-crossing QPT to a singlet ground state as V_{BG} approaches an even diamond, in agreement with the zero-bias crossings in Fig. 3.2(b) and Fig. 3.3(c). This QPT is predominantly governed by the enhanced charge fluctuations away from the e-h symmetry point. Finally, the observed conventional phase dependence in the even state of the dot [Fig. 3.3(f)] is also expected, because a spinless dot effectively acts as a potential scatterer in a non-interacting junction [101].

A more interesting QPT occurs in Fig. 3(h) as a function of phase-bias. It corresponds to a situation where the energy gain from the quasiparticle-dot singlet formation makes this state the ground state at $\phi = 0$ but not at $\phi = \pi$. This behavior is known in theory literature as $0'$-junction or π'-junction [67, 102], and, to our knowledge, has not been reported in previous experiments.

Reducing Δ sufficiently below $k_B T_K$ should result in a level-crossing QPT that is driven entirely by spin fluctuations [74]. Experimentally, we would see a zero-bias crossing of the SGRs at $B < B_c$ as B is increased to suppress Δ. However, this theoretical expectation is not seen in our device as exemplified in Figs. 3.4(b) and 3.4(h), perhaps obscured by our current experimental resolution or by the needle feature. The needle may be related to similar features observed in recent experiments [95, 96]. An unlikely soft gap in Al may explain such a resonance in terms of conventional Kondo screening. We note, however, that the needle itself does not split with increasing B, as one might expect from a conventional Kondo effect. More intriguingly, the needle appears much stronger at $\phi = 0$ than at $\phi = \pi$, suggesting possible phase dependence and a link to the sub-gap states (refer to Fig. 3.15). While the observed behaviors of sub-gap states agree at $B \sim 0$ with existing theory on Yu-Shiba-Rusinov states, further theory and experiment are needed to understand the origin of the needle and the magnetic field dependence of the sub-gap states [65, 103].

3.5 Conclusion

In summary, tunnel-probe spectroscopy of the density of states of an InAs quantum wire with controlled phase between two superconducting contacts is realized experimentally and investigated in detail. This novel system allows a quantum phase transition between states of different spin and parity to be studied. Crossover between a spinful π-junction at low magnetic field and the corresponding Kondo system at higher field shows how these two states connect. An unexplained narrow zero-bias feature at intermediate field with phase dependence is found.

3.6 Acknowledgments

We thank P. Krogstrup, M. Madsen, and C. Sørensen for MBE growth. We also thank D. Abanin, J. Bauer, H. Churchill, E. Demler, K. Flensberg, L. Glazman, K. Grove-Rasmussen, F. Kuemmeth, J. Paaske, D. Pekker, and J. Sau for fruitful conversations. Support from the Carlsberg Foundation, the Danish National Research Foundation, the Lundbeck Foundation, the EU-FP7 project SE2ND (271554), and Microsoft Project Q is gratefully acknowledged.

3.7 Additional information

3.7.1 Zeeman splitting of Kondo resonances

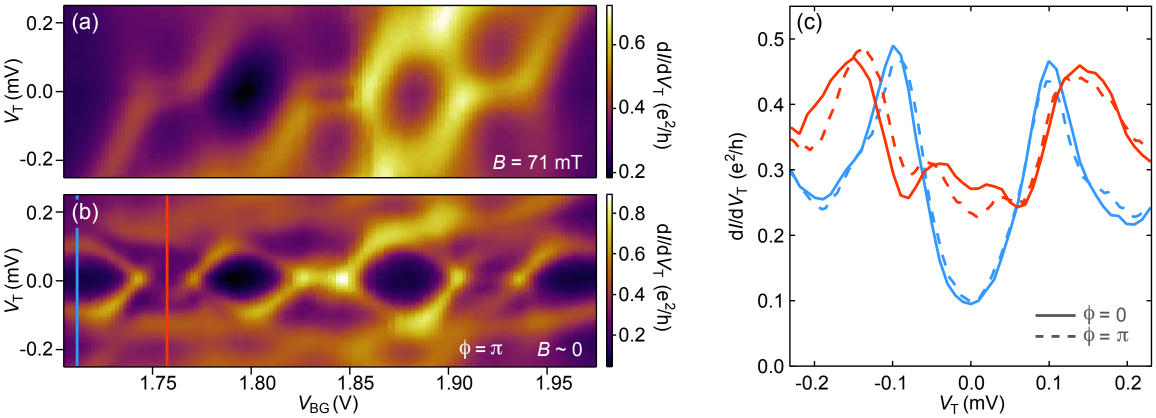

Figure 3.5: (a) Differential conductance of the device as a function of V_{T} and V_{BG} at $B = 71$ mT. Two odd electron occupancy Coulomb diamonds on the left show a pair of Zeeman split co-tunneling peaks. (b) Superconducting state of the device, at $B \sim 0$ and $\phi = \pi$. (c) Vertical line cuts of Fig. 3.2(b) and Fig. 3.5(b) at backgate voltages indicated by blue (even Coulomb diamond) and red (odd Coulomb diamond) lines in Fig. 3.5(b). Dotted and solid lines indicate $\phi = \pi$ and $\phi = 0$ respectively.

In this section we show the same normal/superconducting states illustrated in Fig. 3.2, with the exception that in Fig. 3.5(a), the magnetic field is at a higher value of 71 mT and in Fig. 3.5(b), $\phi = \pi$ and $B \sim 0$. In Fig. 3.5(a), the two left-most Kondo ridges shown in Fig. 3.2(a) have split into co-tunneling peaks at higher magnetic fields. The right-most Kondo ridge remains intact, indicative of varying T_K for different dot orbitals. When the device is in the superconducting state, applying a finite phase pushes the symmetric pairs of SGRs apart such that they overlap each other more, making them more resolvable. Fig. 3.5(c) shows differential conductance as a function of V_{T}, taken at V_{BG} values indicated in Fig. 3.5(b) (blue and red lines).

3.7.2 Estimating U, Γ, and T_K

Fig. 3.6 shows Coulomb diamonds of various sizes. The height of the even diamonds give us the sum of the dot orbital spacing, ξ, and the charging energy, U. The height of the odd diamonds gives just the charging energy U. Looking at the diamonds in Fig. 3.6, these quantities fluctuate with V_{BG}. Coupling to the superconducting leads Γ_S also varies with V_{BG}, evident in the varying sharpness of the diamond edges.

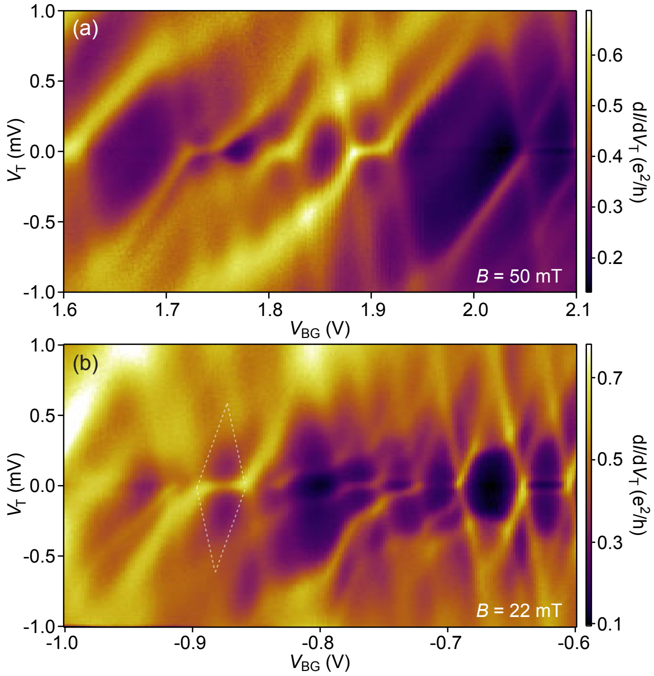

Figure 3.6: Differential conductance as a function of V_{T} and V_{BG} in two backgate voltage ranges. (b) White dotted lines outline the extent of an odd Coulomb diamond.

Consequently, T_K should vary as well. In Figs. 3.6(a) and 3.6(b), the right-most Kondo ridge has already split into co-tunneling peaks, indicative of smaller T_K compared to the other Kondo ridges in the figures. In Fig. 3.6(b) we highlight with white dotted lines the extent of an odd diamond. This diamond corresponds to the state shown in Fig. 3.3(c) and 3.4(a). From the size of the diamond we estimate U to be approximately 500 μeV.

3.7.3 Temperature dependence of the Kondo resonance

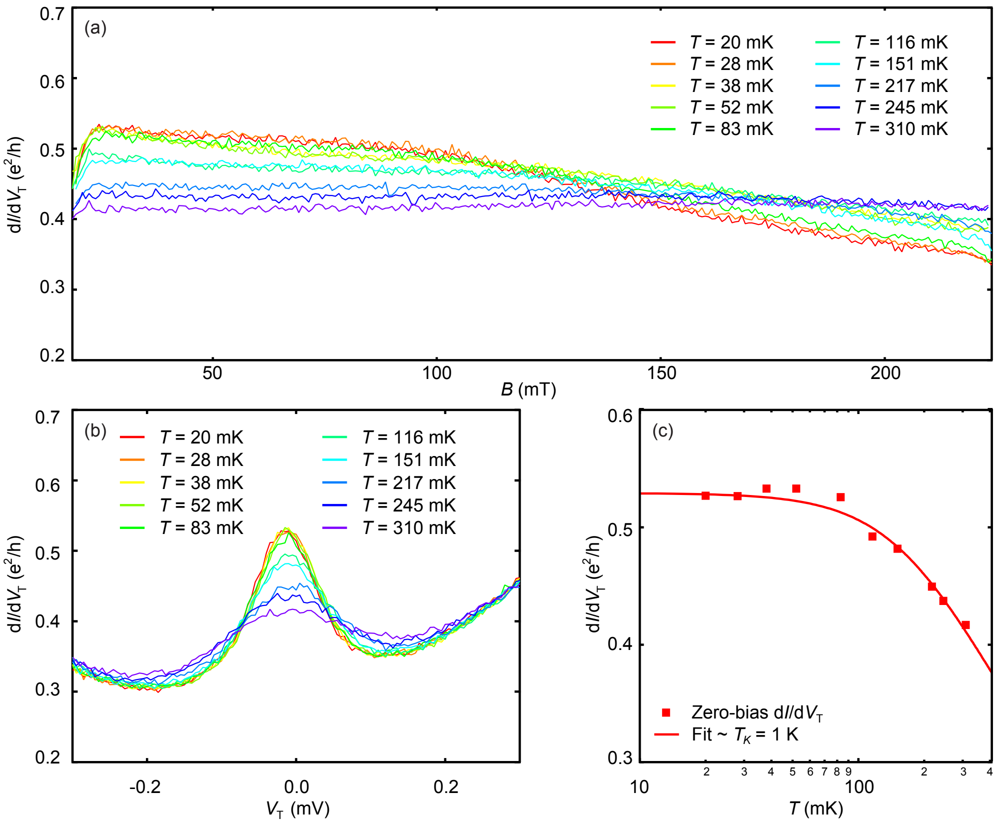

Figure 3.7: (a) Zero-bias conductance at the electron-hole symmetry point of an odd diamond as a function of magnetic field, and at various temperatures. (b) Differential conductance as a function of bias voltage, V_T, at $B = 24$ mT and at various temperatures. (c) Conductance of the Kondo peaks as a function of temperature. The solid line is a fit for $T_K = 1$ K.

In this section, we examine the temperature dependence of the Kondo resonance shown in Fig. 3.4(b). Fig. 3.7(a) shows the zero-bias differential conductance as a function of B. Below $B = 24$ mT, the superconducting gap of the leads suppresses the differential conductance. At $B = 24$ mT, superconductivity in the entire device is fully removed, and the differential conductance reaches its maximum value. As B is increased, the Kondo resonance diminishes in amplitude and eventually splits, resulting in the decrease of the differential conductance. Taking the differential conductance at its maximal value when $B = 24$ mT, we plot it as a function of V_{T} at various temperatures in Fig. 3.7(b). We then fit the zero-bias differential conductance with the following expression from Ref. [104]:

$$G(T) = G_0\{1 + (2^{1/s} - 1)(T/T_K)^2\}^{-s} \tag{3.1}$$

, where $s = 0.22$ for spin 1/2 electrons and G_0 and T_K are fit parameters. The result is an estimated Kondo temperature of $T_K = 1$ K.

3.7.4 Extracting the g-factor

To extract the g-factor of our InAs nanowire device, we reduce V_{BG} until the device is almost pinched off. Sharply defined Coulomb diamonds and their excited states indicate that the device is in the deep Coulomb blockade regime [Fig. 3.8(a)]. Fixing the backgate voltage at the value indicated by the green line in Fig. 3.8(a), we examine the voltage bias and magnetic field dependence of these tunneling resonances in Fig. 3.8(b). The ground state of the dot splits linearly in magnetic field [dotted lines in Fig. 3.8(c)]. Taking the value of the splitting and correcting for the capacitance of the leads, we extract a g-factor of 13.

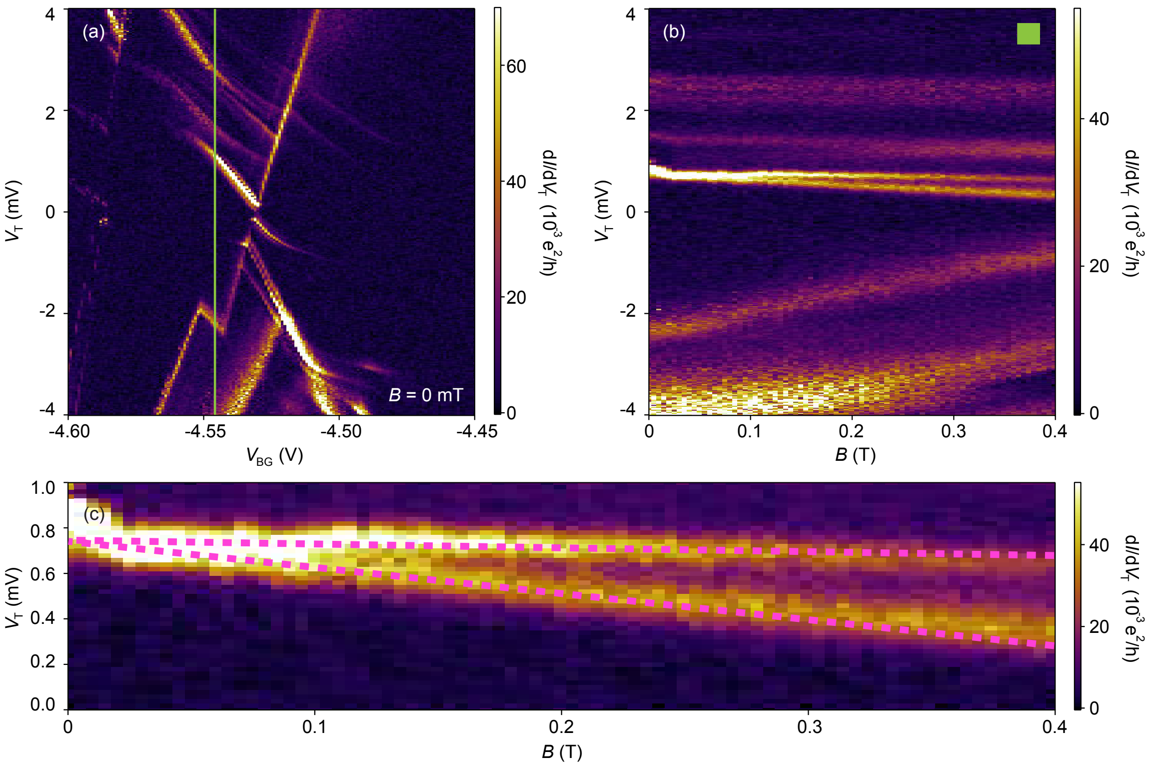

Figure 3.8: (a) Differential conductance as a function of V_T and V_BG in the deep Coulomb blockade regime. (b) Taking a cut of (a) at a fixed V_BG (green line) and examining the magnetic field dependence. (c) A closeup of the Zeeman split resonance in (b).

3.7.5 Critical field of the device in both strongly and weakly interacting regimes

We compare the magnetic field dependence of the device in two different regimes - strongly interacting and weakly interacting. In the strongly interacting case [Fig. 3.9(a)], we show the full magnetic and flux dependence of a SGR with a π-shifted phase dependence [same SGR shown in Fig. 3.4(d)–(f)]. Similar data is shown in Fig. 3.9(b) for a SGR in the weakly interacting regime. Unlike the SGR in Fig. 3.9(a), no Kondo resonance in the normal state is observed. Comparing their zero-bias conductance in Fig. 3.9(c), oscillations due to the phase dependent SGRs vanish abruptly at a

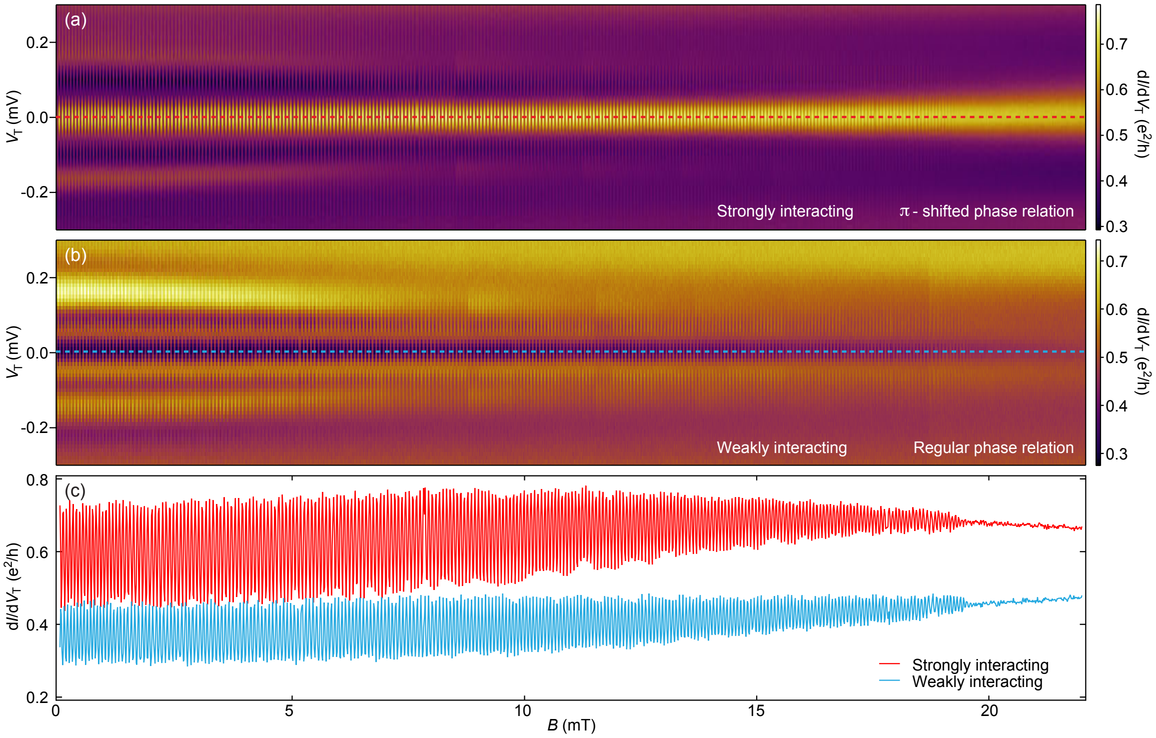

Figure 3.9: (a) Magnetic field dependence of a SGR in the strongly interacting regime. A Kondo zpeak appears above the critical magnetic field. (b) Magnetic field dependence of an SGR in the weakly interacting regime. (c) Zero-bias conductance cuts as a function of B. Oscillations stop abruptly at $B = 19.5$ mT.

common magnetic field $B = 19.5$ mT. This magnetic field value is also common for all charge configurations, and it is treated as the critical field, B_c of the device.

3.7.6 Singlet ground state SGR in the interacting regime

Fig. 3.10 illustrates an example where exchange interaction is large enough such that the ground state is a YSR-like singlet. The SGRs do not intersect at $\phi = 0$ for any value of V_{BG} [Fig. 3.10(a) and 3.10(d)], and their phase dependence at the e-h symmetry point is regular [Fig. 3.10(b)]. At higher fields, the SGRs merge into a Kondo resonance that subsequently splits [Fig. 3.10(c)]. Away from the e-h symmetry

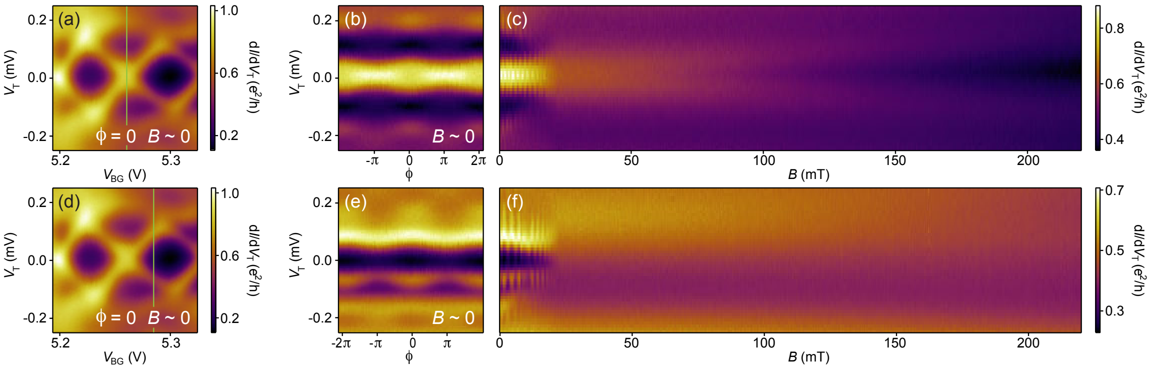

Figure 3.10: (a) and (d) SGR with a singlet ground state at $\phi = 0$. (b) and (c) Phase dependence and magnetic field dependence of the SGR at the electron-hole symmetric point. (e) and (f) Phase and magnetic field dependence of the SGR away from the odd diamond.

point [green line in Fig. 3.10(d)], the phase dependence of the SGR is still regular, but at higher fields the Kondo resonance is absent.

3.7.7 V_{BG} dependence of π-junctions

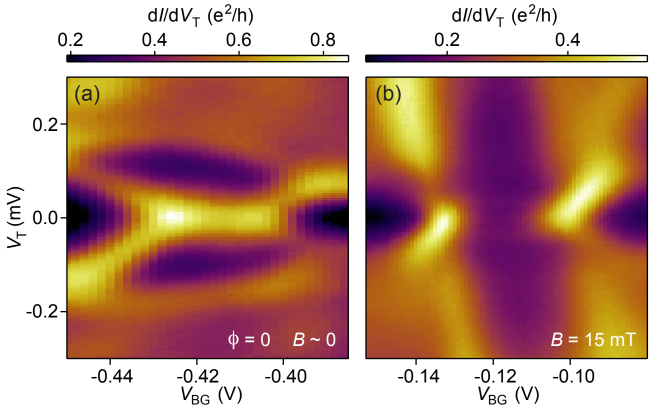

Figure 3.11: (a) and (b) V_{BG} dependence of the SGR shown in Fig. 3.4(d) and Fig. 3.4(g) respectively.

V_{BG} dependence of the SGR in Fig. 3.4(a) is shown in Fig. 3.3(c). Fig. 3.11(a) shows V_{BG} dependence of the SGR in Fig. 3.4(d). At $\phi = 0$, the SGRs are just touching at zero-bias. When ϕ is shifted away from 0, the overlap between the two

SGRs increases. The same is shown in Fig. 3.11(b) for the SGR in Fig. 3.4(g). Even though this SGR lacks a phase dependence (likely due to the poor coupling to one of the superconducting leads), the overlapping SGRs indicate that the SGR has a doublet ground state and is of the π-shifted type. At $B = 15$ mT, the needle is evident.

3.7.8 Full magnetic field dependence with phase information intact

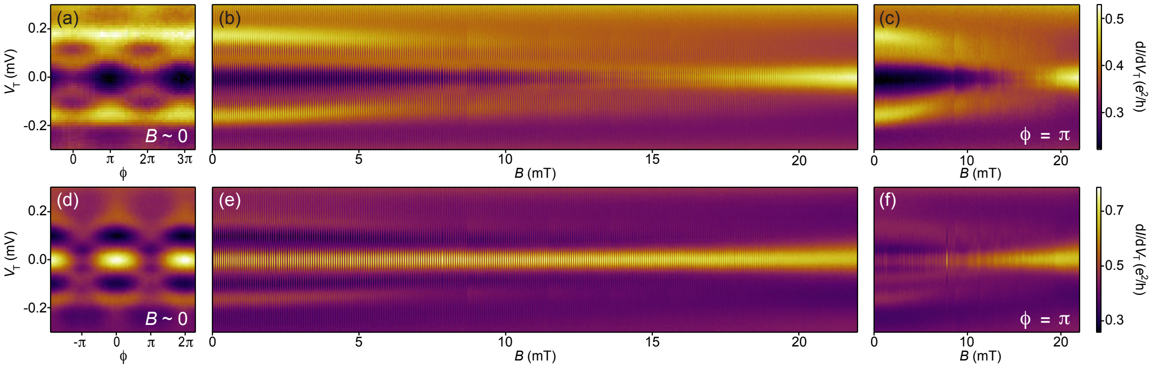

Figure 3.12: (a) and (d) Phase dependence of the SGRs shown in Figs. 3.4(a) and 3.4(d). (b) and (e) Phase and magnetic field dependence of these SGRs. (c) and (f) Phase information is extracted and fixed at $\phi = \pi$.

Fig. 3.12 shows the full phase and magnetic field dependence of the SGRs shown in Fig. 3.4. The ABS shown in the last row of Fig. 3.4 has no phase dependence. We can also choose to fix the superconducting phase difference at $\phi = \pi$. This is shown in Fig. 3.12(c) and 3.12(f).

3.7.9 Temperature dependence of the needle

We examine the temperature dependence of the needle shown in Fig. 3.4(a)–(c). Fig. 3.13(a)–(f) shows the magnetic field dependence of the SGR at six different temperatures. Phase information is removed and fixed at $\phi = 0$ so that the needle is clearly visible. We notice in Fig. 3.13(d) that when $T = 52$ mK, the needle becomes indiscernible from the surrounding SGRs. Taking cuts in V_T at $B = 13\,\mathrm{mT}$, we see that a small zero-bias peak is visible for temperatures up to 52 mK. This is plotted in Fig. 3.13(g) and then offset vertically in Fig. 3.13(h) for better clarity. Keeping in mind that the Kondo temperature for this feature is about 1 K, we note here the difference in energy scales of the needle when compared to the normal state Kondo

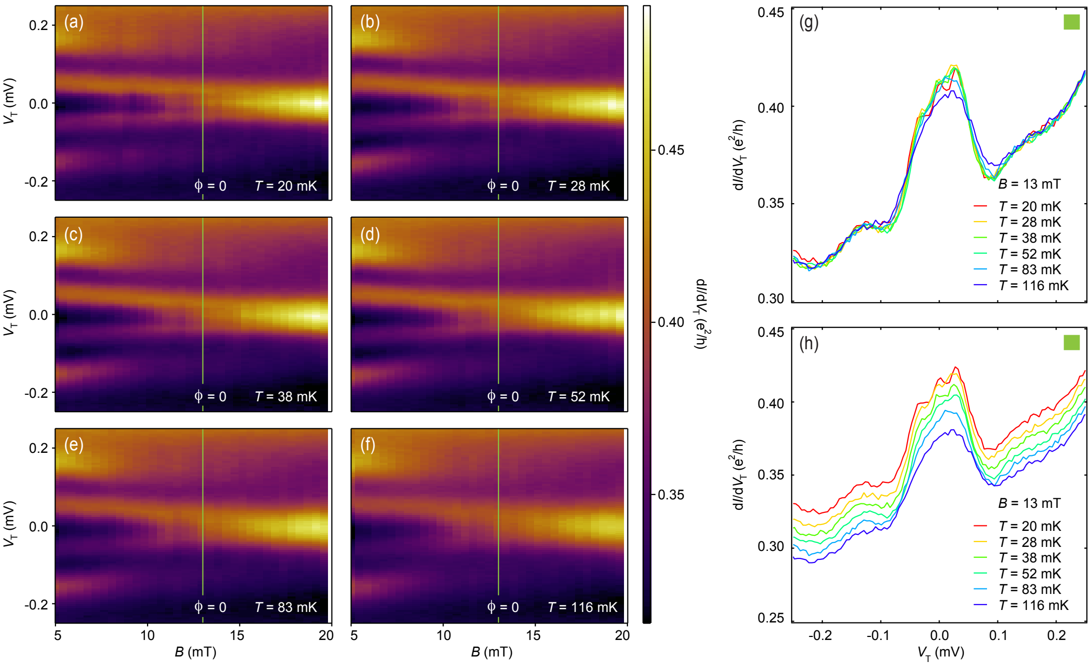

Figure 3.13: (a) - (f) V_T and B dependence of the SGR and needle at six temperatures. (g) Vertical cuts [green lines in (a) - (f)] at $B = 13$ mT. (h) The same data that is shown in (g), except that they are offset vertically for better clarity.

resonance.

3.7.10 Common occurrence of the needle in odd Coulomb valleys

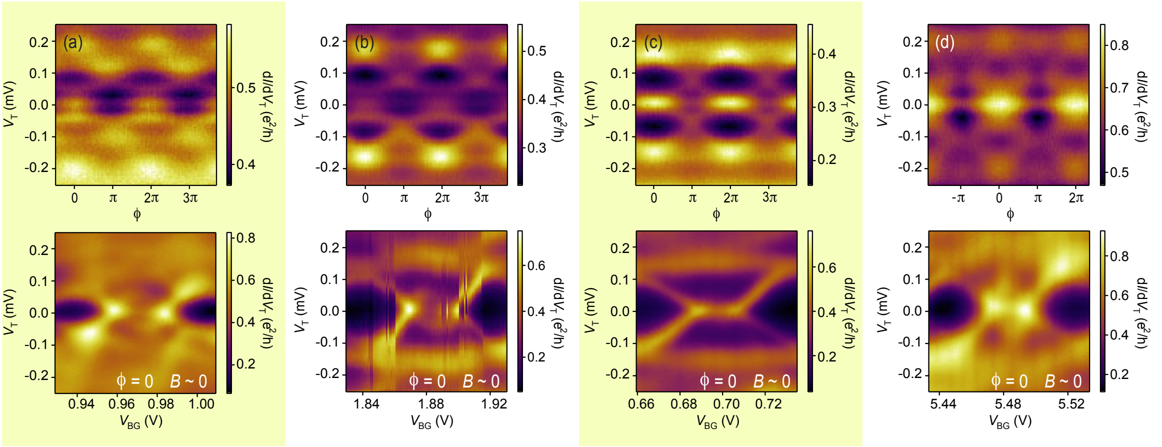

Figure 3.14: (a)–(d) Four π-shifted SGRs with an additional needle structure already present at $B \sim 0$ mT. The top row shows their phase dependence, and the bottom row shows their evolution with V_{BG}.

Four SGRs with a doublet ground state are shown in Fig. 3.14. On the top row, all of the SGRs have maximal energy at $\phi = \pi$ and minimal energy at $\phi = 0$, indicating a π-shifted phase dependence. In addition to the SGRs, the needle is also present as a faint resonance pinned at zero energy. In these examples, the needle is present at $B \sim 0$ mT. On the bottom row, the V_{BG} dependence of these SGRs at $\phi = 0$ are shown. In Figs. 3.14(a), 3.14(b), and 3.14(d), the needle can be seen between the two arching SGRs. It only exists between the two intersection points of the SGRs, which in turn is approximately the extent of the odd diamond in the normal state of the device.

3.7.11 Phase dependence of the needle

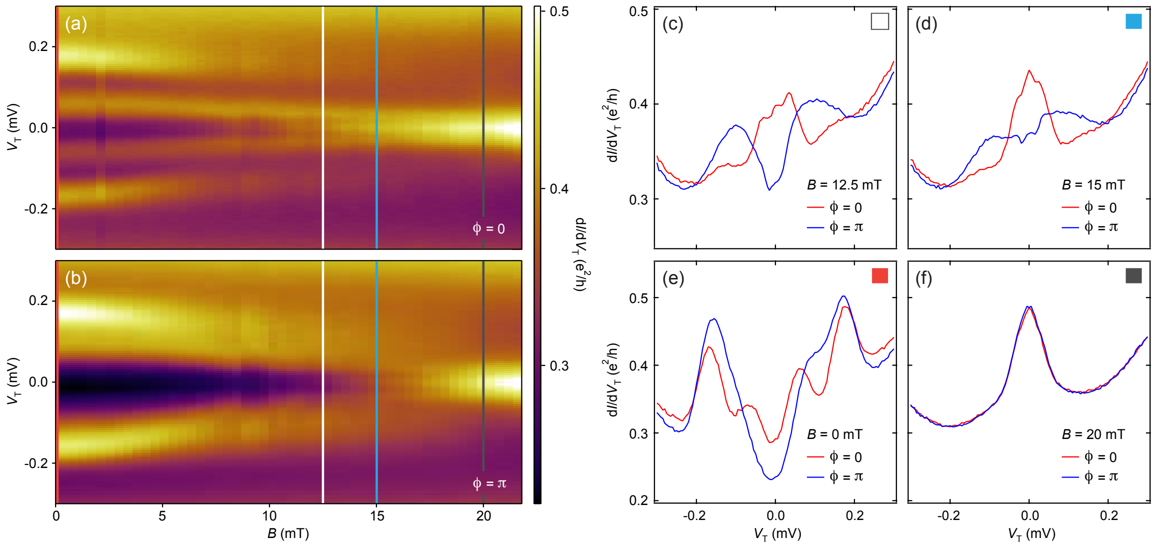

Figure 3.15: (a) and (b) Phase extracted magnetic field dependence of the needle at phases 0 and π respectively. (c)–(f) Cuts in bias voltage for each phase at four different magnetic fields.

In this section we look into the possible phase dependence of the needle. In Fig. 3.15(a) and 3.15(b) we compare the magnetic field dependence of the needle at phases 0 and π. Compared on the same vertical color scale, we see that the needle is more visible at a lower magnetic field when $\phi = 0$. Taking cuts in V_{T} at four different values of B, we compare the effects of ϕ on the needle. At $B = 12.5$ mT [Fig. 3.15(c)], the zero-bias peak is visible at $\phi = 0$ but absent at $\phi = \pi$. At $B = 15$ mT [Fig. 3.15(d)], a strong zero-bias peak can be seen at $\phi = 0$, and a fainter one at $\phi = \pi$. The feature is missing at $B = 0$ mT [Fig. 3.15(e)] for both phases, and at $B = 20$ mT the traces are identical [Fig. 3.15(f)].

Chapter 4

Spin-Resolved ABS in S-QD-N Devices

4.1 Introduction

In the previous experiments, the critical field of the devices were limited to about 20 mT. Assuming a g-factor of 10 for InAs, any Zeeman splitting of the sub-gap resonances (SGRs) would be smaller than 10 μeV. Compounded with broadened tunneling resonances, it becomes obvious that these devices are ill-suited for direct measurements of the spin and magnetic properties of QD-S systems.

In this chapter, I turn to a different set of devices fabricated on InAs-Al core-shell nanowires. While the critical field of these devices are only slightly improved (B_c ranges from 80 mT to 250 mT), the vastly sharpened tunneling resonances allows us to distinguish Zeeman split SGRs.

We observe the Zeeman splitting of the magnetic doublet Andreev bound state (ABS) and extract g-factors ranging from 5 to 10. The experimental observations are largely consistent with theoretical expectations, with the exception that we occasionally observe an extra pair of spin-split SGRs when the ground state of the QD is a magnetic doublet. To the best of our knowledge, this is the second tunneling spectroscopy observation of spin-split ABS in InAs nanowires after prior experimental work in Ref. [36].

4.2 The Device

The InAs-Al core-shell nanowires used in these devices are grown epitaxially in a molecular beam epitaxy chamber. After growing the InAs core axially, Al is then grown radially around the core *in situ*. This results in a pristine and impurity free

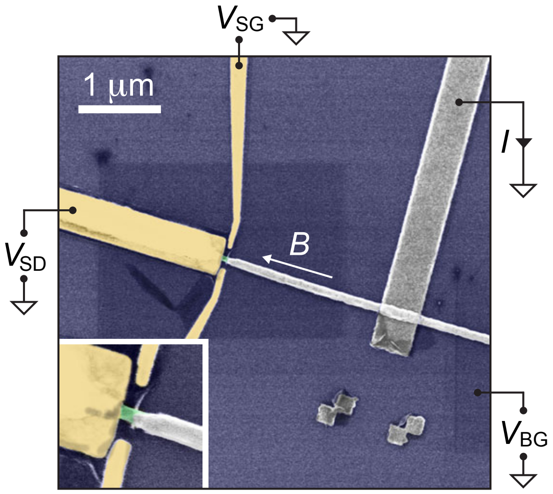

Figure 4.1: False color SEM micrograph of a lithographically similar device. Yellow represents the normal metal leads (Au), green the InAs core, and gray the superconducting shell and leads (Al). A source drain bias voltage, V_{SD}, is applied to the normal metal lead and we measure the differential conductance across the device. Voltage applied to the backgate, V_{BG}, or sidegate, V_{SG}, tunes the density of states of the exposed InAs core.

S-N interface. Further details on these core-shell nanowires can be found in Ref. [35] and also in Chapter 5. We deposit these nanowires on a degenerately doped Si substrate with a 100 nm thermal oxide. To expose the InAs core, we used 'Aluminum etchant - Type D', manufactured by Transene Company Inc. (details can be found in Appendix A.10). The electrodes are defined with standard electron beam lithography techniques. To make ohmic contacts to the Al shell and InAs core, the native oxides on the nanowire are removed with Ar ion milling prior to metals deposition. The core is contacted with a normal metal lead (Ti/Au, 5/80 nm), and the shell is contacted with a superconducting lead (Ti/Al, 5/130 nm). A lithographically similar device is shown in Fig. 4.1. The chemical potential of the exposed core can be tuned via a sidegate, V_{SG}, or the backgate, V_{BG}. We find that a QD forms naturally in the region of the exposed InAs core – a common feature of nanowire devices. The device is measured in a dilution refrigerator with a base temperature of 20 mK. In order to maximize the magnitude of the critical magnetic field, we apply the external magnetic field along the length of the nanowire.

4.3 Measurements

Using a combination of V_{BG} and V_{SG}, we bring the device into the tunneling regime ($G \ll G_0 = 2e^2/h$). As illustrated in Figs. 4.2(a) and 4.2(c), SGRs can be seen in the middle of odd Coulomb valleys, and they can be readily identified as ABSs arising from discrete QD levels. In Fig. 4.2(a), the pair of SGRs at zero magnetic field splits into four distinct resonances at $B = 40$ mT. Tuning V_{SG} to the particle-hole symmetry point of the Coulomb diamond, we look at the magnetic field dependence of the resonances in Fig. 4.2(b). The SGRs split linearly in B, until the superconducting gap closes and the resonances wash out into the background ($B_c \sim 70$ mT).

Fig. 4.2(c) shows an ABS with a magnetic doublet ground state at the particle-hole symmetry point. The crossing of resonances at zero-bias indicates a QPT between singlet and doublet ground states. Like the ABS shown in Fig. 4.2(a), the pair of SGRs split into four distinct resonances at finite magnetic fields. However, the doubling of resonances does not occur everywhere along V_{SG}. In fact, there is only one pair of SGRs near the middle of the Coulomb valley. Tuning V_{SG} away from the particle-hole symmetry point and away from the QPTs, the resonances once again split linearly in B [Fig. 4.2(d)].

Fig. 4.3 shows a rather peculiar ABS at $B = 40$ mT. It is superficially similar to the ABS in Fig. 4.2(c) because at zero magnetic field, its ground state at the particle-hole symmetry point is a magnetic doublet. However, in contrast to the ABS in Fig. 4.2(c), the number of resonances at finite field doubles even at the particle-hole symmetry point, where the ground state of the ABS is clearly one of the spin 1/2 states.

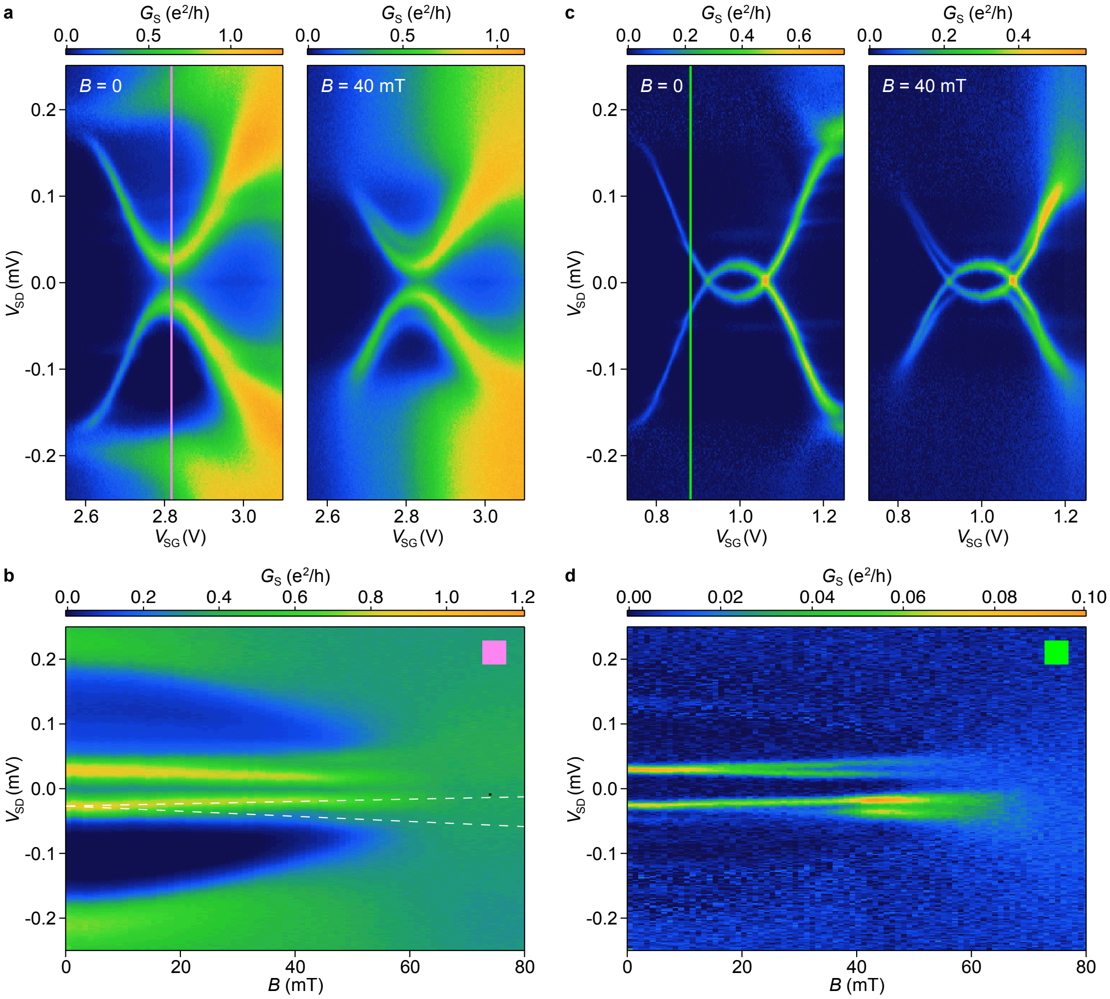

Figure 4.2: **a**, Singlet ground state ABS in an odd Coulomb valley. At finite fields (B = 40 mT), the number of resonances double (right panel). **b**, Magnetic field dependence of the SGRs at the particle-hole symmetry point (indicated by the pink line in **a**). **c**. ABS with a magnetic doublet ground state in an odd Coulomb valley. At B = 40 mT, the resonances between the zero-bias intersections do not split. **d**, Magnetic field dependence of the resonances outside the two zero-bias intersections.

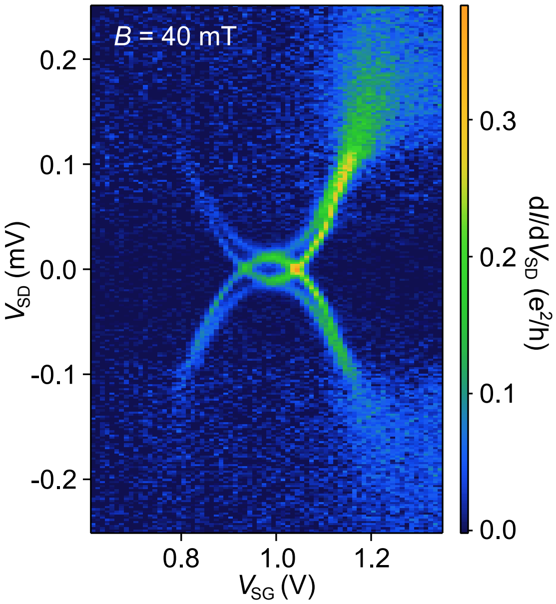

Figure 4.3: Zeeman split ABS at $B = 40$ mT. There are four distinct resonances even when the ground state of the ABS is a spin 1/2 state.

4.4 Discussion

When a single-level QD coupled to a superconductor is tuned to the middle of an odd Coulomb valley, the lowest energy states are a singlet state, $|S\rangle$, and a magnetic doublet, $|D\rangle = |\uparrow\rangle, |\downarrow\rangle$. Competition between the superconducting gap, Δ, the coupling to the superconductor, Γ_s, and the charging energy, U, determines which of the two states becomes the ground and the first excited states. Applying an external magnetic field lifts the degeneracy of the magnetic doublet (Fig. 4.4), while the spin zero singlet state remains unaffected.

Experimentally, a tunneling resonance occurs when an electron or a hole hops from the normal lead onto the QD, thereby inducing a single electron transition between the ground state and the first excited state. This single electron transition necessarily involves a parity change in the QD. In the case of a singlet ground state configuration

[Fig. 4.4(a)], the degeneracy of the first excited state, the magnetic doublet, is lifted linearly as the magnetic field is increased. Because both spinful states are individually odd and the singlet state has even parity, a single electron transition is allowed from the singlet ground state to both spin 1/2 states. Therefore, at finite fields, what was originally one single tunneling resonance now becomes two. This picture is consistent with our observations shown in Fig. 4.2(a) and 4.2(b). In Fig. 4.2(a), the ABS remains in the singlet ground state throughout the Coulomb valley. As expected, the number of resonances also doubles throughout the gate voltage range of the ABS at finite magnetic fields. At the particle-hole symmetry point, the linear splitting of the resonance is a measure of the Zeeman energy between the two spin states, $E_Z = \mu_\mathrm{B} g B$. From Fig. 4.2(b), we extract a g-factor of approximately 10. The experimental observations of a singlet ABS from a second device is also consistent with

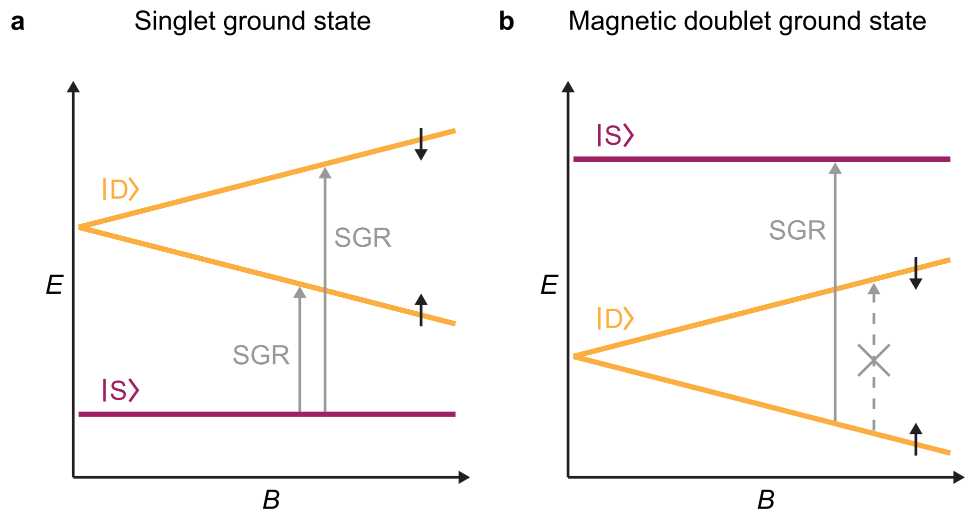

Figure 4.4: Lowest energy states of a S-QD system in the presence of an external magnetic field. (a), Singlet ground state configuration. Single electron transition from the ground state to both spin 1/2 states are allowed. (b) Doublet ground state configuration. When the degeneracy is lifted, a transition is only allowed between the lower energy spinful state (ground state) and the excited singlet state.

theoretical expectations, and for that device, we extract a g-factor of approximately 5 (see Section 4.6).

In contrast, when the ground state begins as a magnetic doublet, the only allowed transition is between the lower energy spin state and the singlet excited state, as illustrated in Fig. 4.4(b). Transition between $|\uparrow\rangle$ and $|\downarrow\rangle$ is disallowed because the two states have the same parity. As a result, even at finite magnetic fields, the number of distinct tunneling resonances remains unchanged. Experimental observation shown in Fig. 4.2(c) is largely consistent with this theoretical picture. Between the two zero-bias intersection points and centered about the odd Coulomb valley, the ground state of the ABS is a spin 1/2 state. At finite magnetic fields, only one pair of SGRs is observed near the particle-hole symmetry point.

However, under careful scrutiny, we notice discrepancies between experimental observation and expectations of the model illustrated in Fig. 4.4. Fig. 4.5 is a closeup of the QPTs in Fig. 4.2(c). Keeping in mind the ground state configuration of the ABS as a function of V_{BG} (demarcated with shaded bands in Fig. 4.5), we notice that the spin-split resonances do not terminate when the ground state switches from even to odd parity. Instead, the spin-split resonances continue in the spinful ground state configuration until they intersect at points indicated by orange arrows in Fig. 4.5.

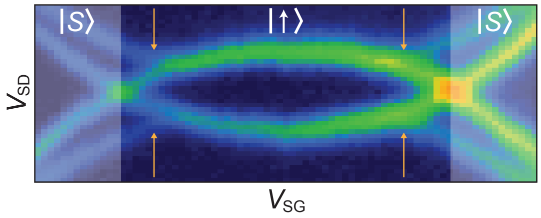

Figure 4.5: Close up of the QPTs in Fig. 4.2(c). The different ground states of the ABS is clearly demarcated, and the termination of the spin-split SGRs is indicated by orange arrows.

This effect is even more pronounced in the ABS shown in Fig. 4.3, where four distinct resonances exist throughout the entire gate voltage range of the ABS. These observations seemingly contradict the experimental results of Lee *et al* in Ref. [36], where the more energetic spin-split resonances stops abruptly at the gate voltage QPTs.

We suggest a possible mechanism for the additional resonances by carefully examining the intermediate configuration of lowest energy states between what is illustrated in Fig 4.4(a) and 4.4(b). When a singlet or a doublet ground state is near the QPT point in gate voltage space, additional Zeeman energy can result in a state configuration illustrated in Fig. 4.6, where the two spin 1/2 states sandwich the singlet state. Like the example in Fig. 4.4(b), the only allowed direct transition is between the $|\uparrow\rangle$ ground state and the $|S\rangle$ first excited state. However, provided that the bias voltage is sufficient, it is possible to execute a double transition from $|\uparrow\rangle$ to $|\downarrow\rangle$ via the $|S\rangle$ state since each transition changes the parity of the QD occupancy (the first and second transitions are indicated by the gray and blue arrows in Fig. 4.6). The double transition mechanism offers a second current path through the QD and thus registers as a second resonance in the tunneling differential conductance.

The double transition is allowed until a level crossing occurs between $|S\rangle$ and $|\downarrow\rangle$, the more energetic spin 1/2 state, which happens as the gate voltage is tune towards the particle-hole symmetry point. The points at which this occurs in V_{SG} is indicated in Fig. 4.5 by orange arrows. When the singlet state becomes the most energetic state, the only current carrying transition is between $|\uparrow\rangle$ and $|S\rangle$, thus only one tunneling resonance remains. This expectation is consistent with the termination point of the

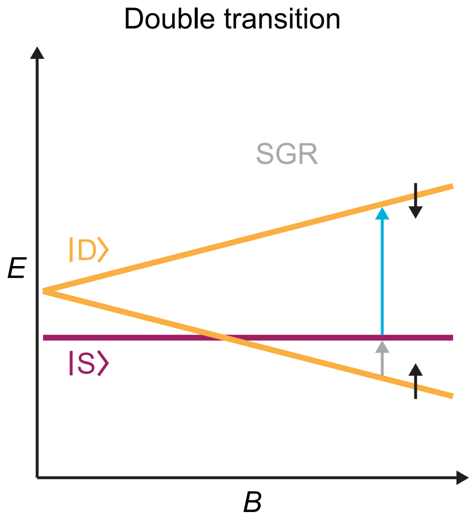

Figure 4.6: Lowest energy states of a hybridized QD near the QPT point. When $|S\rangle$ is sandwiched between $|\uparrow\rangle$ and $|\downarrow\rangle$, a double transition is allowed to happen between the two spin states by temporarily populating the singlet state (gray and blue arrows).

more energetic spin-split resonance in Figs. 4.2(c) and 4.5.

While the double transition is possible, we note that it becomes increasingly unlikely as Zeeman energy grows and the level separation becomes larger. This might explain the absence of an additional tunneling resonance in the observations of Lee *et al* in Ref. [36]. Their reported Zeeman splitting between the two spin 1/2 states is on the order of 100 μeV, while the Zeeman splitting in our devices at $B = 40$ mT is on the order of 10 μeV.

4.5 Conclusion

In summary, we observed Zeeman split tunneling resonances of ABS in QD-S devices. The tunneling spectrum of our devices is consistent with our theoretical expectations, and we suggest a possible higher order transition to explain the discrepancies between our experimental observations and those reported in Ref. [36].

4.6 Extraction of g-factor from second device

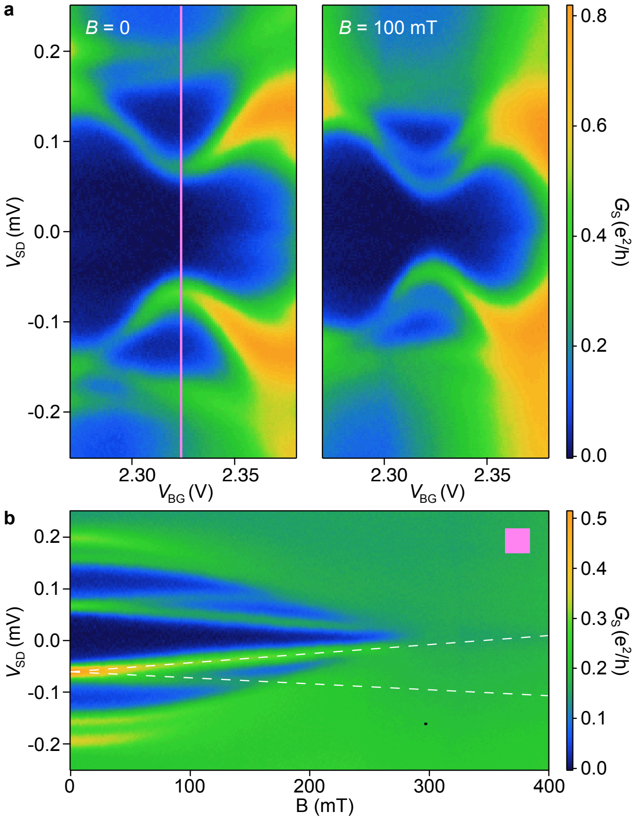

Figure 4.7: Device B. **a**, Singlet ground state ABS. The pair of resonances split into four distinct resonances at B = 100 mT. **b**, Magnetic field dependence of the resonances at the particle-hole symmetry point.

Fig. 4.7 shows a singlet ABS in a second InAs N-QD-S device. At B = 100 mT, the pair of symmetrical SGRs splits into two sets. At the particle-hole symmetry point, we examine the tunneling resonances as a function of V_{SD} and B. Because of the higher critical field of this device, the spin-split resonances are more readily resolved in Fig. 4.7(b). From this dataset, we extract a g-factor of approximately 5.

Chapter 5

Hard Superconducting Gap in Hybrid Epitaxial Semi-Super InAs-Al Nanowires

W. Chang[1,2], S. M. Albrecht[2], T. S. Jespersen[2], F. Kuemmeth[2], P. Krogstrup[2],
J. Nygård[2], and C. M. Marcus[2]

[1] *Department of Physics, Harvard University, Cambridge, Massachusetts 02138, USA*

[2] *Center for Quantum Devices, Niels Bohr Institute, University of Copenhagen,*
Universitetsparken 5, 2100 Copenhagen Ø, Denmark

5.1 Introduction

In this chapter, we present measurements of hard induced superconducting gap in epitaxially grown InAs-Al core shell nanowires. These hybrid nanowires come in two flavors, the first having a core that is completely covered by Al (full-shell), and the second having a core that is only half covered (half-shell). Both nanowire types display strong superconducting proximity effect in the InAs core, with sub-gap conductances up to two orders of magnitude lower than its normal state value. In addition, we find the conductance of the half-shell type to be gate dependent. The robust proximity effect, the hardness of the induced gap, and the gate-tunability of these hybrid nanowires make them an attractive platform on which induced p-wave superconductivity can be experimentally investigated.

5.2 The ‘soft’ gap quandary

The predicted existence of Majorana bound states in exotic phases of superconductivity [6] has garnered widespread attention because of their potential applications in topological quantum computation [9, 13–17]. Proposals to create a topological p-wave superconducting state by coupling a regular s-wave superconductor to a semiconducting nanowire with strong spin-orbit coupling and large g-factor are particularly alluring because the required ingredients are readily available [7, 8]. While zero-bias conductance peaks in tunneling spectroscopy measurements have been reported by numerous experiments on InAs and InSb nanowires [18–22, 59], a common experimental observation is the presence of a large amount of sub-gap density of states. The origin of this soft gap is unknown, and theoretical models have attributed its existence to interface roughness between semiconductor and superconductor [105], and to the inverse proximity effect of the normal metal tunneling probe [106]. On a grander scale, the soft gap represents a serious obstacle in the efforts to realize nanowire-based Majorana qubits because quasiparticle poisoning can nullify the highly coveted property of topological protection [107, 108].

5.3 The device

The InAs cores of the nanowires were grown axially in the wurzite [0001] direction with molecular beam epitaxy (MBE) [109]. After reaching lengths of 5–10 μm, Al was then grown radially around the core *in situ*. The resulting semiconductor-superconductor interface, shown in Fig. 5.1(c), is coherent, domain matched, and impurity free. Further details on the nanowire bicrystal growth can be found in Ref. [35]. Full-shell nanowires are completely covered by Al [Fig. 5.1(a)], while half-shell nanowires are only in contact with Al on two or three facets of the hexagonal core [Fig. 5.5(a)]. The core-shell (40 nm core diameter, 40 nm shell thickness) nanowires were deposited on a degenerately doped Si substrate with a 100 nm thermal oxide. We contacted the shell with a superconducting Ti/Al (5/130 nm) lead and the core with a normal metal Ti/Au (5/80 nm) lead. To expose the InAs core, an etchant that selectively targets Al was used. All contacts to the nanowire were made highly transparent by ion-milling away the native oxides *in situ* before metal deposition. Fig. 5.1(d) shows a SEM micrograph of a lithographically similar device.

To compare the quality of the induced superconducting gap between an epitaxi-

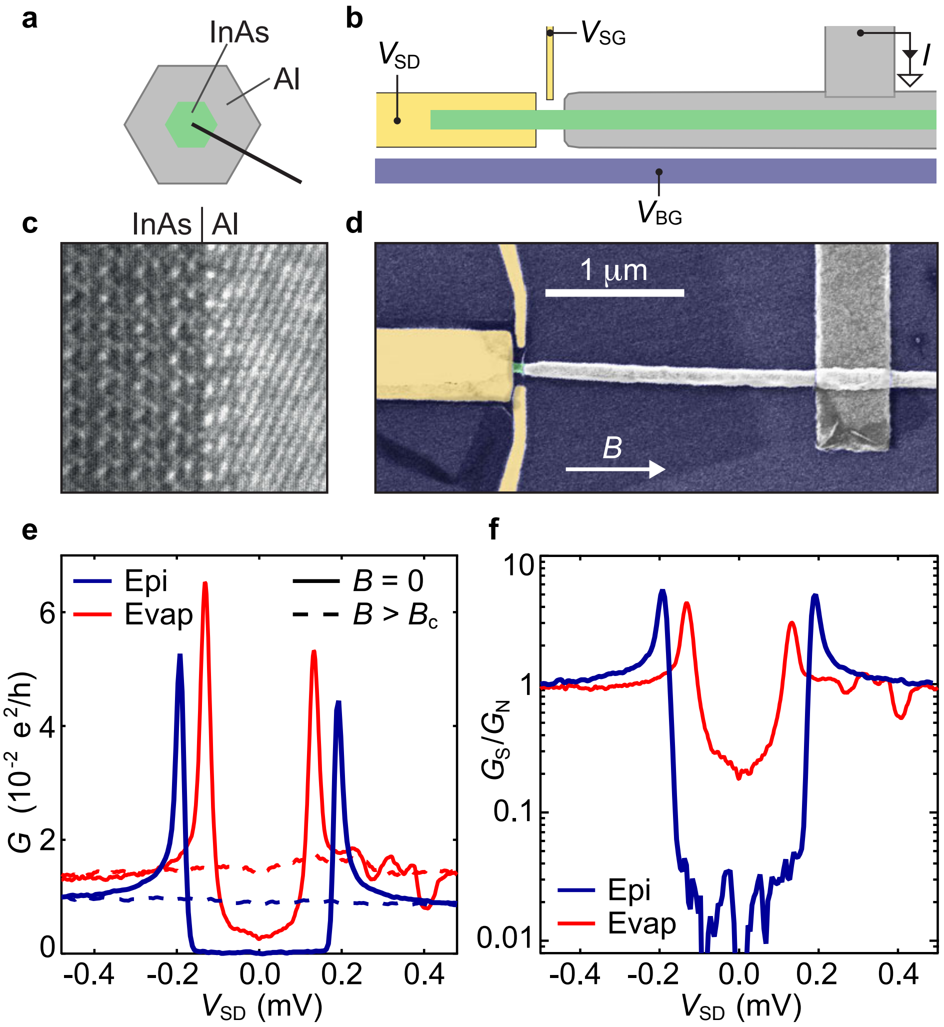

Figure 5.1: **Epitaxial full-shell device with a hard induced gap a**, Cross-section schematic of an epitaxial full-shell nanowire. **b**, Measurement set-up. Yellow represents normal metal (Au), green InAs, and gray superconductor (Al). **c**, TEM image of epitaxial N-S interface. **d**, False colored SEM micrograph of a lithographically similar device. **e**, Differential conductance as a function of source-drain voltage of an epitaxial full-shell device (blue) and an evaporated control device (red). Solid lines represent data at zero magnetic field while dashed lines represent data at fields above the critical magnetic field, B_c. **f**, Normalized differential conductance. Epitaxial full-shell nanowires exhibit a sub-gap conductance suppression of up to two orders of magnitude.

ally defined N-S interface and an evaporated N-S interface, we separately fabricated control devices using similar nanowires. In these devices, the entirety of the shell was removed with Al etchant. We replaced the shell with evaporated Al in select areas to create a device similar to its epitaxial counterpart [Figs. 5.1(b) and 5.1(d)], with the exception that the underside of the InAs core is in contact with the substrate and not Al. We found it necessary to introduce a 5 nm Ti sticking layer between the nanowire and the evaporated Al film in these control devices because numerous devices fabricated without the sticking layer showed poor induced gap and a highly disordered sub-gap spectrum (see section 5.8.1). We thus compare gap measurements from epitaxial full-shell and half-shell devices against control devices proximitized via an evaporated Ti/Al (5/50 nm) 'half-shell'. The measurement schematic for all devices is shown in Fig. 5.1(b). The carrier density in the exposed core can be tuned with a sidegate voltage, V_{SG}, or a backgate voltage, V_{BG}. In this experiment, we use only the backgate. Unless stated otherwise, the external magnetic field, B, was applied parallel to the length of the nanowire. All measurements were performed in a dilution refrigerator with a base temperature of 20 mK.

5.4 Measurements

We first bring the devices into a tunneling regime ($G \ll G_0 = 2e^2/h$) by reducing V_{BG}. The tunneling spectrums of an epitaxial full-shell device (blue) and an evaporated device (red) are shown in Fig. 5.1(e). In the superconducting state ($B = 0$) both devices exhibit peaks in differential conductance at symmetrical source-drain voltages, V_{SD}. Between these two peaks, conduction is suppressed. The peaks and dip disappear as we increase B above the critical magnetic field, B_{c} ($\sim$75 mT for epitaxial full-shell and $\sim$250 mT for evaporated control). In the normal state, both devices show similar tunneling conductances of approximately 0.01 e^2/h [dashed lines in Fig. 5.1(e)]. We refer to the differential conductance in the $B = 0$ superconducting state as G_{S}, and the differential conductance in the $B > B_{\mathrm{c}}$ normal state as G_{N}. In Fig. 5.1(f), we compare the normalized tunneling conductance ($G_{\mathrm{S}}/G_{\mathrm{N}}$) of the two devices. The epitaxial full-shell device shows an induced gap of $\Delta^* = 190\ \mu\mathrm{eV}$, similar to the superconducting gap of bulk Al, and a sub-gap conductance suppression of up to two orders of magnitude. The evaporated control device shows a smaller induced gap of 140 μeV, and a sub-gap conduction suppressed by at best a factor of 5, similar to reported experiments in proximitized InAs and InSb nanowires [18–22, 59].

Increasing V_{BG} increases both sub and above-gap conductances of the epitaxial full-shell device. A pair of sub-gap resonances (SGR) appears close to the gap edge in the range $-11\ \mathrm{V} < V_{\mathrm{BG}} < -8\ \mathrm{V}$ [Fig. 5.2(a)]. The appearance of this SGR coincides with a sharp increase in the above-gap conductance. The rest of the tunneling spectrum is devoid of other SGRs. In this device, no evidence of dot-like charging physics was observed [Fig. 5.2(b)]. Conductance peaks independent of V_{BG} occur at $V_{\mathrm{SD}} = 190\ \mu\mathrm{V}$, and in some areas the sub-gap conductance exceeds the normal state conductance. This sub-gap conductance enhancement is illustrated in Fig. 5.2(c), which shows two vertical cuts taken at low and high backgate voltages [indicated by orange and green lines in Figs. 5.2(a) and 5.2(b)]. In Fig. 5.2(d) we plot the superconducting zero-bias conductance as a function of conductance at $V_{\mathrm{SD}} = 0.4$ mV. On the same graph, we plot, with no free parameter, the theoretical dependence between $G_{\mathrm{S}}(V_{\mathrm{SD}} = 0)$ and $G_{\mathrm{N}}(V_{\mathrm{SD}} = 0)$, given by the following expression in Blonder-Tinkham-Klapwijk-Beenakker (BTKB) theory [44, 110]

$$G_{\mathrm{S}}\big|_{V_{\mathrm{SD}}=0} = 2G_0 \frac{G_{\mathrm{N}}^2}{(2G_0 - G_{\mathrm{N}})^2} \tag{5.1}$$

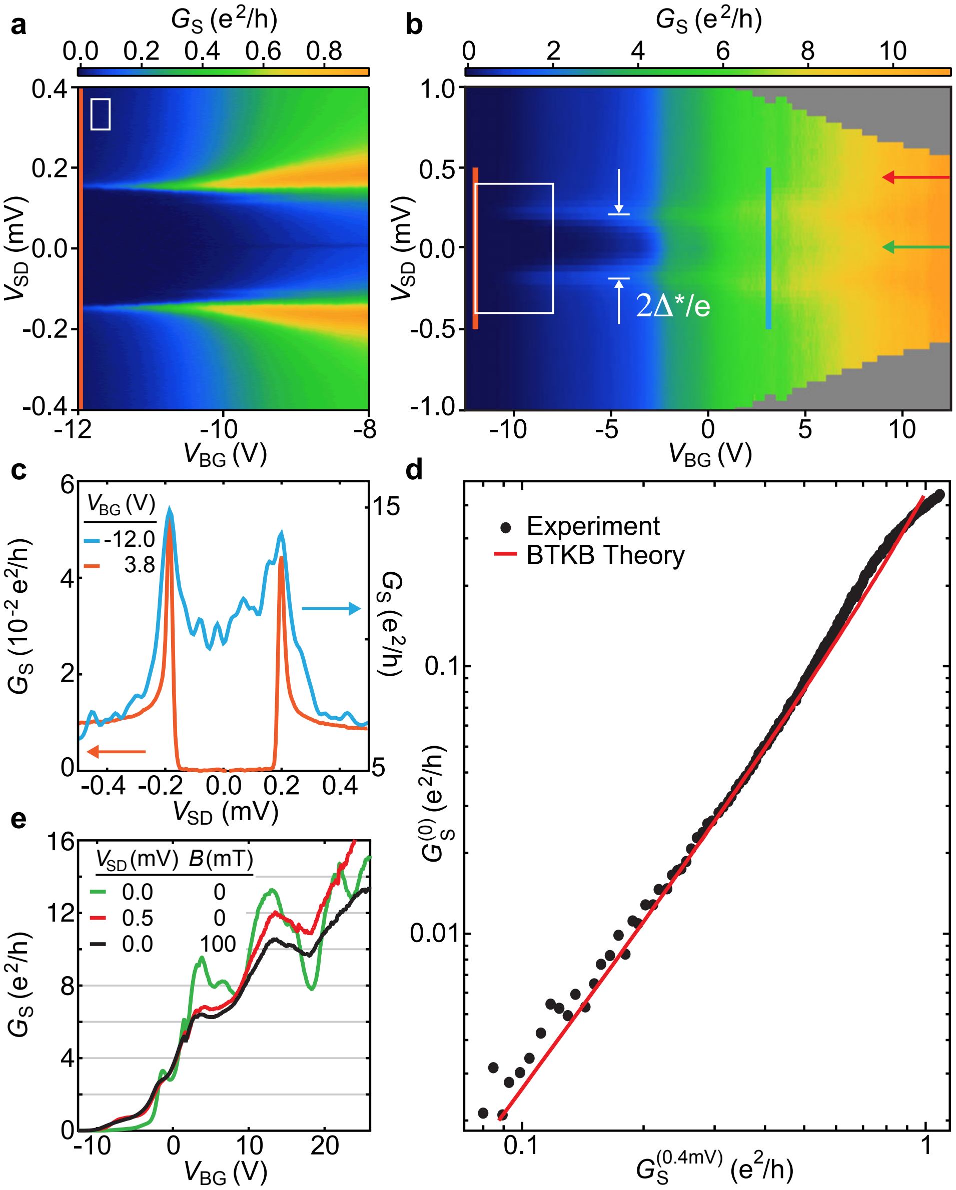

Figure 5.2: **Conductance of a ballistic one-dimensional N-S junction in an epitaxial full-shell device**. **a**, **b**, Differential conductance of a full-shell device as a function of backgate, V_{BG}, and V_{SD}. **c**, Vertical cuts of **a** and **b** in the tunneling (orange), and open (blue) regimes. **d** Zero-bias versus finite-bias (0.4 mV) conductance. The solid line (red) represents the theoretical relation between the two quantities. **e**, Conductance steps as a function of V_{BG} at zero-bias, above-gap bias, and normal state ($B = 100$ mT $> B_c$).

The device also exhibits conductance steps as a function of V_{BG} [Fig. 5.2(e)], a typical signature of quantum point contacts (QPC). Zero-bias conductance in the

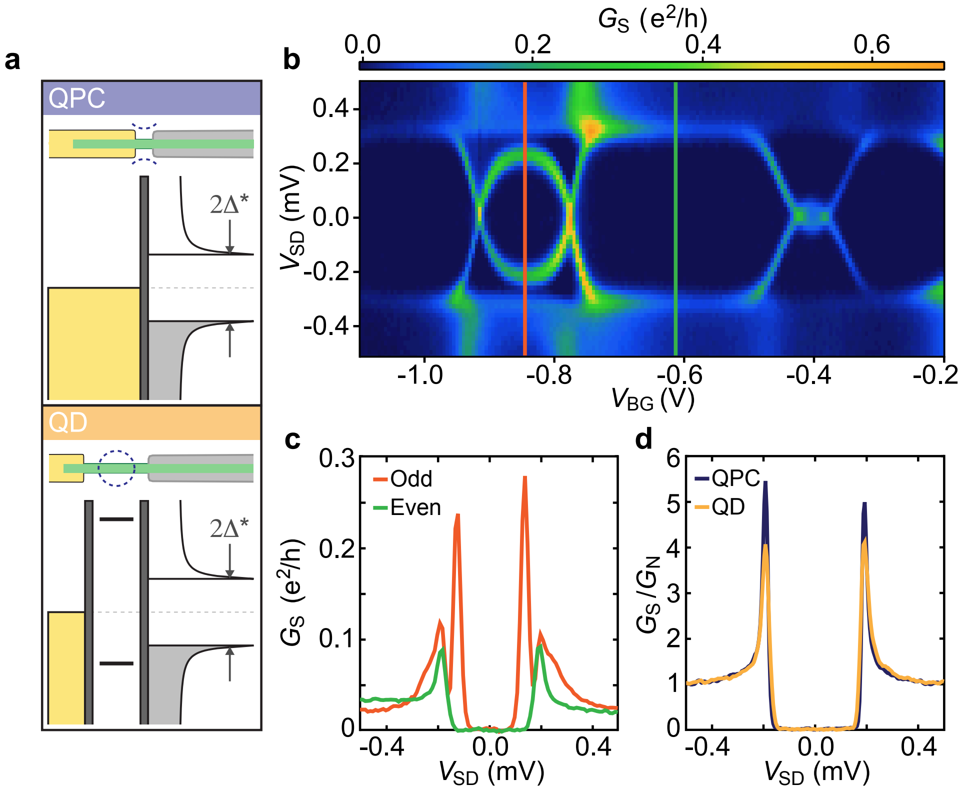

Figure 5.3: **Epitaxial full-shell quantum point contact vs quantum dot devices. a**, Tunneling spectrum of a proximitized InAs core coupled to a QPC (upper panel) and QD (lower panel). **b**, Andreev bound states in a quantum dot. The green (orange) line indicates the particle-hole symmetry point of an even (odd) Coulomb diamond. **c**, Vertical cuts of **b**. **d**, Comparison of tunneling measurements between a QPC device and a QD device in an even valley.

normal state (black line) shows plateaus at values close to 1, 3, 6, and 10 e^2/h. In the superconducting state and at source-drain bias above Δ^*/e (red line), the device conductance shows a similar behavior, but the begins to deviate above 6 e^2/h. Plateaus are less defined at zero-bias in the superconducting state (green line). Instead, conductance oscillates around the normal state values and peaks on the lower V_{BG} edge of the normal state plateaus.

Not all of the measured devices, epitaxial or evaporated, form QPCs. Instead, a quantum dot (QD) can form in the exposed InAs core [Fig. 5.3(a)]. In the normal state of an epitaxial full-shell QD device, Coulomb diamond resonances and well defined even-odd structures can be identified (see supplementary information). In the superconducting state, symmetric SGRs in the shape of inverted bells occupy the odd diamond valleys [Fig. 5.3(b)]. These SGRs, arising from Andreev bound states (ABS) or Yu-Shiba-Rusinov states (YSR) [69–71, 75, 76], have been extensively investigated in previous studies [36, 59, 64, 66, 93–95, 97]. Similar QD structure and their associated SGRs in the superconducting state are also observed in our control devices. Vertical cuts at the particle-hole symmetry point of an odd (orange) and even (green) Coulomb valley are shown in Fig. 5.3(c). Away from the SGRs, both even and odd Coulomb valley traces show highly suppressed sub-gap conductances. We compare the normalized conductance of an epitaxial full-shell QPC device against an epitaxial full-shell QD device tuned to the middle of an even Coulomb valley [Fig. 5.3(d)]. The two measurements are almost indistinguishable, and this experimental observation allows us to compare induced gap measurements between various devices, regardless of their QPC or QD nature. Since fabricated QPC devices are of a rarer variety than QD devices in nanowire systems, all comparisons between epitaxial and evaporated devices are between the epitaxial full-shell QPC device and an evaporated QD device.

In Figs. 5.4(a) and 5.4(b) we study the evolution of the induced gap as a function of magnetic field and temperature. We then compare the normalized zero-bias conductance of an epitaxial full-shell device against an evaporated control device in Figs. 5.4(c) and 5.4(d). Since the sub-gap conductance in epitaxial devices is close to our experimental noise-floor, we average over a 40 μV window centered about zero-bias and define this value as $G_S^{(0)}/G_N^{(0)}$. Experimental error bars smaller than

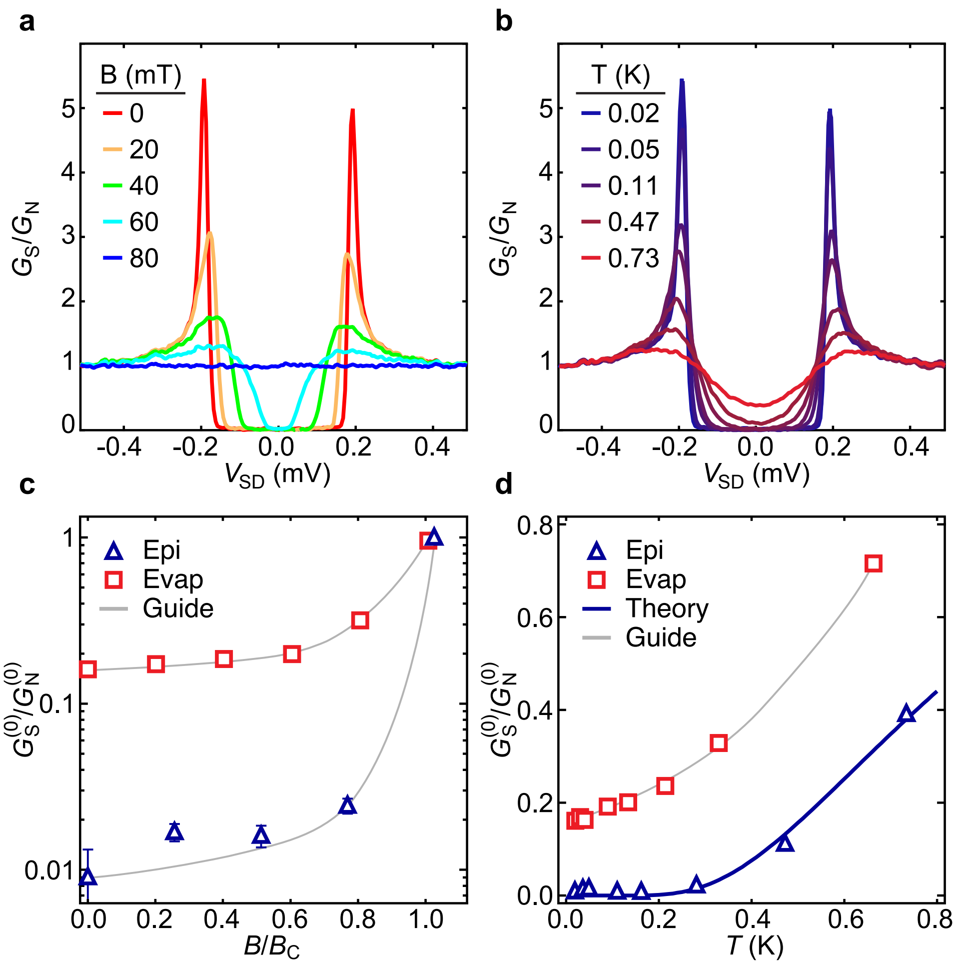

Figure 5.4: **Magnetic field and temperature dependence of induced gaps.** **a**, Magnetic field dependence of an epitaxial full-shell device. **b**, Temperature dependence of an epitaxial full-shell device. **c**, Comparison of normalized zero-bias conductance between the epitaxial device and a control device as a function of normalized magnetic field. **d**, Comparison of normalized zero-bias conductance between the epitaxial device and an evaporated control device as a function of temperature. Gray lines in **c** and **d** are guides to the eye, and the blue line in **d** is a theoretical fit to the data.

the marker size in Figs. 5.4(c) and 5.4(d) are not shown. For better comparison, we normalize the applied magnetic field by the critical fields of each device in Fig. 5.4(c). Fig. 5.4(d) shows the normalized zero-bias conductance as a function of temperature. We fit the temperature dependent tunneling conductance of a N-S junction in BCS theory to data from the epitaxial full-shell device. The theoretical dependence is

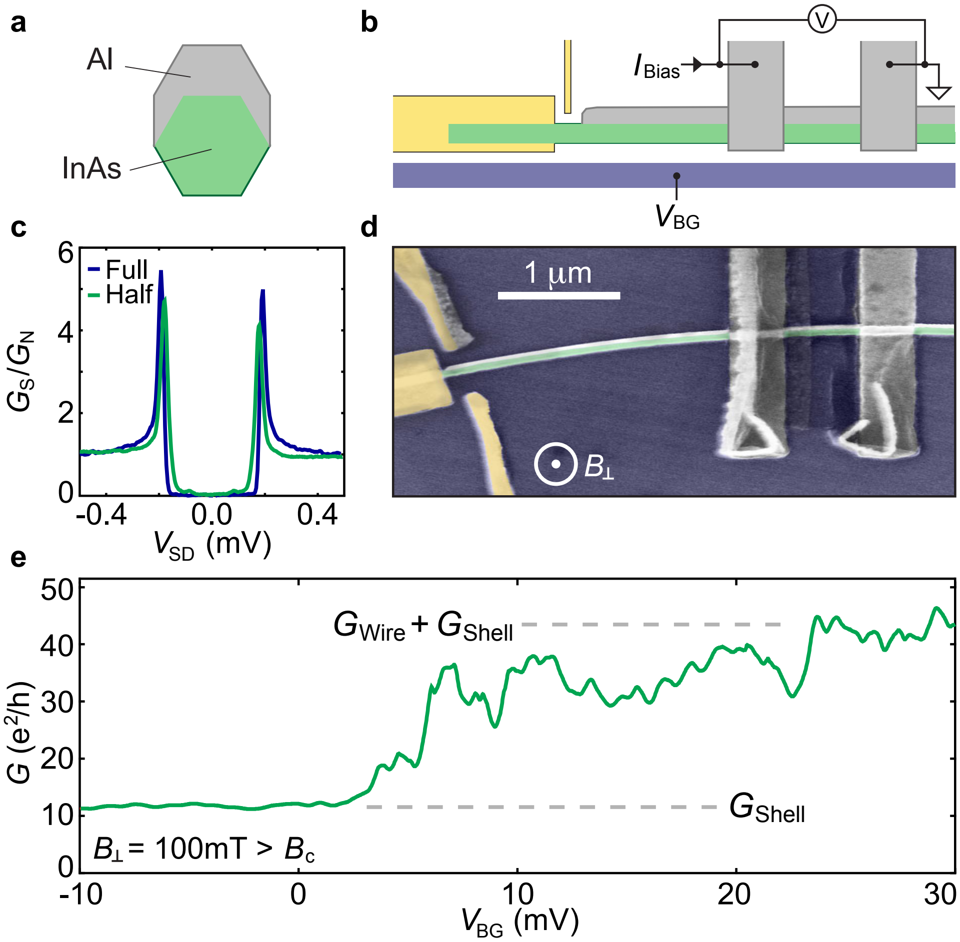

Figure 5.5: **Epitaxial half-shell device and gate-tunability of InAs core a**, Cross-section illustration of a half-shell nanowire. **b** Gate-tunability measurement schematic of a half-shell nanowire device. **c**, Comparison of induced gap quality between an epitaxial full-shell and half-shell device. **d**, SEM micrograph of a lithographically similar device. **e**, conductance of the Al shell and InAs core as a function of V_{BG}.

given by the expression [38]

$$\left.\frac{G_S}{G_N}\right|_{V_{SD}=0} = \sqrt{\frac{2\pi\Delta^*}{k_B T}}\, e^{-\Delta^*/k_B T} \tag{5.2}$$

, where k_B is the Boltzmann constant and T is the temperature. From the theoretical fit (blue line), we extract an induced gap of 160 μeV.

We fabricate similar devices on epitaxial half-shell nanowires [Figs. 5.5(a), 5.5(b), and 5.5(d)], with the exception that an additional Al lead is added to the device, and these leads now contact both the shell and the core. Identical tunneling spectroscopy is performed on these devices, and we compare the induced gap quality of the full-shell QPC device to a half-shell QD device in Fig. 5.5(c). The induced gap size of an epitaxial half-shell device (180 μeV) is similar to the induced gap size in epitaxial full-shell devices. The normalized sub-gap conductance is a factor of 50 lower than the normal state conductance, substantially better than the induced gap in evaporated control devices.

The additional Al lead to the shell allows us to explore the gate-tunability of the half-exposed InAs core. As illustrated in Fig. 5.5(b), we apply a current bias between the two Al leads and measure the voltage drop when the device is in the normal state ($B_\perp = 100$ mT $> B_c$). Conductance through the normal state Al shell and the semiconducting InAs core is shown in Fig. 5.5(e). It remains roughly constant at 10 e^2/h below $V_{\mathrm{BG}} = 3$ V, then rises to approximately 45 e^2/h at much higher V_{BG}.

5.5 Discussion

Normalized sub-gap conductance suppression of up to two orders of magnitude represents a significant improvement in the hardness of induced gaps in InAs nanowires [19,21,59,94]. This number should be regarded as a lower bound limited by the experimental noise floor of our measurement set-up [Fig. 5.1(f)]. While we cannot isolate the effects of a Ti sticking layer on the hardness of the proximitized gap, we note that our control devices fabricated without the sticking layer have produced far inferior induced gaps. The collective measurements across multiple devices, epitaxial and evaporated, suggests that the soft gap is a result of semiconductor-superconductor interface roughness [105]. Commonly practiced methods of proximitizing these nanowires require the removal of native oxides either via chemical etching or physical ion-milling before the deposition of a superconducting metal. These fabrication steps can potentially damage the crystalline semiconductor surface.

Interface quality aside, the QPC nature of our epitaxial full-shell device demonstrates ballistic transport in the semiconducting core. The only SGR present in the QPC device [Fig. 5.2(a)] coincides in V_{BG} with the the first conductance plateau in the normal state. We interpret this resonance as an ABS formed from the first sub-band of a one-dimensional channel [41].

In the tunneling limit, we approximate the normal state conductance by the quasiparticle transport conductance measured at sufficiently high source-drain bias ($V_{\mathrm{SD}} = 0.4$ mV $> \Delta^*/\mathrm{e}$). Comparing this value against the zero-bias superconducting state conductance, we find excellent agreement between experiment and BTKB theory [44, 110] [Fig. 5.2(d)]. What is remarkable is that the comparison between experiment and theory has no free parameter. The zero-bias superconducting state conductance of a single channel N-S junction depends solely on the transmission coefficient, τ, which, in Landauer formalism, is directly proportional to the normal state conductance. Measurement noise notwithstanding, the striking similarity between experiment and theory tells us that the hardness of the induced gap is close to its theoretical limit.

Further agreement with BTKB theory can be found by comparing sub-gap conductances between the tunneling regime and the open transport regime [Fig. 5.2(c)].

At low backgate voltages, the probability of Andreev reflection [111] is low because of a high tunnel barrier [Fig. 5.3(a), upper panel] between the normal lead and the proximitized InAs core [44]. At high backgate voltages, the barrier is lowered and the sub-gap conductance is enhanced above its normal state value. However, we note that there remains a finite probability for an electron to specular reflect against the proximitized core. This is evident from the fact that the sub-gap conductance never reaches twice its normal state value.

Conductance steps as a function of backgate voltage are evident in Fig. 5.2(e), but the steps do not occur at typical QPC values. The discrepancy could be attributed to imperfect transmission of one-dimensional conduction modes [112] and additional symmetries in the transverse confining potential of the nanowire [113]. In addition, while we have subtracted line resistances from our measurement set-up, we cannot account for additional contact resistances within the device.

While QPCs and QDs represent vastly different transport regimes in a nanowire, both types of devices allow us to perform tunneling spectroscopy on the proximitized core. As illustrated in Fig. 5.3(a), a QPC near pinch-off forms a single tunnel barrier between the normal electrode and the InAs core. On the other hand, a single QD can be envisioned as two tunnel barriers with discrete states in between. Since the charging energy of the reported QD device is larger than the induced gap Δ^*, when V_{BG} is tuned to the particle-hole symmetry point of an even Coulomb diamond, the discrete QD states are far from the edge of the induced gap. The QD thus acts as a single tunnel barrier between the normal lead and the proximitized InAs core. The agreement of tunneling spectroscopy measurements between the QPC and the QD device [Fig. 5.3(c)] serves as an experimental validation of this interpretation.

In Figs. 5.4(a) and 5.4(c), we note that the floor of the induced gap remains close to zero, rising sharply only when B approaches B_c. Retaining a hard gap at finite magnetic fields is an important trait for Majorana bound state experiments since theoretical framework requires that the Zeeman energy in the semiconductor be larger than the induced s-wave pairing gap [6–8]. While the temperature dependent tunneling conductance from BCS theory [38] qualitatively fits our experimental observation [Fig. 5.4(d)], the extracted induced gap of 160 μeV does not coincide with our tunneling spectroscopy measurement of $\Delta^* = 190$ μeV. Alternatively, one can interpret this discrepancy as an effective device temperature that is roughly a factor of 1.2 larger than the measured temperature of the dilution refrigerator. Although the actual electron temperature can be higher than the cryostat temperature, we expect the two values to agree fairly well at elevated temperatures above 100 mK.

Turning our attention to the epitaxial half-shell variety of nanowires, we find that the induced gap has similar hardness to their full-shell cousins [Fig. 5.5(c)]. More interestingly, in the normal state of the Al shell, the conductance between the two Al leads is gate-dependent. The resistance saturates at about 2.5 kΩ below $V_{\mathrm{BG}} = 3$ V, and lowers to about 600 Ω at higher backgate voltages [Fig. 5.5(e)]. We interpret the saturated resistance to be the resistance of the Al shell, and the subsequent reduction of resistance to come from the opening of a parallel conduction channel through the InAs core. Using the capacitance model from Ref. [114], we estimate the following transport parameters for the InAs core: (i) carrier density (at high V_{BG}), $n = 5 \times 10^{18}$ cm^{-3} (ii) mobility, $\mu = 3300$ cm^2/Vs (iii) elastic scattering length,

$l_e = 100$ nm. These are typical values for InAs nanowires reported in Refs. [115,116]. However, the expected resistance for our Al shell should be on the order of 10^1 Ω. The higher measured resistance could be attributed to additional contact resistance between the Al leads and the Al shell.

5.6 Conclusion

While epitaxial full-shell nanowires provide interesting geometries (cylindrical superconducting shell) for future experiments, it is probably the epitaxial half-shell variety that strongly interests the Majorana community. The possibility of controlling the sub-band occupation in a large spin-orbit, large g-factor quasi-one-dimensional semiconductor while maintaining a hard induced superconducting gap makes the epitaxial half-shell nanowire an ideal platform for nanowire-based Majorana qubits.

5.7 Acknowledgements

We thank N. L. B. Ziino, and K. Flensberg for fruitful discussions. Support was received from Microsoft Project Q, the Danish National Research Foundation, the Carlsberg Foundation, the Villum Foundation, and the Lundbeck Foundation.

5.8 Additional information

5.8.1 Evaporated control devices

Without Ti sticking layer

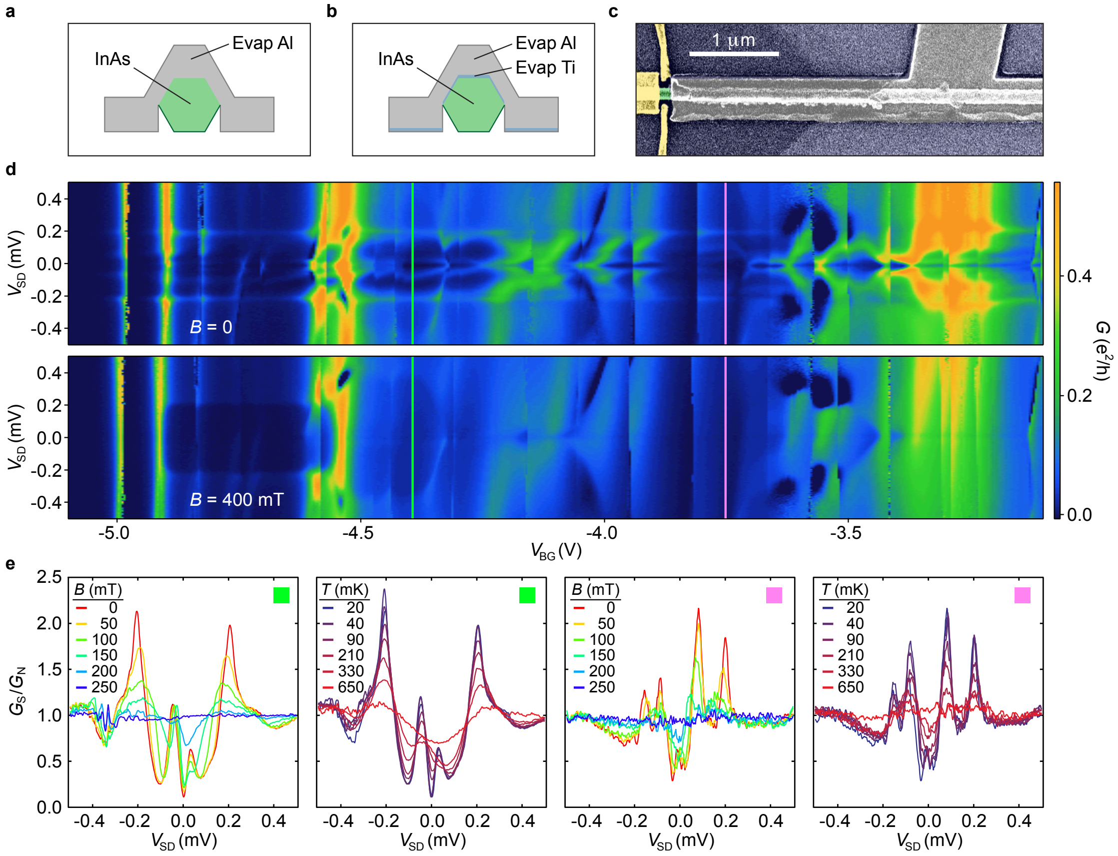

Figure 5.6: **Geometry and measurements of evaporate control devices (without Ti sticking layer).** **a** and **b**, Cross-section schematic of control devices with evaporated Al film and evaporated Ti/Al film. **c**, False color SEM micrograph of a lithographically similar control device. **d**, Differential conductance as a function of V_{SD} and V_{BG}. **e**, Vertical cuts of **d** at various magnetic fields and temperatures.

Epitaxial half-shell nanowires from the same growth were used for both the epitaxial half-shell devices and the evaporated control devices. For the control, all of the native Al shell was chemically removed. Al, or Ti/Al (Ti being the sticking layer), was then evaporated onto the remnant InAs core to create a final device similar to the one shown in Fig. 5.6(c). Figs. 5.6(a) and 5.6(b) illustrate the cross-sectional profile of these control devices.

In this section we focus only on evaporated control devices without a Ti sticking layer. Fig. 5.6(d) shows the differential conductance of a control device as a function of V_{SD} and V_{BG}. The lower panel shows data from the same region in V_{BG}, but taken at $B = 400$ mT $> B_{\mathrm{c}}$. The device appears to be highly switchy as the tunneling spectrum is discontinuous in V_{BG}. We can see faint suggestions of Coulomb diamond structures, but the lack of a clear even-odd structure tells us that there are potentially multiple ill-defined QDs in the InAs core. In the superconducting state, there is a backgate-independent induced gap below $|V_{\mathrm{SD}}| \sim 200$ μV. Populating the device tunneling spectrum are numerous SGRs. The gap and the SGRs originate from the superconducting proximity effect since they disappear at magnetic fields above B_{c}.

At no point in V_{BG} of this device are we able to avoid the SGRs. This makes extracting the minimum normalized sub-gap conductance difficult. Our best attempts are shown in Fig. 5.6(e), at backgate voltages indicated by the vertical green and pink lines in Fig. 5.6(d). We show the evolution of the tunneling spectrum as a function of magnetic field and temperature. In these examples, the normalized sub-gap conductance suppression is at best a factor of 5. Four evaporated control devices without Ti sticking layers were measured, and all of them showed similar behavior.

With Ti sticking layer

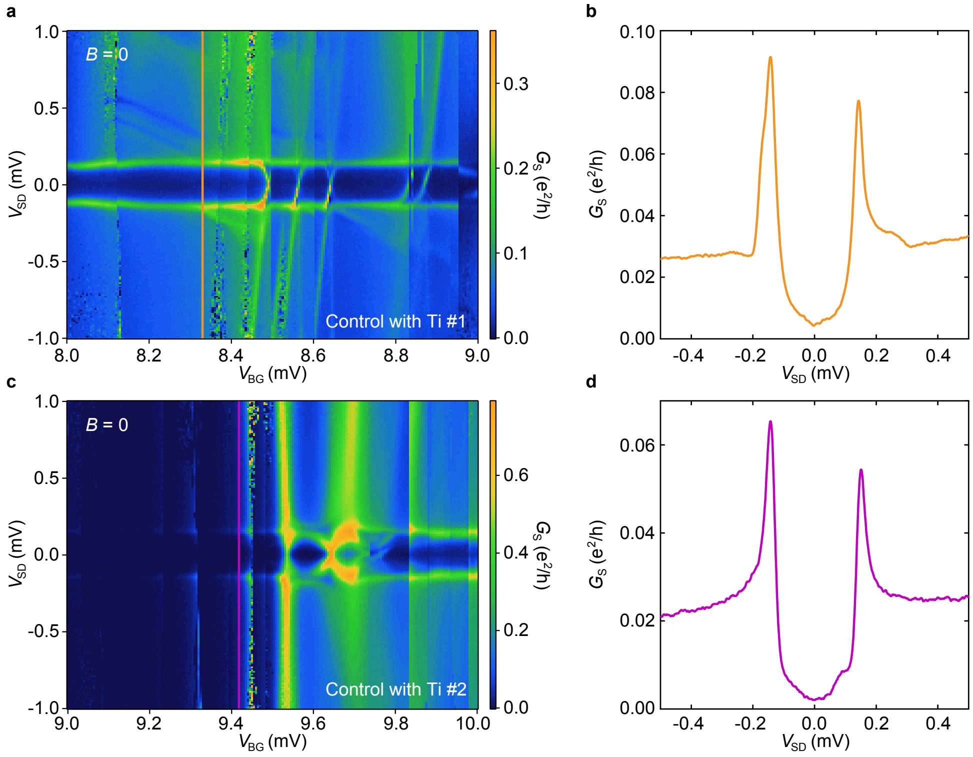

Figure 5.7: **Tunneling spectrum of two evaporated control devices with a Ti sticking layer.** **a** and **c**, Tunneling spectrums as a function of V_{SD} and V_{BG} of control devices #1 and #2. **b** and **d**, Induced gap measurements of the evaporated control devices taken at V_{BG} values indicated by the orange and purple lines in **a** and **c**.

Fig. 5.7 shows the tunneling spectrum of two evaporated control devices with Ti sticking layers. Both devices are switchy (discontinuities in V_{BG}), but compared to devices without a Ti sticking layer, it is now possible to move away from the SGRs and extract a minimum normalized sub-gap conductance. It is also possible to identify odd and even Coulomb valleys by the SGRs and the Kondo resonances. Figs. 5.7(b) and 5.7(d) show conductance traces at V_{BG} values indicated by the orange and purple lines in Figs. 5.7(a) and 5.7(c).

5.8.2 Epitaxial full-shell QPC device – a focus on the first ABS

Additional data on the single ABS in the epitaxial full-shell QPC device is shown in Fig. 5.8. Data shown in Fig. 5.8(a) is identical to data shown in Fig. 5.2(a). Here, we change the aspect ratio to place emphasis on the ABS. Fig. 5.8(b) shows the evolution of the induced gap and the ABS as a function of magnetic field. The ABS remains close to the gap edge, then merges into the continuum above $B \sim 40$ mT. It shows up most prominently as two peaks in an one-dimensional trace taken at V_{BG} = -10 V [Fig. 5.8(c)].

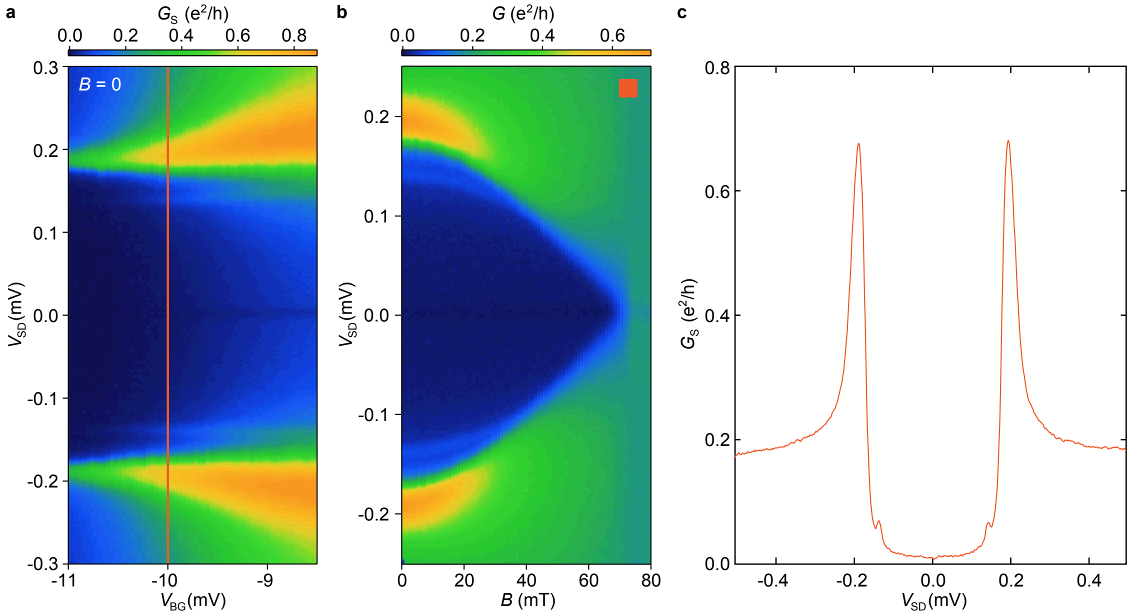

Figure 5.8: **ABS of the first sub-band in the epitaxial full-shell QPC device.** **a**, Tunneling spectrum below the first conductance plateau. A pair of horizontal SGRs can be seen at the edge of the induced gap. **b**, Magnetic field dependence of the SGRs. **c**, Vertical cut of **a** (orange line), showing two small conductance peaks at the edge of the induced gap.

5.8.3 Epitaxial full-shell QD device

We turn our attention to measurements from epitaxial full-shell QD devices. Distinct Coulomb diamond resonances with charging energy on the order of 1 meV can be seen in Fig. 5.9. Furthermore, even-odd structure can be seen from the presence of both Kondo resonances (normal state) and SGRs (superconducting state) in every other Coulomb diamond. QD data shown in Fig. 5.3(d) is taken at the particle-hole symmetry point of an even Coulomb diamond [indicated by the pink line in Fig. 5.9(a)].

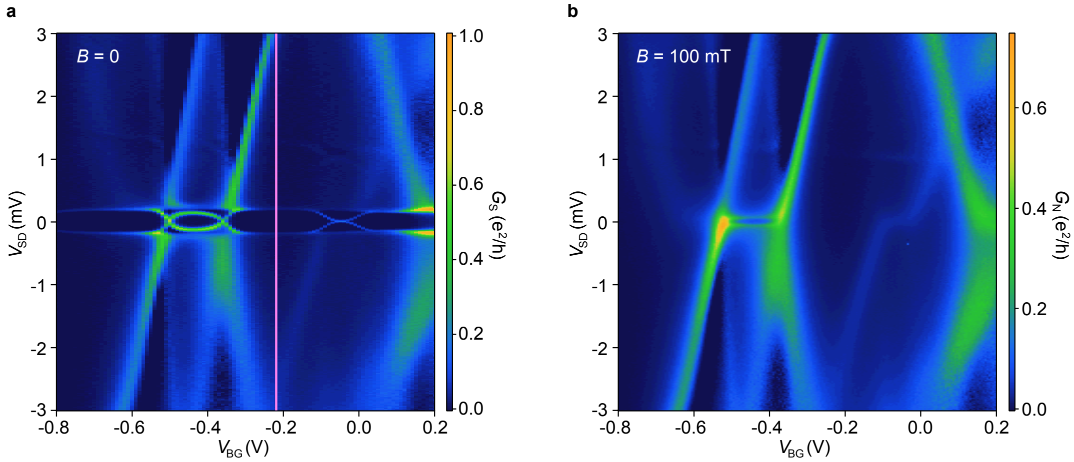

Figure 5.9: **Charge stability diagram of an epitaxial full-shell QD device.** **a** and **b**, Differential conductance as a function of V_{SD} and V_{BG} at $B = 0$ and $B = 100$ mT respectively. Pink line in **a** indicates the backgate voltage at which the induced gap measurements shown in Figs. 5.3(c) and 5.3(d) is taken.

5.8.4 Epitaxial half-shell QD device

Three epitaxial half-shell QD devices were measured. In Figs. 5.10(a) and 5.10(b) we show the charge stability diagrams of one of the devices at zero and at finite magnetic fields. The QD nature of this device is evident from Coulomb diamonds,

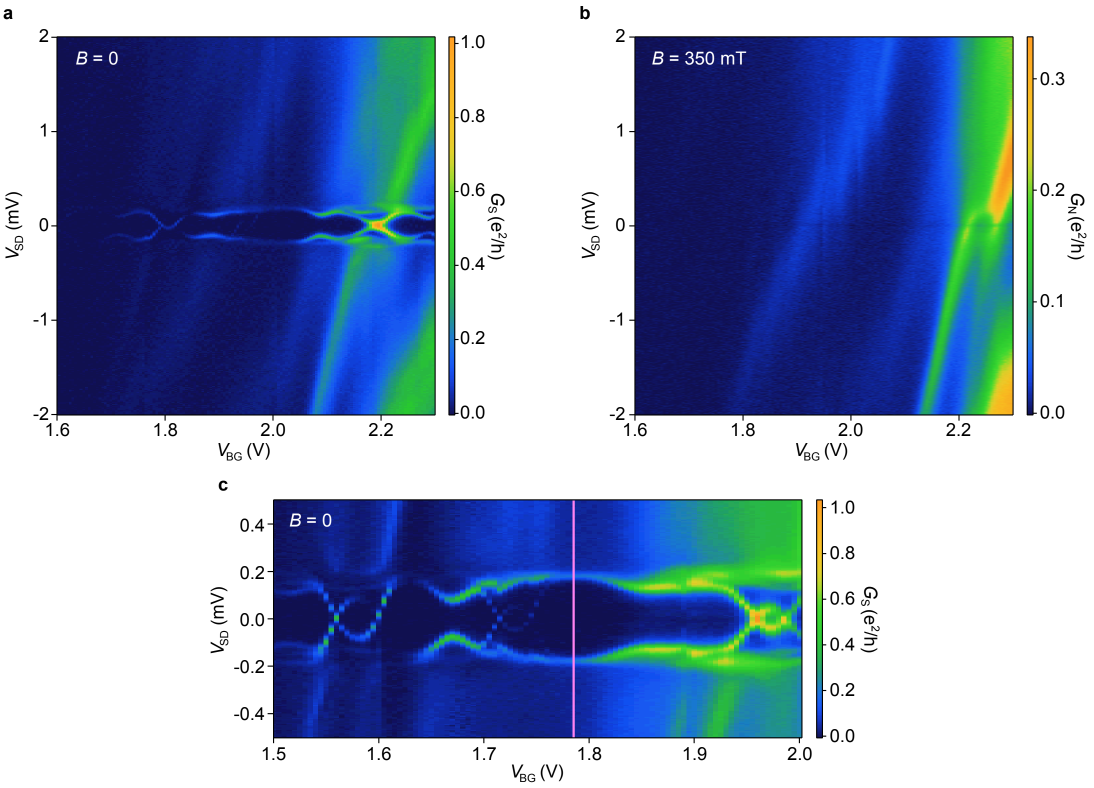

Figure 5.10: **Charge stability diagram of an epitaxial half-shell QD device.** **a** and **b**, Charge stability diagram of the device at $B = 0$ and $B > B_c$. Coulomb diamonds with charging energy on the order of 1 meV are evident. In the normal state, a spin-split Kondo resonance occurs near $V_{BG} = 2.2$ V. **c**, Close-up of the sub-gap spectrum in the backgate voltage range of **a** and **b**; numerous SGRs are visible. The pink line indicates the backgate voltage value at which the induced gap measurement shown in Fig. 5c is taken.

and its charging energy is on the order of 1 meV. In the normal state [Fig. 5.10(b)], we see a pair of spin-split Kondo resonances near $V_{BG} = 2.2$ V. In the superconducting state, the Kondo resonance turns into a pair of SGRs [Fig. 5.10(a)]. To extract a measurement of the induced gap, we move away from the SGRs in V_{BG}. Data shown in Fig. 5.5(c) is taken at a backgate voltage value indicated by the pink line in Fig. 5.10(c).

Chapter 6

Gate-Tunability of Epitaxial Half-Shell Nanowires

6.1 Introduction

One of the key criteria to induce a topological phase in a super-semi hybrid structure is to be able to tune the chemical potential of the one dimensional semiconductor into the induced superconducting gap. Furthermore, the number of occupied subbands must be odd in order for the zero-energy Majorana mode to manifest [6–10,37]. It was unclear if this was experimentally feasible, because proximitizing semiconducting nanowires usually involved placing large pieces of superconductors on top of, and in good contact to, the target semiconductor. The presence of a metal could screen the effectiveness of gate electrodes, and the good contact to a metal could potentially dope the semiconductor and increase its carrier density.

In the previous chapter, we saw that the normal state ($B > B_c$) conductance of a segment of an epitaxial half-shell nanowire varies as a function of backgate voltage, V_{BG}. In this chapter, we further investigate the superconducting properties of these epitaxial half-shell nanowires as a function of V_{BG} and magnetic fields in various directions.

In addition to a gate-dependent normal state resistance, we observe that the maximum supercurrent carried by the S-nanowire-S Josephson junction varies with V_{BG}. The maximum supercurrent also varies as a non-monotonic function of applied magnetic field – a signature similar to Fraunhofer interference in Josephson junctions. From the local minima (in magnetic field) of the supercurrent, we extract an effective area of the Josephson junction. The calculated effective cross-sectional areas of the Josephson junction are consistent with the lithographic dimensions of the device. Moreover, the areas diminish as V_{BG} is reduced.

The consistent backgate dependence of normal state resistance, maximum supercurrent, and effective area of these nanowires indicates that the chemical potential of a well proximitized nanowire can be controlled experimentally.

6.2 Device schematic

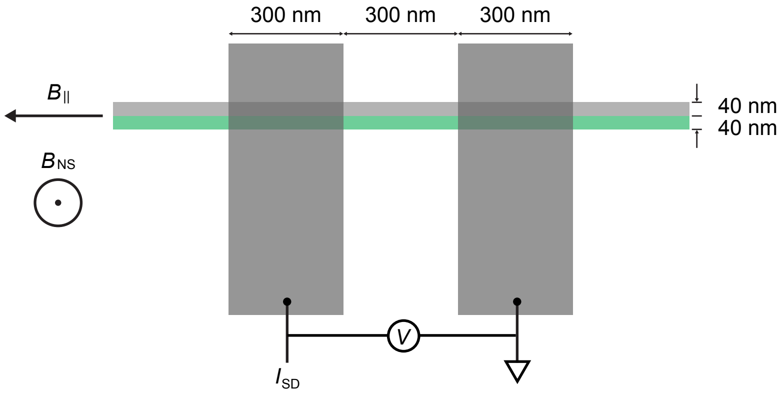

Figure 6.1: Device and measurement schematic of an epitaxial half-shell Josephson junction. Both core (pastel green) and shell (light gray) are contacted by evaporated Al to form two Josephson junctions in parallel – S-c-S and S-InAs nanowire-S. A bias current can be injected into the junctions through the Al leads, and the potential difference across the leads is measured. External magnetic field can be applied in various orientations relative to the length of the nanowire.

The measured epitaxial half-shell device is similar to devices described in the previous chapter. We focus only on the segment of nanowire between two evaporated superconducting Ti/Al (5/50 nm) leads (Fig. 6.1). The leads were lithographically designed to straddle both the InAs core and the Al shell of the nanowire. To make good electrical contact to the nanowire, we ion-milled away native oxides of the nanowire with Ar. The milling condition was optimized to remove Al_2O_3. Since InAs oxide and InAs are less resistant to Ar ion milling than Al_2O_3, it is likely that the InAs core underneath the leads was over-milled. Nonetheless, the Al shell should remain largely intact and good electrical contact was made between nanowire and leads.

The 300 nm wide Ti/Al leads were spaced 300 nm apart. From SEM images of the nanowires, we estimate the shell to be 40 nm thick and the core to be 40 nm in diameter. SEM images also indicate that the epitaxial half-shell nanowires tend to lie sideways, with the shell and the core both visible when looking down at the substrate (as illustrated in Fig. 6.1, where the page is in the plane of the Si substrate). The degenerately doped substrate provided a global backgate voltage, and we measured the voltage drop across the two leads as we applied a current bias, I_{SD}.

6.3 Measurements

We begin by defining three magnetic field orientations. With a vector magnet, we apply an in-substrate-plane magnetic field and define the direction of the largest supercurrent critical field as $B_{||}$. This direction is consistent with the major axis of the nanowire, as determined from SEM and optical images of the device. With the nanowire orientation determined, we apply a magnetic field perpendicular to the length of the nanowire. The direction perpendicular to the nanowire and with the largest supercurrent critical field is defined as B_{Minor}. This direction turns out to be roughly in the plane of the substrate. Finally, we define the magnetic field normal to the substrate as B_{NS}.

Fig. 6.2 shows the differential resistance of the device as a function of I_{SD} and B_{Minor} at various backgate voltages. We subtract the line resistance of the measurement circuit to offset the differential resistance at low bias currents and low magnetic fields to zero. Data is acquired in the direction of positive to negative magnetic

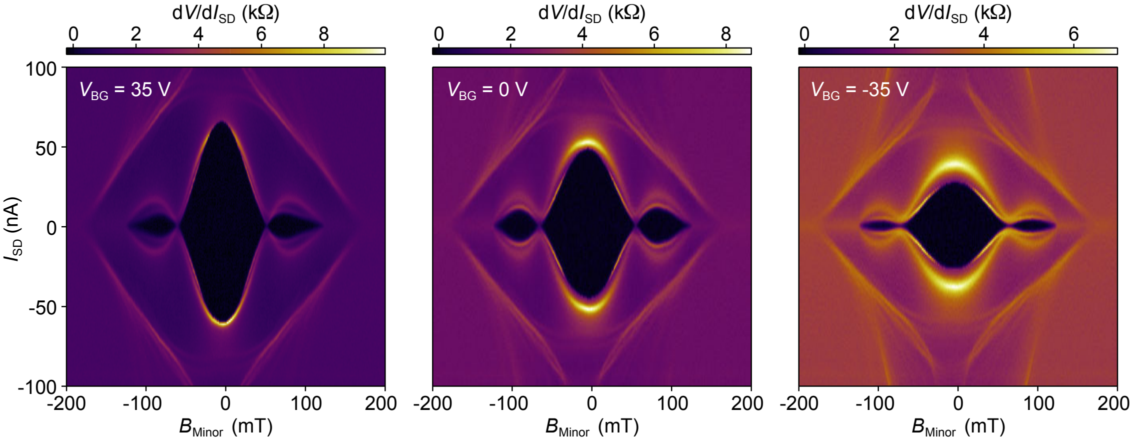

Figure 6.2: Differential resistance of the hybrid Josephson junctions as a function of current bias and B_{Minor} at three different backgate values. The resistance in the normal state and the size of the maximum supercurrent increases and decreases respectively with a decreasing backgate voltage.

field and negative to positive current bias. The resistance of the device switches abruptly to a finite value above a switching current, I_{S}, on the positive bias side, and below a re-trapping current, I_{R}, on the negative bias side. Both switching and re-trapping currents have a non-monotonic dependence on the applied magnetic field. They encounter a local minima around $B_{\text{Minor}} = 70$ mT, and finally vanishes above $B_{\text{Minor}} = 120$ mT. We identify the latter as the critical field of the superconducting leads in the B_{Minor} direction. The overall pattern of I_{S} and I_{R} as a function of magnetic field resembles a Fraunhofer interference pattern [38, 117].

As we reduce the backgate voltage (going from left to right on Fig. 6.2), the maximum values of I_{S} and I_{R} decrease. In addition, the normal state resistance at high fields ($B_{\text{Minor}} = 200$ mT) increases. Similar characteristics are shown in Fig. 6.3, where we change the direction of the applied field to B_{NS}. The differences are that the device switches to the resistive branch at a much smaller field, $B_{\text{NS}} = 40$ mT, and the local minima of the switching and re-trapping currents happen around $B_{\text{NS}} = 30$ mT.

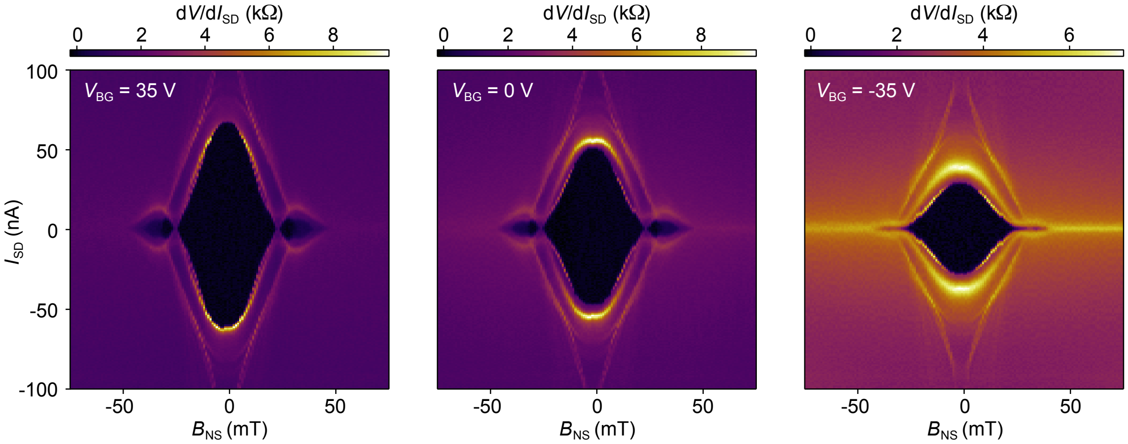

Figure 6.3: Differential resistance of the hybrid Josephson junction as a function of current bias and B_{NS} at three different backgate values. The critical field of the junction is smallest in this magnetic field direction, and the first minima in supercurrent occurs at a much smaller value.

In Fig. 6.4, we turn to the last magnetic field direction. The critical magnetic field in this direction is about $B_{\mathrm{MA}} = 300$ mT, and more importantly, Fraunhofer interference-like patterns are absent.

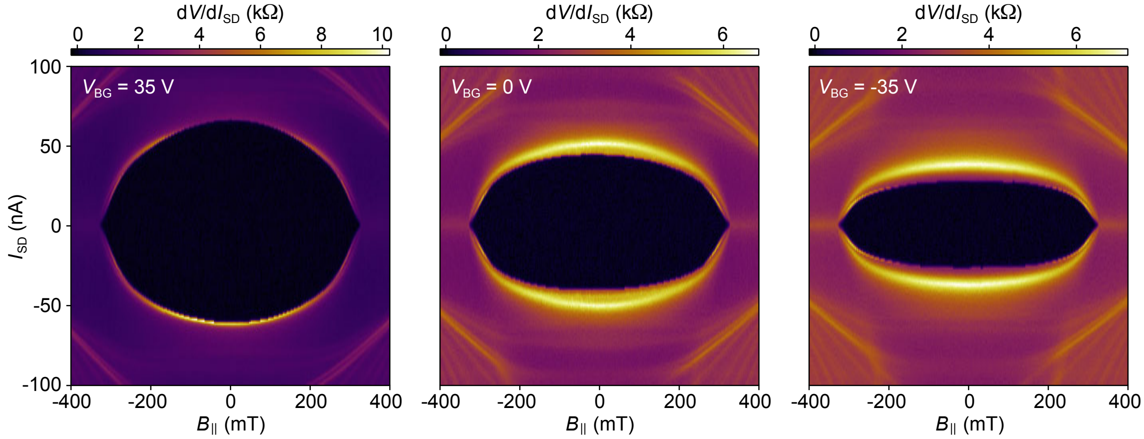

Figure 6.4: Differential resistance of the hybrid Josephson junction as a function of current bias and $B_{||}$. No Fraunhofer-like interference pattern can be seen when the magnetic field is aligned with the length of the nanowire, presumably because the incident area is miniscule. The critical field of the device is also largest in this direction.

Because of the direction of data acquisition, the graphs in Figs. 6.2, 6.3, and 6.4

are not necessarily symmetric and centered about the origin. Generally, switching and re-trapping currents in an underdamped Josephson junction do not have the same magnitude [38]. Sweeping the magnetic field between large values can also be hysteric. We take horizontal cuts of the graphs in Figs. 6.2 and 6.3 at I_{SD} values where the critical fields are the largest and plot them in Fig. 6.5.

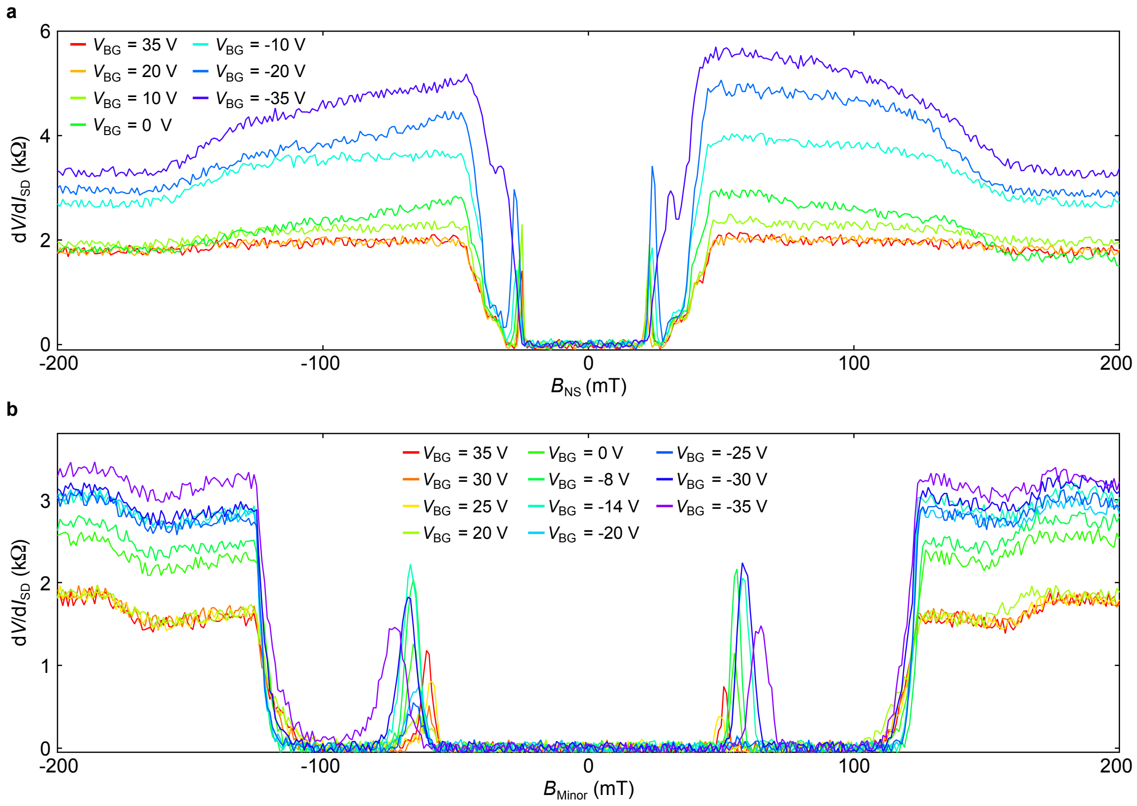

Figure 6.5: Zero-bias (after compensating for hysteresis) differential resistance of the hybrid Josephson junction as a function of B_{NS} in (a) and as a function of B_{Minor} in (b), at various backgate voltages. The first minima in the switching current can be identified by a peak in resistance. The normal state resistance and the magnetic field value at which resistance peak occurs increase with decreasing backgate voltage.

Similarly, we take vertical cuts of Figs. 6.2 and 6.3 at magnetic field values where I_{S} and I_{R} are largest and plot them in Fig. 6.6. Panels (a) and (b) of each figure show cuts from the B_{NS} and B_{Minor} dataset respectively. It is evident from the figures

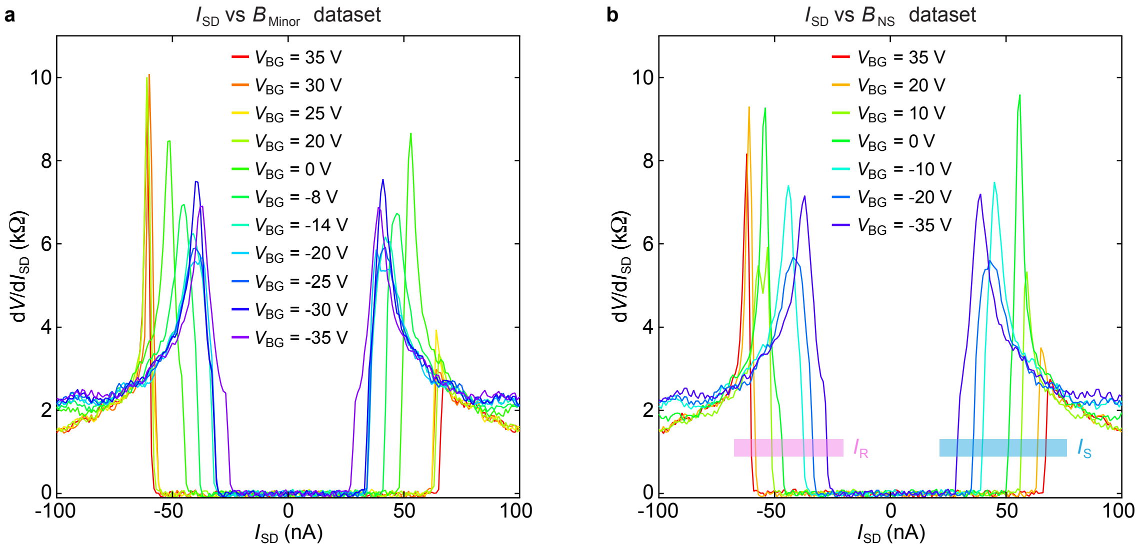

Figure 6.6: Switching and re-trapping currents of the hybrid Josephson junction at zero magnetic field (after compensating for hysteresis) at various backgate voltages. Values extracted from the I_{SD} vs B_{Minor} dataset are shown in (a). Likewise, values extracted from the I_{SD} vs $B_{\mathrm{NS|}}$ dataset are shown in (b). We also differentiate the switching and re-trapping currents with colored boxes in (b).

that the normal state resistances rise with decreasing backgate voltage. The switching and re-trapping currents also decrease as backgate voltage is reduced (Fig. 6.6). More interestingly, the local resistance maxima, which coincides with the local minima of I_{S} and I_{R}, varies as a function of backgate. The magnetic fields at which they occur increase with a decreasing V_{BG}.

6.4 Discussion

The measured device, illustrated in Fig. 6.1, can be interpreted as a parallel combination of a S-constriction-S and a S-semiconductor-S Josephson junction, where the Al shell of the nanowire is the superconducting constriction. A Josephson supercurrent is driven between the two evaporated superconducting leads, and magnetic fields can penetrate the nanowire because the supercurrent density is not large enough for the Meissner effect to manifest. In fact, the thin superconducting leads should also allow flux penetration, reminiscent of the intermediate laminar state of a Type-I superconducting slab [38, 118].

Treating the device as an extended Josephson junction, the Fraunhofer-like dependence of I_S and I_R as a function of applied magnetic field can then be attributed to the interference between supercurrent paths. In rectangular junctions with negligible magnetic field screening, the interference pattern is a Fraunhofer diffraction pattern. The local minima of maximal supercurrent occur at integer multiples of the superconducting flux quanta, $\Phi_0 = h/2e$.

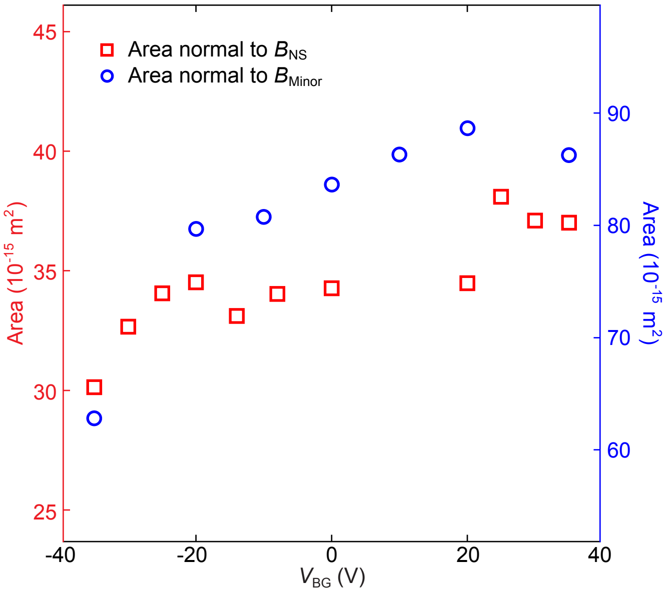

Figure 6.7: Assuming that the first zero-bias resistance maxima coincides with one flux quantum through the Josephson junction, the incident area of the magnetic flux is plotted in this graph. Red square markers (read against left axis) is the cross-sectional area normal to B_{NS} of the Josephson junction. Blue circular markers (read against right axis) is the cross-sectional area normal to B_{Minor}.

In the strictest sense, the measured device is not a rectangular extended Josephson junction. Nonetheless, we can use the Fraunhofer picture to estimate the effective incident area of magnetic flux. Using the magnetic field value of the local maxima in resistance from Fig. 6.5, we can extract a corresponding area for the Josephson junction. We plot the results in Fig. 6.7. Incident area in the B_{Minor} direction is plotted against the red axis (left) and incident area in the B_{NS} direction is plotted against the blue axis (right). In the B_{Minor} direction, which is perpendicular to the length of the wire and roughly in the plane of the substrate, the effective area of the Josephson junction is about 35×10^{-15} m^2. If we assume flux penetration of the superconducting leads, the length of the Josephson junction would be 900 nm. This means that the width of the junction is about 40 nm, consistent with the lithographic height of an epitaxial half-shell nanowire that's lying on its side.

Next, in the B_{NS} direction, the cross-sectional area of the Josephson junction is about 80×10^{-15} m^2. Once again, assuming a length of 900 nm gives a width of approximately 90 nm. This is also consistent with a half-shell nanowire that has a shell thickness and a core diameter of approximately 40 nm each. Most importantly, the effective area in both magnetic field directions decreases as the backgate voltage is reduced. One interpretation is that as the carrier density in the InAs core is reduced, parts of the wire become depleted and do not contribute to the effective area of the Josephson junction. This interpretation is consistent with the rising normal state resistance, R_{N}, and the reducing switching current.

We plot the extracted values of I_{S} and R_{N} from Figs. 6.5 and 6.6 in Figs. 6.8(a) and 6.8(b). In an ideal tunneling Josehpson junction, the product of the critical Josephson current and the normal state resistance should follow the Ambegaokar-Baratoff relation given in Eq. (2.35). Since it is experimentally very difficult to extract the critical current of a Josephson junction, we approximate I_{C} with the switching

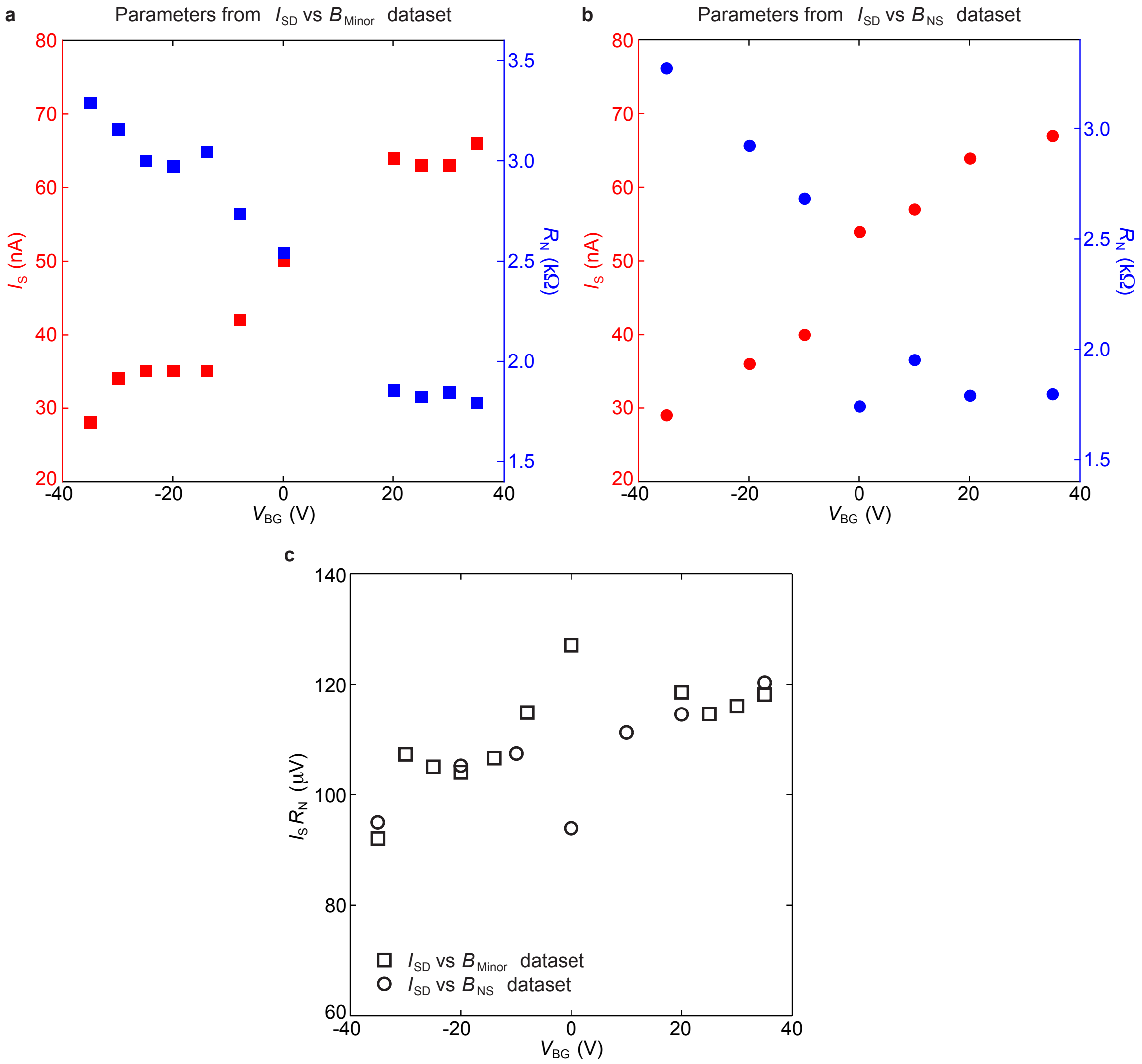

Figure 6.8: (a) and (b) Switching current (red, left axis) and normal state resistance (blue, right axis) as a function of backgate voltage. Values extracted from the I_{SD} vs B_{Minor} and I_{SD} vs B_{NS} dataset are shown in (a) and (b) respectively. (c) Product of I_{SD} and R_N as a function of backgate voltage.

current instead. The product $I_S R_N$ is shown in Fig. 6.8(c).

The superconducting order parameter of the leads should be around $|\Delta| \sim 200$ μeV. We thus expect the product $I_S R_N$ to be some where close to 300 μeV. However, it is not surprising for the experimental estimates to fall short of the theoretical value, since the switching current is not the critical current and the critical current could in principle be much higher than the measured values. Furthermore, the Josephson junction is likely diffusive and contacts to the nanowire can be imperfect. Both of these factors can contribute to a reduced critical current [45]. Even though there is an unexpected gate-dependence of $I_{\mathrm{S}}R_{\mathrm{N}}$, the variation is not large and the product is largely constant.

6.5 Conclusion

The normal state resistance, the maximum supercurrent, and the effective area of a segment of half-shell nanowire contacted by two superconducting leads are three independently measured variables. The backgate-dependence of these three variables are consistent with one another, and points towards a gate-tunable proximitized semiconductor.

Chapter 7

Speculations and Possibilities

The core-shell nanowires provide a few advantages to an experimentalist: (i) hard superconducting gap (ii) sharp tunneling resonances (iii) ease of fabrication (iv) patterning small pieces of Al onto InAs nanowire while maintaining good electrical contact (v) thin pieces of Al that can withstand large magnetic fields (vi) thin, cylindrical Al that wraps around the InAs core (applicable only to full-shell variety) (vii) automatic suspension of the InAs core above the sample substrate (applicable only to full-shell variety). With these qualities in mind, let us explore the quick and dirty experiments that are readily within grasp. Do note that these are incomplete ideas born out of informal discussions with various people. The purpose of this chapter is not to claim credit for these ideas, but to document those that I think are interesting and feasible.

7.1 Spin-orbit resolved ABS at finite superconducting phase difference

Most proposals to induce p-wave superconductivity in nanowires require two crucial ingredients to coexist with proximity effect – (i) few and odd one-dimensional sub-band occupation (ii) strong spin-orbit coupling. The first criteria has been observed in a few transport measurements where the maximum supercurrent through a ballistic nanowire Josephson junction was demonstrated to be quantized in steps [34, 48]. These observations were attributed to supercurrent carrying ABSs originating from ballistic one-dimensional conduction channels as described by Beenakker in Ref. [41], and our discussion in Section 2.5.1. Our experiments discussed in Chapter 5 have also demonstrated quantized conduction steps in a N-QPC-S device, and on top of that, showed direct tunneling resonances of the first sub-band ABS. Nonetheless, it would be reassuring to observe direct tunneling resonances of ABSs from higher transverse modes of the nanowire, and to investigate their magnetic, spin-orbit, and superconducting phase dependences.

One of the biggest problems with nanowires is their relatively short mean free paths. While improvements in materials growth can minimize stacking faults and impurities in the crystals, nanofabrication processes will inevitably trash the nanowires. This is aggravated by the fact that nanowires are relatively naked compared to two-dimensional electron gas (2DEG) systems which are buried deep within protective heterostructures.

A solution would be to imitate 2DEG systems and add a non-conductive shell

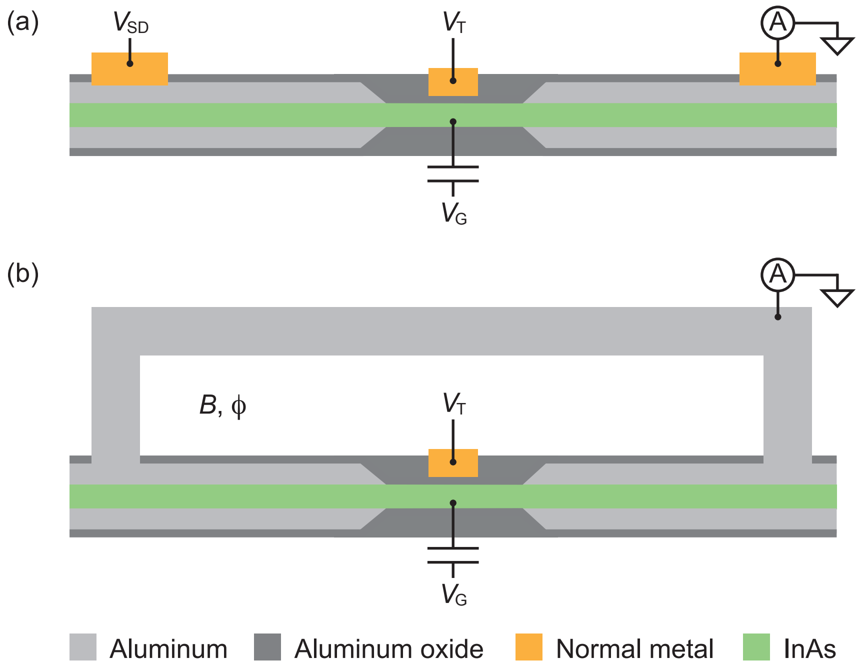

Figure 7.1: (a) Proposed QPC Josephson junction device. An epitaxial full-shell device is anodized in the middle to produce a QPC. Normal contacts are laid down on both ends of the Al shell. An optional tunnel probe can be deposited in the middle after selectively thinning parts of the Al_2O_3 shell to make a tunnel barrier. (b) Proposed phase-controlled QPC Josephson junction device. Measurement capability across the junction is sacrificed to connect a phase-controlling superconducting loop to both ends of the device. Tunneling spectroscopy of the InAs QPC is achieved via the central tunnel probe.

to the nanowire. While this passivates and protects the surface of the core from chemical processes, it still doesn't avoid the inevitable trashing when ohmic contacts have to be fabricated onto the nanowires. Another solution would be to do what Krogstrup *et al* have done, which is to make the shell out of a metal (even better, a superconductor!). This solves the problem of making ohmic contacts to the nanowire core, because all one has to do is to contact the metal instead. However, since metal is now everywhere, they have to be removed at some points along the nanowire in order to fabricate sensible semiconducting devices. Not only would the metal handle most of the current transport, it would also shield the semiconducting nanowire from gate defined electric fields. This returns us to square one, since the nanowire core is once again exposed to the elements.

But what if we could combine both solutions by turning metal into insulator at will? David Tuckerman and Burton Smith from Microsoft inspired the following solution by suggesting the controlled anodization of Al. Let us begin with an epitaxial full-shell InAs/Al nanowire described in Chapter 5. Contacts to the Al shell can be easily made without damaging the InAs core (simply remove the native Al_2O_3). Instead of removing the Al shell between the contacts to make a S-N-S junction, we can selectively turn parts of the Al shell into Al_2O_3 via electrolytic anodization in a borate bath. The areas to be anodized can be defined with a patterned resist layer, and the depth of anodization is easily controlled because it scales linearly with applied voltage.

The end result would look like the illustrations in Fig. 7.1. But wait, it gets even better! Not only is Al_2O_3 an excellent insulator and an excellent dielectric, it is also an excellent tunnel barrier! By gently polishing away some of the oxide layer, we can drop another metal contact in the middle of a S-N-S junction to function as a tunnel probe. The tunneling resistance of such a tunnel probe is easily controlled by varying the thickness of the Al_2O_3 barrier.

This method should protect the InAs core and retain its innate mean free path, which is hopefully longer than typical measurements of 50 to 100 nm. The devices illustrated in Fig. 7.1 are thus ballistic within the InAs junction. Using the device in Fig. 7.1(a), one could measure quantized conduction steps in the normal state (by applying a magnetic field larger than the critical field), and correlate them to quantized

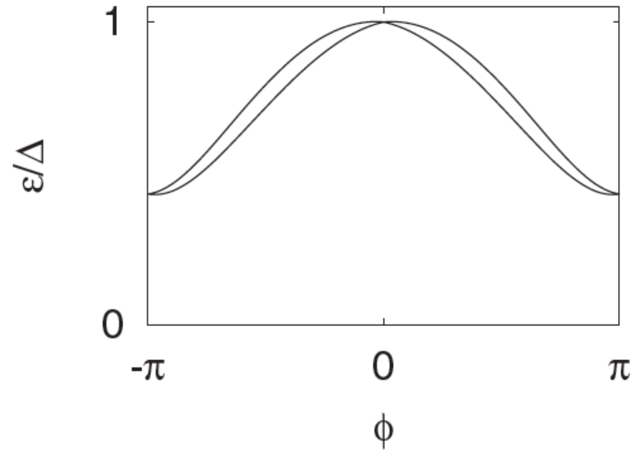

Figure 7.2: Figure taken from Ref. [119]. The degenerate ABS levels are predicted to split at finite phase difference across a ballistic Josephson junction with spin-orbit coupling. Here, ε is the energy of the ABS, Δ is the pair potential of the superconductor, and ϕ is the superconducting phase difference across the Josephson junction.

critical current steps in the superconducting state as the gate voltage is varied. Using the tunnel probe, one could also measure tunneling resonances associated with each ABS as the number of transverse modes in the one-dimensional nanowire is increased. Since the Al shell can be made arbitrarily thin, one could apply a magnetic field along the length of the nanowire and watch the ABSs spin-split.

Another option is to make a device illustrated in Fig. 7.1(b). We short out both ends of the Josephson junction with a superconducting loop. While supercurrent transport measurement is no longer possible, this configuration gives us controllability over the superconducting phase difference. Using the tunneling probe, one could still measure the tunneling resonances of ballistic ABSs. At finite superconducting phase across the Josephson junction, one could observe the splitting of the degenerate ABSs due to spin-orbit coupling [119]. This experimental signal is illustrated in the graph taken from Ref. [119] (Fig. 7.2).

In short, selective anodization of Al gives the experimentalist gate-tunability in the core, passivation of the core, and tunneling spectroscopy capabilities without ever exposing the InAs core to process chemicals.

7.2 Improved N-QPC-S devices

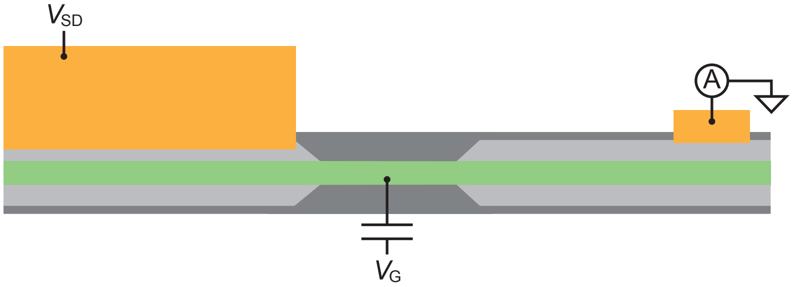

Figure 7.3: Largely similar to the device in Fig. 7.1(a), except that the tunnel probe is not necessary and one of the S electrodes is turned into N by evaporating a thick layer or normal metal. Inverse proximity effect should weaken the Al shell and remove its superconductivity.

One could potentially improve the N-QPC-S device discussed in Chapter 5. Using the device in Fig. 7.1(a) as a base template, we can do without the middle tunnel probe and evaporate a thick stack of normal metal on one of the contacts to produce a final device shown in Fig. 7.3. The idea is to 'inverse' proximitize one end of the Al shell with a large piece of normal metal so that it loses its superconducting properties (as long as the Al shell is reasonably thin). Assuming that the anodization protects the InAs core and creates a ballistic junction, we now have a N-QPC-S junction to execute the proposal by Wimmer *et al* in Ref. [120].

7.3 Direct tunneling spectroscopy of Majorana bound states

Another proposal we've been toying with for some time is more of a hail Mary approach to the detection of Majorana bound states. Armed with anodization techniques and new epitaxial core-shell InAs-Al nanowires, this proposal becomes seemingly feasible, though the existence of Majorana bound states in these systems is anyone's guess.

We begin with a lopsided epitaxial full-shell nanowire, where the Al shell is thicker on a few facets of the hexagonal core. This should be easily achieved by adapting existing growth techniques. The nanowires can then be anodized such that the thinner parts of the Al shell turn entirely into Al_2O_3, while some Al is left in the thicker parts of the shell. The end result should be an epitaxial half-shell nanowire with some of the InAs facets passivated by Al_2O_3 and others proximitized by Al.

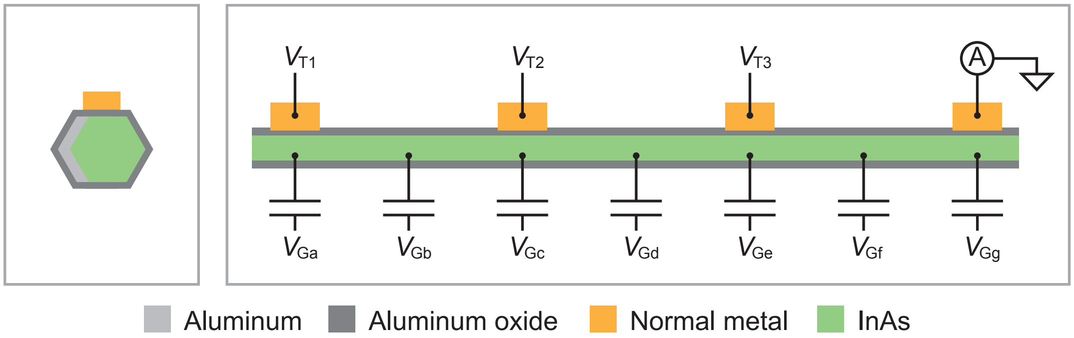

Figure 7.4: (Left panel) Cross-sectional schematic of the half-shell wire (normal to wire axis). (Right panel) Proposed epitaxial half-shell tunneling spectroscopy device. Multiple normal metal tunnel probes are deposited along the length of the wire after sufficient thinning of the Al_2O_3 shell to produce local tunnel barriers. Gate control over the nanowire can be achieved via multiple bottom or sidegates.

Once again, we can selectively thin parts of the Al_2O_3 shell and drop normal metal electrodes to act as tunnel probes. Multiple probes can be laid down along the length of the wire to measure the local density of states, as illustrated in Fig. 7.4. Any of the probes can be activated with at least one other acting as a drain electrode. In addition, multiple gate electrodes can be fabricated close to the nanowire to provide gate control over the local carrier density. If Majorana bound states do exist in these systems, they should show up as sub-gap resonances. Therefore it is of no concern that the tunnel probes will also probe the density of states of the Al half-shell.

7.4 Little-Parks experiment and the proximity effect

The Little-Parks experiment demonstrated that the critical temperature of a thin superconducting cylinder is reduced when the superfluid velocity of Cooper pairs is increased by threading the cylinder with a magnetic field [121,122]. Because the transition of resistance as a function of temperature has a finite width near T_c, resistance of the cylinder was used as a measure of the reduction in critical temperature. As a result, the resistance of the cylindrical superconductor oscillates with a period of $\Phi_0 = h/2e$ and peaks at $\Phi_0/2 \mod (\Phi_0)$.

In the case of epitaxial full-shell InAs nanowires, one could ask the question: what happens to proximity effect in the InAs core when magnetic flux is threaded through the superconducting shell? Using the device schematic in Fig. 7.1(a) as a base template, we could add additional tunnel probes to the Al shell. We can then measure the resistance of the device, the tunneling spectrum of the shell, and the tunneling spectrum of the InAs core as a function of magnetic flux through the quasi-cylindrical superconducting shell. This would be a nice textbook experiment.

7.5 Class D symmetry in InAs nanowires

While we're on the topic of phase-controlled experiments, we can also investigate the mesoscopic symmetry classes of proximitized InAs nanowires. The device in Fig. 7.1(b) could be used to execute proposals by Altland and Zirnbauer in Refs. [123, 124], although one would have to intentionally trash the InAs junction or make it longer so that transport through the nanowire is in the diffusive regime (assuming that the wires are ballistic in the first place).

The proposals also require half a flux quanta to be threaded through the superconducting loop in order to suppress the induced minigap while retaining the electron-hole symmetry of a superconductor. In principle, the original phase-controlled devices described in Chapters 2 and 3 could have been used for this experiment, but we did not have access to a vector magnet and the critical field (perpendicular to substrate) of the device was too low to produce any significant Zeeman energy. With the new epitaxial full-shell wires, the thin Al shells have exhibited parallel critical fields of up to 2 T [35]. A vector magnet can thread magnetic flux through the evaporated superconducting loop while a parallel magnetic field is applied to drive the symmetry class of the InAs nanowire from DIII to D.

However, if this magnetic field direction were to be chosen for inducing Zeeman physics, one might have to modify the device in Fig. 7.1(b) by using an epitaxial half-shell nanowire instead. An epitaxial full-shell device would trap magnetic flux within the cylindrical Al shell and turn device into an unintentional Little-Parks experiment.

It might be possible to use the device illustrated in Fig. 7.1(a) to achieve similar results by trapping half a flux quanta in the cylindrical Al shell. However, doing so might not be physically relevant since the effect of magnetic flux through the superconducting cylinder is to lower its critical temperature and drive the shell normal. More thought would be needed to verify the feasibility of this particular variation of the Altland-Zirnbauer experiment.

Appendix A

Device Fabrication

Nanofabrication is perhaps one of the more underrated skills an experimental condensed matter physicist can possess. The truth of the matter is, the better you are at fab, the easier time you'll have. At the bottom of it, it's really about a person's ability to follow instructions, then execute them consistently every single time. It's also about valuing efficacy. If a previous graduate student developed a reliable recipe, don't attempt to reinvent the wheel, otherwise you'll spend months playing around with an impossible number of fabrication variables. Finally, it's also about having a healthy dose of dexterity with your digits. In fact, I'd suggest taking on baking and assembling plastic miniatures as hobbies!

A.1 Making Pre-Fabricated Blanks

Wafer choice

I've used degenerately doped Si wafers with a 100 nm thermal oxide for most of the nanowire experiments. These wafers, purchased from University Wafers, have the following specifications:

Size: 4"

Crystal axis: [100]

Dopants: Degenerately doped, P-type, Boron

Resistivity: 0.001 - 0.005 Ωcm

Thickness: 500 μm

Thermal Oxide: 100 nm

The thin thermal oxide gives me good capacitive coupling to the nanowires, and between the backgate and the device, I've applied a maximum potential difference of about 43 V without breaking down the oxide. However, these 100 nm thermal oxides can leak quite easily, either from intrinsic defects in the substrate, scratches to the oxide during fabrication, or punctures during wire-bonding. Future fabricators of nanowire devices might want to consider degenerately doped Si substrates with thicker thermal oxides, like 200 or 300 nm.

Cleaving the wafer

The idea is to make a lot of pre-fabricated blanks in one go. The photomasks can make a 6 by 12 grid of chips, and each chip is a 5 mm by 5 mm square. So do the math and cleave a suitably large piece of Si wafer. For large pieces of Si, I wing it and leave them by hand. Take note of the flat of the wafer, and decide on a cleave direction. Make a small notch (about 2 mm long and parallel to your cleave direction) on the edge of the wafer. Rest the wafer on a glass slide, keeping the edge of the glass slide parallel to your cleave direction and directly below the notch. Using the edge of the glass slide as a fulcrum, press down on both ends of the wafer with soft-tipped tweezers until the wafer snaps (this should require very minimal force). If done correctly, the wafer should cleave straight and true in a most satisfactory manner.

The only concern here is the accidental scratching of the thermal oxide, especially after cleaving because the surface is covered with Si dust. Always keep the wafer face up (thermal oxide up). Do not cover it with cleanroom wipes. The only times you touch the surface of the wafer are when you scribe it, cleave it, and grab it by its edge with tweezers.

Cleaning the wafer - Piranha etch

I clean all of my fresh-out-of-the-box Si wafers (or pieces of it) with Piranha etch. It aggressively removes organic residues on the wafer and makes the surface of the substrate hydrophilic. It's a simple mixture of:

3 parts concentrated sulfuric acid

1 part 30% hydrogen peroxide solution

The reaction between the two ingredients is highly exothermic, so give it a couple of minutes to cool before immersing your Si substrate. I let the Si substrate soak for about 10 to 15 minutes, then dunk it successively in 2 to 3 beakers of deionized (DI) water. Blow dry with a nitrogen gun. **Remember to dispose the Piranha etch in a ventilated waste basket after it has cooled sufficiently!**

Making meanders and bond pads

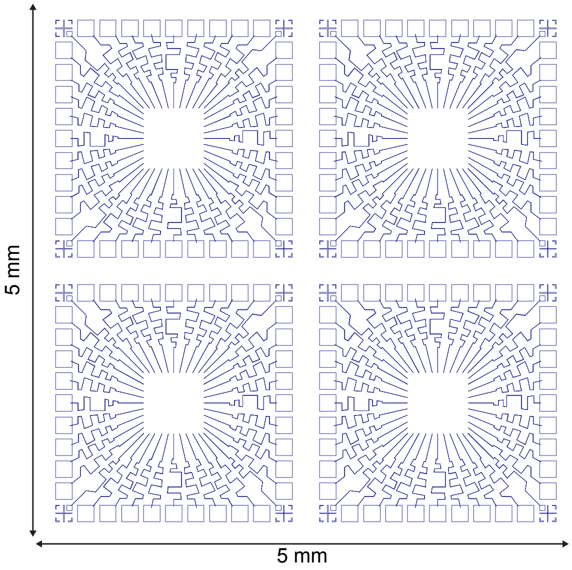

Figure A.1: Exposure pattern of one cell (or chip) of the "Meander" photomask.

The meanders and bond pads are defined with photolithography. It is a two-step process, involving two photomasks labelled "Meander" and "Bondpad" (Figs. A.1 and A.2). The meanders act as on-chip resistors. All the meanders are 1.2 mm long, and by controlling the thickness of the evaporated metals one can control the overall resistance of the lines. For both photolithography steps, I use photoresist Shipley 1813:

Spin speed: 5000 rpm

Spin acceleration: 5000 rpm/s

Spin duration: 45 s

Bake conditions: 115 degrees C for 2 min

Using a mask aligner, expose the pattern on the “Meander” photomask. I’ve only used the mask aligner in the Harvard soft matter room (4 s exposure), so I cannot say what the appropriate exposure time would be for fabbers at QDev.

After exposure, develop the photoresist with CD-26. Prepare two beakers of CD-26 and a beaker of DI water. Dunk the sample in the first beaker of CD-26 for 20 s, then immediately transfer the sample to the second beaker of CD-26 for another 25 s of development. Finally, rinse the sample in the beaker of DI water for about 15 to 30 s and blow dry with nitrogen.

Evaporate a suitable bi-metal layer onto the substrate. A typical choice would be a Cr sticking layer followed by a capping layer of Au. The total thickness of the evaporated film should be around 20 nm. The actual mix of Cr followed by Au should be determined by the desired resistance of the meanders.

Finally, lift-off the evaporated film in acetone. To speed up the lift-off process, one can elevate the temperature of the acetone in a hot water bath, or sonicate the sample in acetone.

Bond pads are fabricated next. Repeat the process of resist spinning, UV exposure, metals evaporation, and finally lift-off. This time, use the “Bondpad” photomask. Align the mask such that the corner bond pads line up with the crosses of the first layer. Evaporate a bi-metal stack of either Cr/Au or Ti/Au (5/100 nm). Thick bond pads can survive repeated bondings better than thin ones. Note that while the “Meander” photomask is 4-fold symmetric, the “Bondpad” photomask has a specific

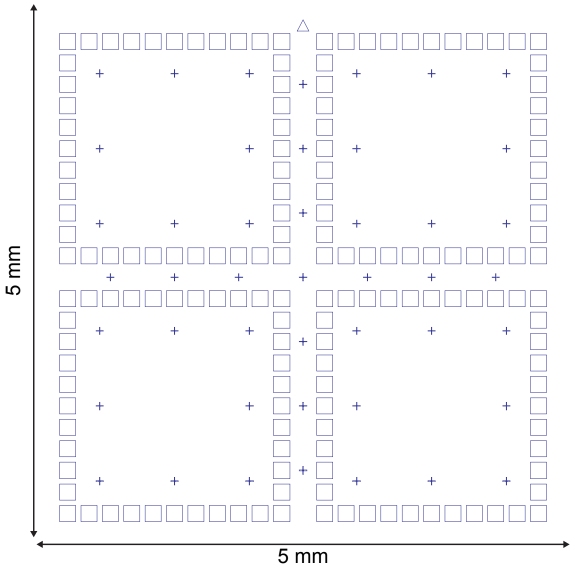

Figure A.2: Exposure pattern of one cell (or chip) of the “Bondpad” photomask. Alignment marks (crosses) are dispersed throughout the cell. The triangle at the top of the chip defines the upright position.

orientation indicated by the triangle at the very top of the pattern (Fig. A.2).

Making electron-beam defined alignment marks

The alignment marks defined with photolithography in the previous steps are not sharp enough to achieve 10 nm alignment accuracy. In this step, finer alignment marks are patterned throughout the chip with electron-beam lithography (EBL). Fig. A.3 shows EBL defined alignment marks (red) in a photolithographically defined quadrant of a chip (black). The main cluster of alignment marks are confined within a 600 μm by 600 μm square in the middle of each chip quadrant. These marks are used primarily for optical and SEM location of individual nanowires. There are eight variety of marks, and they are permutated in a 50 μm by 50 μm grid such that the combination of four closest alignment marks is never repeated within the same

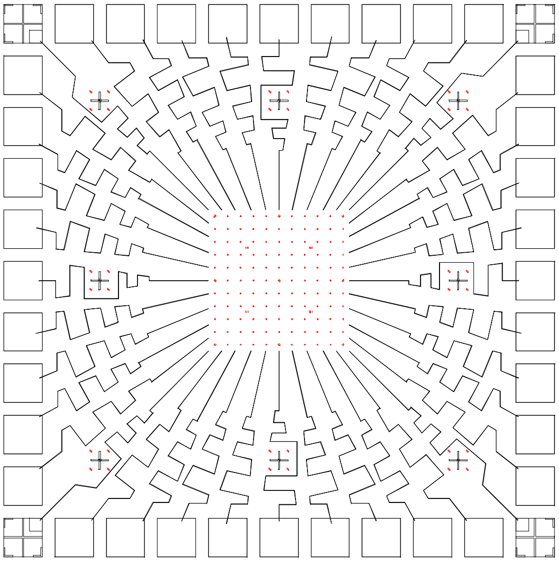

Figure A.3: Template of one chip quadrant. Patterns in black are defined by photolithography, while patterns in red are EBL defined alignment marks.

quadrant. Fig. A.4 shows a sample of these alignment marks.

EBL alignment marks are also patterned around the photolithographically defined crosses (Fig. A.3). These marks are used to align CAD patterns against the physical chip in EBL systems. To create these marks, I coat the Si substrate with a bi-layer electron-beam resist stack:

1. Bottom layer: 6% Methyl methacrylate/methacrylic acid in ethyl lactate copolymer (MMA/MAA EL6)
2. Top layer: 4% Poly(methyl methacrylate) in anisole (PMMA A4)

Both resist layers use the following spin recipe:

Spin speed: 4000 rpm

Spin acceleration: 1000 rpm/s

Spin duration: 45 s

Bake conditions: 180 degrees C for 2 min

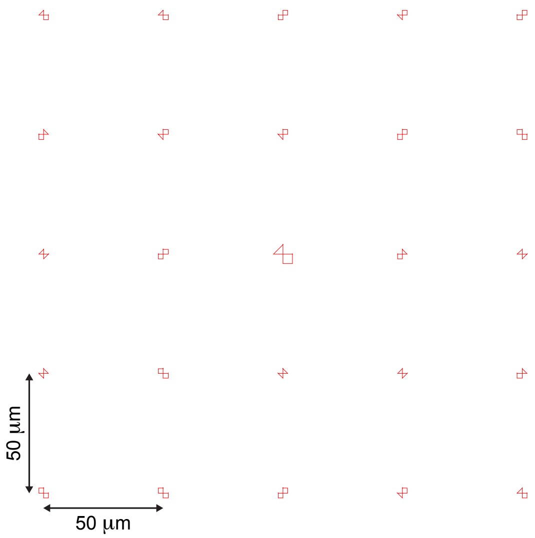

Figure A.4: EBL defined alignment marks in a 50 μm by 50 μm grid. Nanowires are located relative to these alignment marks by using optical microscopes or SEMs. The permutation of different alignment marks ensures that images of nanowires are not incorrectly overlaid on the CAD file during device design.

The Si substrate is now ready for patterning in the Elionix EBL system. Unlike the photomasks, which repeat the same pattern for 6 by 12 chips, the DesignCAD file for these alignment marks cover only one chip. It is therefore necessary to condition Elionix to repeat the pattern in a grid large enough to cover your Si substrate. Remember once again that the chips are spaced in a 5 mm by 5 mm grid. The beam conditions are:

Chip size: 600 μm by 600 μm

Number of dots: 60,000 by 60,000

Aperture: 4 (largest)

Current: 4 nA

Dose: 1200 μC/cm^2

There are a couple of issues to take note of. First, the write will span several centimeters. It is probably a good idea to rely on the laser height sensor while Elionix patterns your substrate. Second, when using the "Matrix" functions in the Elionix software to divide a write pattern into multiple "chips", select the origin of the first "chip" with care, such that the main cluster of alignment marks fall within a single "chip". This ensures that the main cluster of alignment marks is immune to Elionix stitching errors. Last of all, these EBL alignment marks have to be consistent with the photolithography pattern. Field correction in Elionix has to be engaged, and you can use any of the photolithographically defined crosses as alignment marks.

Next, Develop the exposed bi-layer resist stack with:

Developer: Methyl isobutyl ketone : Isopropyl alcohol (MIBK : IPA) 1 : 3

Time: 90 s

Temperature: Room temperature

Rinse: 15 s IPA

then dry with nitrogen. Evaporate a bi-metal stack of Ti/Au (5/15 nm), then lift-off in acetone. Once again the lift-off process can be expedited with elevated temperatures or with sonication.

Cleaving the Si substrate into individual chips

The Si substrate is now ready to be divided into individual 5 mm by 5 mm chips. A dicing saw or a scriber/cleaver can be used. Small pieces of Si can be a hassle to scribe and cleave if the scriber/cleaver is not in excellent shape. The general rule of thumb is more force and scribe the same spot multiple times to make cleaving easier. There's really no fixed recipe for this, as I've encountered diamond scribing tips in various states of disrepair. Take a junk piece of Si substrate and practice scribing/cleaving with it. Use it to calibrate the amount of force necessary and the number of scribes needed. The rest should then be straightforward.

Congratulations! Now you have a gel-box full of pre-fabricated blanks!

A.2 Depositing nanowires onto pre-fabricated blanks

There are two ways to transfer nanowires from their growth substrate to target substrates - dry and wet. I cannot determine which method is better. Dry deposition is more localized, because one can target where one dabs. However, it appears to break long nanowires into many small pieces. Wet deposition spreads nanowires all over the place, but seems to leave the nanowires relatively intact. However, it has been suggested that sonication induces small cracks in the crystalline Al shell for core-shell nanowires. I do not have enough evidence from my personal experience to conclude one way or another.

Dry transfer technique

The idea is to take a very small piece of cleanroom wipe, swipe a small area of the growth substrate, then dab the cleanroom wipe on your target chip. In other words, knock over thousands of nanowires with a cleanroom wipe, get them stuck in the fibers of the cleanroom wipe, then release them over your target chip.

First, the recipient chip should be cleaned with acetone then IPA (soak the chips in each solution for a few minutes).

Next, take a cleanroom wipe, and cut an acute isoceles triangle about 15 to 20 mm in height and 6 mm across at the base. Note that the length of the triangle should be parallel to the grain of the cleanroom wipe. This ensures that the apex of the triangle does not fray as easily (see Fig. A.5).

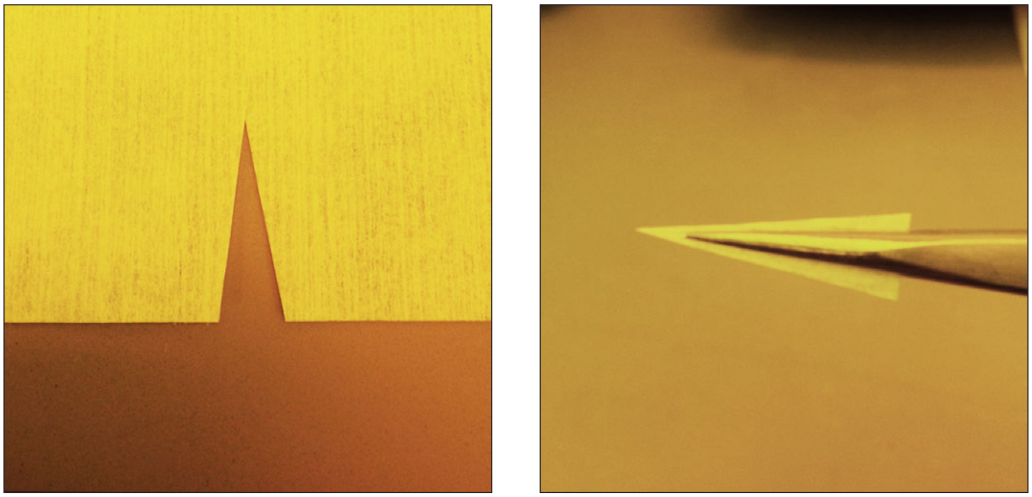

Figure A.5: (Left panel) Cut at shallow angles along the grain of the cleanroom wipe to make an acute isosceles triangle. Notice how the grain of the cleanroom wipe runs vertically in this photo. (Right panel) With a pair of sharp tweezers, hold the piece of cleanroom wipe such that the tip of the cleanroom wipe is about 1 mm away from the tip of the tweezers.

With a pair of sharp tweezers, hold the triangle such that the tip of the cleanroom wipe is about 1 mm away from the tip of the tweezers (demonstrated in Fig. A.5). Using the extended part of the triangle like a brush, swipe a small area (0.5 mm by 0.5 mm) of the growth substrate. Under good lighting conditions, the naked eye can discern areas that have been swiped and areas that still have nanowires. Now that the tip of the cleanroom wipe is full of nanowires, dab the target substrate repeatedly as if you were recreating an impressionist piece by Monet.

Repeat as many times as required to achieve the desired density of nanowires. The same cleanroom-wipe-triangle can be reused, until the tip becomes too frayed or flaccid.

Wet transfer technique

Figure A.6: Plastic vial for growth wafer sonication. The vial is just big enough to fit a piece of the growth wafer so that only a small amount of methanol is needed to submerge the substrate.

Insert a small piece of the growth substrate (it can be as small as 1 mm by 1 mm) into a plastic vial like one shown in Fig. A.6. I use plastic and not glass because plastic receptacles damp the effects of sonication. Add just enough methanol to wholly immerse the growth substrate (typically a few droplets). Sonicate the vial for 10 s. Using a micropipette, extract the suspension of nanowires, and deposit a few droplets onto the target substrate.

Now, unlike standard drying techniques with a nitrogen gun, the idea here is to let the droplet evaporate slowly on the substrate. As the droplet reduces in size, you can nudge the droplet around with a gentle flow of nitrogen. This gives a small degree of positional control over the nanowires. Finally, do not let the droplet dry completely on the target substrate. This leaves behind a lot of residue. The last straggling droplet of methanol suspension should be blown off the chip.

Once again, if necessary, repeat the process until the desired density of nanowires is achieved. The growth substrate can be left to dry and reused for subsequent depositions.

A.3 Optically locating nanowires

The InAs nanowires I've used have diameters upwards of 40 nm and lengths up to 10 μm. These are rather big objects, and are easily identifiable under a decent optical microscope.

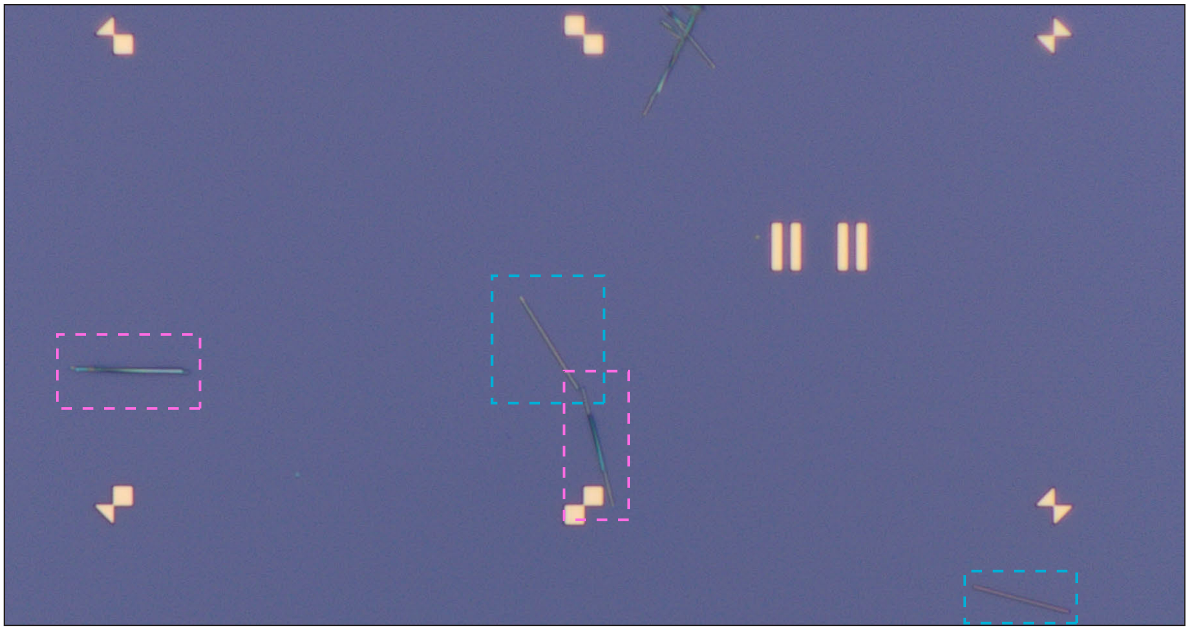

Figure A.7: Optical microscope image of InAs nanowires on a pre-fabricated substrate. Ideal and non-ideal wires are boxed in blue and pink dashed lines respectively.

Fig. A.7 is an example of a bright field image taken at 100× magnification. Some people prefer dark field images because of the higher contrast between nanowire and substrate, but personally I prefer bright field images because it gives me color information on the nanowire. Examples of nanowires that I would fabricate devices on are boxed in blue dashed lines in Fig. A.7. These are clearly single, isolated nanowires with no discoloration. Examples of nanowires that I would not use are boxed in pink dashed lines. Under careful scrutiny, these are most likely nanowires sitting on top of each other.

Optically locating the nanowires can give sub-50 nm position accuracy. When taking a picture, try to include as many alignment marks in the field of view as possible. Six well positioned images at 50× can cover the entire grid of alignment marks and still give good resolution on the nanowires.

A couple of things to take note of. First, needless to say, focus is important. It makes aligning the optical images in DesignCAD easier. Second, I try to rotate the chip and the microscope stage such that the alignment marks are parallel with the edge of the image. Spending an extra 5 minutes at the microscope will save you the trouble of rotating these images in Photoshop later. Third, nanowires, though infrequently, can shift when resist is spun onto the substrate. Therefore it is preferable to image the nanowires after coating the chip with the appropriate electron-beam resist. Finally, all lenses distort images to some extent. I try to avoid framing choice nanowires at the edge of the images (where lens distortion tends to be largest), and when scaling the images in DesignCAD, I scale the height and width of the images independently.

A.4 Electron-beam resist stacks

To keep things simple, I use the same spin recipe for every electron-beam resist layer:

Spin speed: 4000 rpm

Spin acceleration: 1000 rpm/s

Spin duration: 45 s

Bake conditions: 180 degrees C for 2 min

Copolymer-PMMA A4 bi-layer stack (good for almost everything)

This is a standard resist stack that is suitable for features as small as 40 nm with a 90 nm pitch, assuming that it is then developed at room temperature. The only choice here is the concentration of MMA/MAA in EL. In general I use EL9 (9%) because the nanowires can be thick (up to 120 nm in diameter), and EL9 lifts of very easily.

Bear in mind that the undercut with this resist stack is large. Small features with small pitch can result in areas where the PMMA A4 layer is completely suspended. This becomes a problem if one uses Ti as a sticking layer, as Ti can wet and short electrodes in close proximity. The solution in this case is to use Cr as a sticking layer, or to use the resist stack in the following section.

Double layer PMMA A4 stack

I use this resist stack for good resolution and minimal undercut (prevents Ti wetting between electrodes). The only reason for the bi-layer stack is to give it sufficient height for thick nanowires.

Single layer PMMA A6 stack

I use a single layer PMMA A6 stack for defining chemical etch windows, windows that are not meant to be filled with metals in a subsequent evaporation step. In other words, the resist is only meant to create large (micron sized) features for chemicals to come through. It is a single layer stack to minimize undercut and prevent chemicals from running laterally.

Tri-layer PMMA C6-C6-A4 stack

This is the mother of all resist stacks, as it is ridiculously tall, and therefore, ridiculously easy to lift-off. This tri-layer stack is meant for EBL patterning of hafnium oxide atomic layer deposition (ALD). 'C' in C6 refers to chlorobenzene (as opposed to anisole). Since chlorobenzene is frowned upon, future users can replace PMMA C6 with an appropriately thick replacement (like A6).

A.5 Electron-beam lithography

Any feature larger than 100 nm is extremely robust to dose fluctuations. When using the PMMA-anisole family of resists, EBL dosage ranges from 1000 to 1500 μC/cm^2.

The parameters I use are:

Chip size: 600 μm by 600 μm

Number of dots: 60,000 by 60,000

Aperture: 1 (smallest)

Current: 500 pA

It is not a coincidence that the ends of the meanders and the main cluster of alignment marks are within a 600 μm by 600 μm window. The pre-fabricated blanks are designed such that every EBL step needs only one Elionix 'chip' for each quadrant. This removes the hassle of having to use the 'matrix chip' function and makes the fabrication process immune to stitching errors.

I use 500 pA for pretty much all my EBL processes (except writing alignment marks and enormous features like bond pads). Given the dose I use and the improved beam blanking time on the new generation of Elionix systems, the writing current could in principle be much higher. However, large currents charge up my alignment marks rapidly (especially on an insulating substrate) and makes alignment a little more difficult. 500 pA seems like a fine compromise between large current size and alignment mark visibility during field correction.

As I've mentioned, EBL with PMMA is a relatively robust process and for 100 nm scale feature sizes, it is not too sensitive to dosage. As a rule of thumb, I use 1200 μC/cm^2 for features between 100 nm and 1 μm, 1500 μC/cm^2 for features in the micron range, and 1000 μC/cm^2 for features around 50 nm. Bear in mind that 1000 μC/cm^2 is borderline underdosing. If your device features are living in this region, it is best to do a dose test.

A.6 Developing electron-beam resist

Developer: MIBK : IPA 1 : 3

Duration: 90 s

Temperature: Room temperature

Finishing: Quench reaction and rinse in IPA, blow dry with nitrogen

It is possible to achieve consistent finer features (20 to 40 nm) by developing the resist at 0 degrees C (cold developement). The developer can be chilled in an ice bath or a peltier cooler for about 15 minutes. The only other difference is that the EBL dosage required would be about 2 to 3 times the normal value.

A.7 UV ozone clean and plasma ashing

Both processes are similar, and performing either one will do. It all depends on what is available in your cleanroom.

UV ozone clean and plasma ashing achieves two purposes. The first, is to burn off a thin layer of organic polymer. The second, is to increase the hydrophilicity of the substrate. Both purposes are crucial if the next step involves a chemical etch. It is therefore important that you subject your sample to either process before any chemical etchants.

If the next step involves ion milling, then these processes are most likely unnecessary, since the Ar ions will strip the resist as well.

For UV ozone, using the equipment in the Harvard cleanroom, I subject my sample to a 60 s clean at room temperature, and at a gas flow rate of 1.

For plasma ashing, using the asher in the QDev cleanroom, I subject my sample to a 30 s clean.

A.8 Making ohmic contacts to InAs

Stripping native InAs oxide can be achieved chemically or physically. The advantage of a chemical etchant like ammonium polysulfide is that the sulfur content in the etchant passivates the surface of the InAs nanowire, allowing the device to age less quickly [33]. The advantage of Ar ion milling is that the Kaufman ion source is attached to the same vacuum chamber as the electron-beam evaporator, allowing one to mill and evaporate without exposing the nanowire to ambient conditions.

Regardless of the method used, either process in this section should give you a near 100% yield.

Chemical etching of native oxide

This recipe originates from Ref. [33]. I pre-mix and store a half-liter batch of ammonium polysulfide etchant. This generally lasts for about 2 months. To make a half liter batch, I use:

1. 450 ml of DI water
2. 50 ml of stock ammonium sulfide, 20-24% aqueous solution from VWR International
3. 2.4 g of elemental sulfur (powder form)

Needless to say, the ingredients are extremely pungent. Processes that involve ammonium sulfide and ammonium polysulfide should be performed in a well ventilated fume hood.

In a glass beaker, mix the sulfur powder with the stock ammonium sulfide solution. The sulfur powder does not dissolve easily, so stir the solution at elevated temperatures (using a hot plate or a hot water bath, but never at temperatures above 40 degrees C!). As the sulfur dissolves, the solution turns from a pale yellow to a dark yellow/brown liquid. After the sulfur powder has been completely dissolved, dilute the solution with DI water. Store the final solution in a suitable bottle. I've used standard high-density polyethylene (HDPE) bottles, but it is probably preferable to store it in an amber glass bottle, since the chemical is sensitive to harsh lighting.

To etch InAs nanowires, warm a small beaker of the mixed solution to 40 degrees C in a water bath. While it is warming, cover the beaker with a lid to minimize solvent evaporation. Before you begin the actual etch, remember to UV ozone clean or plasma ash the sample! Immerse your sample in the solution for 17 minutes, making sure that the beaker stays covered and no bubbles form on the surface of your chip. Finally, quench the reaction in DI water, rinse and dry carefully.

Now that you've removed the native oxide on your InAs nanowire, start running towards the evaporator and load the sample before it starts oxidizing again!

Ar ion milling of native oxide

Making ohmic contacts with Ar ion milling in the AJA systems is a very straightforward process. The settings for the Kaufman ion source are shown in Fig. A.8. The

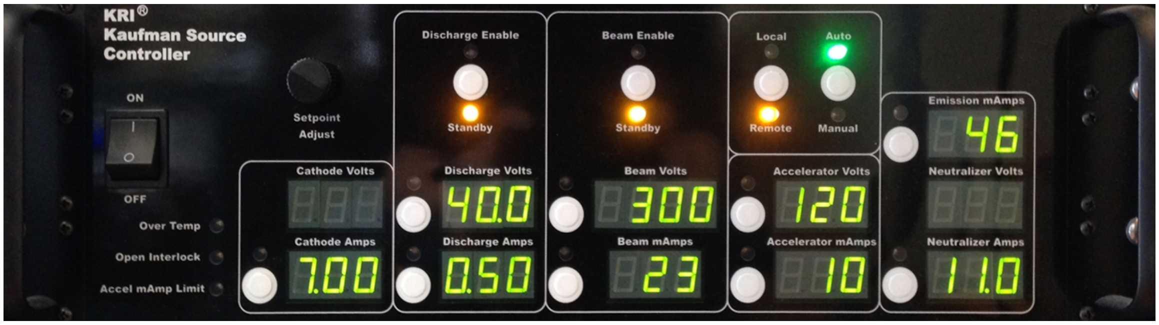

Cathode Amps 7.00

Discharge Volts 40.0

Discharge Amps 0.50

Beam Volts 300

Beam mAmps 23

Accelerator Volts 120

Accelerator mAmps 10

Emission mAmps 46

Neutralizer Amps 11.0

Figure A.8: Settings for the Kaufman ion source.

rest of the parameters are:

Ar flow rate: 15 sccm

Pressure: 9.8E-4 Torr

Etch time: 1 min 15 s for AJA 1, 1 min 53 s for AJA 2

Toggle the VAT gate-valve controller to 500 (0 being fully closed and 1000 being fully opened). That should give a chamber pressure of around 9.8E-4 Torr. Note that the milling time required in AJA 2 is about 50% longer than what is required in AJA 1. There is a 7 s delay between turning on the ion source and having an actual emission current. The “Plasma” circle on the AJA control PC turns pink when this happens. Start the timer only when the circle turns pink.

One more thing to take note of. Since Ar ion milling usually precedes metals deposition with the electron-beam evaporator, it is crucial to let the pressure drop back to standard pressures (below 1E-7 Torr) before starting your evaporation.

A.9 Making tunnel contacts

Tunnel contacts for devices in Chapters 2, 3 and Ref. [59] are essentially very bad ohmic contacts. A part of the native InAs oxide is intentionally left behind with an incomplete etch. This remnant oxide acts as a tunnel barrier. Because it is an incomplete chemical etch, the final tunneling resistance at room temperature can be anywhere between 25 kΩ to 10 MΩ.

NOTE: Because the aim is to perform an incomplete etch, contrary to regular practice, I do not UV Ozone clean or plasma ash the developed sample. I also do not run to the evaporator to load the sample in a hurry. Instead, I would saunter towards the evaporator at a leisurely pace after the sample has been etched.

To etch, I use a 7 : 1 buffered oxide etch (BOE). Etch the sample at room temperature for 7 s, then quench and rinse the in DI water. Blow dry with nitrogen.

Remember to use acid-resistant tweezers!

An alternative to BOE is to use the same ammonium polysulfide etch recipe for ohmic contacts. However, since we desire an incomplete etch, I etch for 12 min instead of 17 min. This gives similar tunnel contacts as BOE would.

A.10 Chemical etching of Al shell

Credit goes to Nino Leander Bartolo Ziino for developing this recipe. Aluminum Etchant Type D manufactured by Transene Company Inc. is the etchant of choice. Warm it up to 55 degrees C in a closed beaker with a hot water bath. The etch is only 10 s, so get the timing right! The etchant eats bare Al very rapidly. Most of the

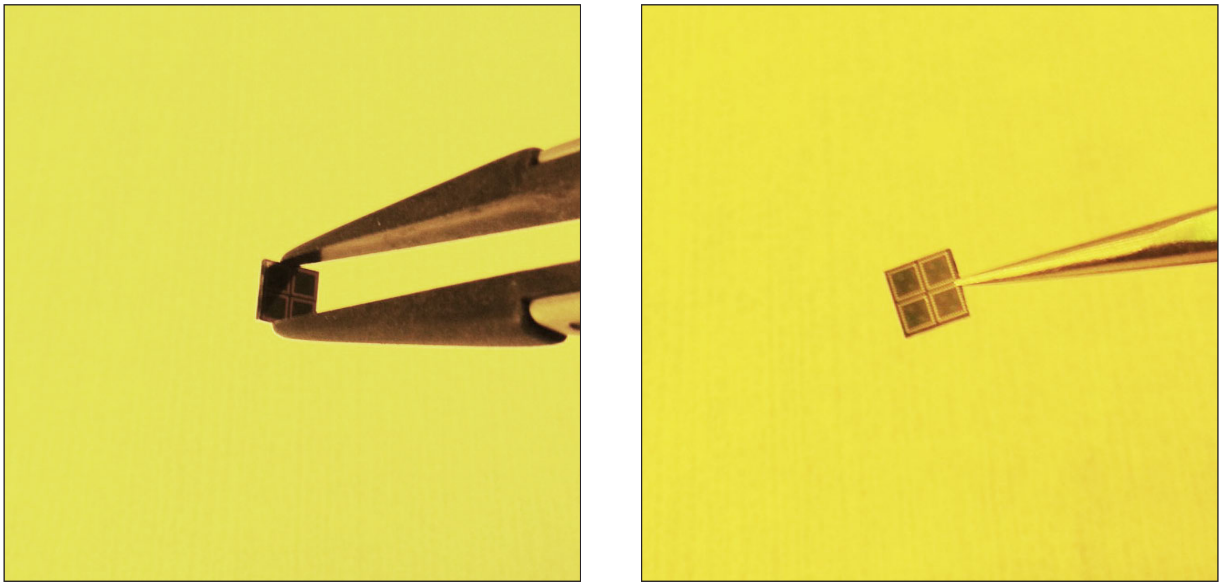

Figure A.9: (Left panel) Regular method of handling chips. Tweezers apply pressure to the sides of the chip to avoid coming into contact with the surface. However, air bubbles can be trapped between the surface and the tweezers when immersed in a viscous liquid. (Right panel) Suggested method of holding a chip when chemically processing it.

damage (etching a couple of hundreds of nm) is done within 2 s. The rest of the 10 s etch attacks the Al oxide which is a much tougher customer.

A few things to take note of. First, the way a chip is held with a pair of tweezers is crucial. Usually, I hold a chip by clamping down on its sides with a pair carbon polymer-tipped tweezers (see left panel of Fig. A.9). This way, the surface of the chip never comes into contact with the tweezers and it cannot be scratched. However, immersing a chip into viscous liquids this way can create a pocket of air between the chip surface and the pair of tweezers. In a 10 s etch, you might as well not be etching at all!

To counter this, I switch to a less favored way of holding the chip – clamping down on the front and back of the chip (see Fig. A.9). To reduce the extent of any damage to the surface of the chip, I hold the chip in between quadrants and over as small of an area as possible.

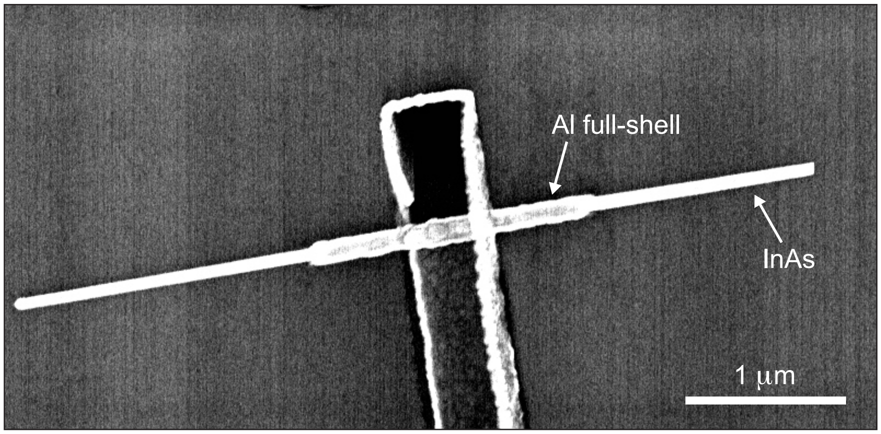

Figure A.10: SEM micrograph of an epitaxial full-shell nanowire, post etch. The nanowire is held down by an evaporated Al contact.

After 10 s, I terminate and flush the etch in two beakers of DI water. Give the chip an aggressive swirl in the first beaker of DI water, then dump it in the second beaker of water for about 30 s. The etchant works its way along the nanowire so it is paramount to thoroughly rinse the chip.

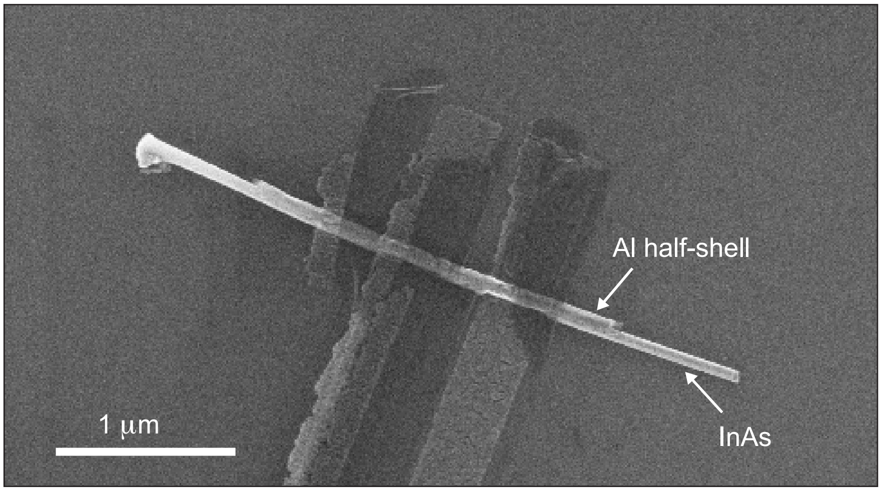

Figure A.11: SEM micrograph of an epitaxial half-shell nanowire, post etch. The nanowire is held down by two evaporated Al contacts. Debris on the chip are most likely due to the redeposition of SiO_2 during ion milling.

It is possible to see the difference between etched and non-etched parts of the nanowire under an optical microscope. Without optical filters, the nanowires should look kind of apple-green in color and rather fat. After chemical treatment, the etched parts of the nanowire should look thinner and black, like burnt matchsticks.

However, the etchant runs aggressively along the nanowire, so lateral etching can be big, up to 200 nm on either side of the etch window. This is with a single layer PMMA, so imagine the extent of unintentional etching one can have if a bilayer resist stack with strong undercut was used instead! Unfortunately it is impossible to determine with any accuracy the extent of this lateral etch (it varies every time). So we image the post-etch nanowires with a low power SEM to locate the termination of the Al shell. Figs. A.10 and A.11 show what a full-shell and a half-shell nanowire look like after etching.

The Al shells of these nanowires terminate rather abruptly, giving a nice edge at the end of it which can be easily identified under a SEM. This is fortuitous. Some etches can give the shell a tapered termination, which makes it very difficult to identify where the shell ends.

Since the etchant is mostly phosphoric acid, I'll say this again. **Remember to use acid-resistant tweezers!**

A.11 Making ohmic contacts to Al shell

I only make ohmic contacts to the Al shell with ion milling. Refer to sub-section A.8 for milling parameters. The only difference is in the milling time. To completely remove Al_2O_3, mill in AJA 1 for 3 minutes, and in AJA 2 for 4.5 minutes.

Appendix B

Electrical Filtering

For my experiments, filtering and shielding in the fridge serves three primary purposes. The first is the thermalization of electrons. While the base temperature of the dilution refrigerator may be 20 mK, the electrons that are injected into the device at the end of the cold finger can be much higher in temperature. The electron temperature ultimately defines the thermal broadening of any transport signature. While my experiments are not tremendously sensitive to electron temperatures like fractional quantum Hall effect experiments do, it is still nice to have well thermalized electrons.

The second purpose is to eliminate noise from the electronics and the environment. The third and final purpose is more specific to superconductivity – the minimization of quasiparticle poisoning. High frequency radiation more energetic than the superconducting gap can break cooper pairs and introduce unwanted amounts of quasiparticles in the devices. Recent results suggest that the effective quasiparticle poisoning temperature of our setup is about 200 mK, which is not exactly stellar.

More care could be taken to shield the sample space [125].

B.1 Overall layout

I've set up two different fridges and measured in three, so the filter setup has been changed multiple times. However, the components in each fridge are similar, and the general principle is identical. This section describes the general layout of Marcus 3, Triton 1, and Triton 3 dilution fridges.

B.1.1 Marcus 3

Marcus 3 is the third cryo-free dilution refrigerator in old Marcus lab (we're not tremendously creative when it comes to naming things). I very much prefer Marcus 3 because it was configured purely for DC measurements and it had a very nice feature – a shielded coldfinger. The coldfinger and sample puck assembly was designed by Angela Kou [126]. The detached coldfinger, shown in Fig. B.1, is machined from a single piece of copper and then gold-plated.

A bore runs along the length of the otherwise solid coldfinger. This allows any wiring threaded through the bore to be completely shielded between the mixing chamber plate and the device. We extended this column by adding a copper box to the top of the coldfinger. The copper box houses a copper powder filter and a sapphire box.

The copper powder filter serves as a block to high frequency radiation through skin-effect damping between the insulated wires and the surrounding copper powder. The sapphire box thermalizes the electrons with the mixing chamber plate through

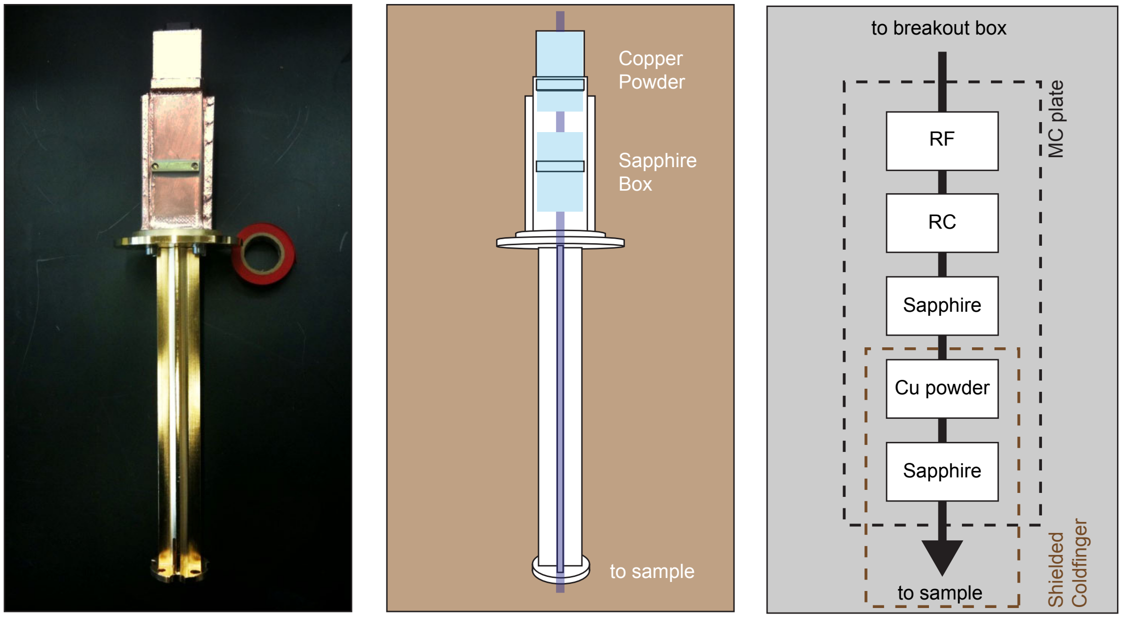

Figure B.1: Filter setup on Marcus 3. Left panel shows a picture of the shielded coldfinger arrangement. Components in the shielded coldfinger are illustrated in the center panel. Right panel shows the overall layout of the filter arrangement.

dissipative meanders fabricated on sapphire plates – an electrically insulating material known for good thermal conductivity at low temperatures [127].

The rest of the filters are mounted on the mixing chamber plate, as illustrated in the rightmost panel of Fig. B.1. The RF filter is a series of LC low-pass filters with cutoff frequencies beginning at 80 MHz. The RC filter has a single 80 MHz-cutoff LC filter and two RC low-pass filters. Finally, another sapphire box is also mounted directly to the mixing chamber plate to provide additional thermalization.

At various stages of the fridge we mount copper thermalization posts for additional thermalization. These are cylinders made out of high-conductivity copper. Looms comprising of twelve twisted pairs of constanstan wires wrap around the copper cylinder. The same type of loom connects the various stages of filtering together.

The result of the addition of the custom coldfinger and various filtering/thermalization

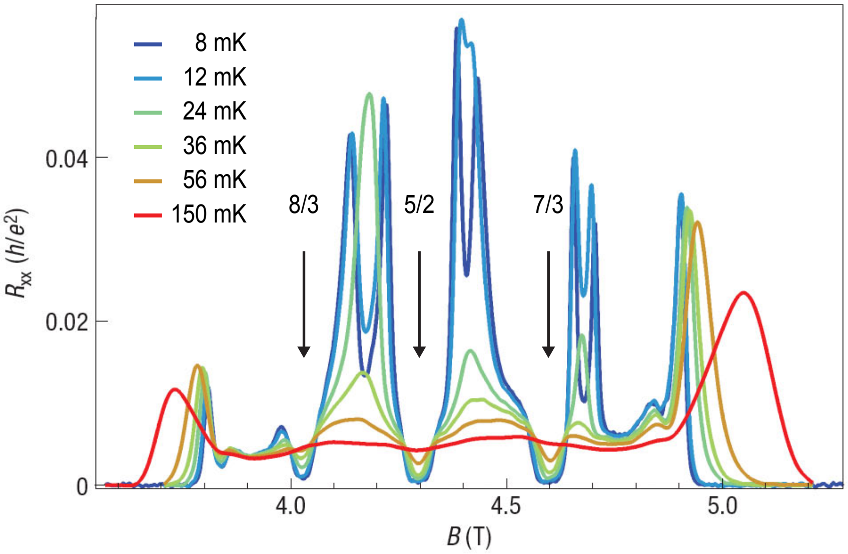

Figure B.2: Figure taken from Ref. [128]. Longitudinal resistance of a GaAs 2-DEG hall-bar in the fractional quantum hall regime is measured as a function of magnetic field at various temperatures.

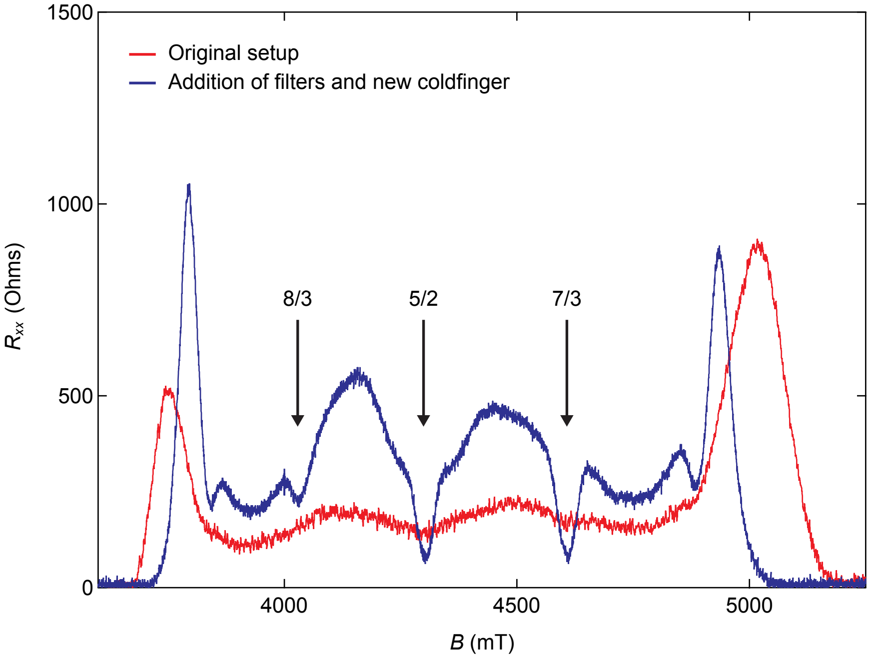

Figure B.3: Longitudinal resistance of a hall-bar made from the same GaAs wafer as the device Jeff Miller measured in Ref. [128]. The hall-bar was measured before (red) and after (blue) the installation of the custom coldfinger and filtering/thermalization modules.

modules can be seen in Fig. B.3. We measure the longitudinal resistance, R_{xx}, of a GaAs 2DEG hall bar (wafer I.D. P2-25-05, grown by L. Pfeiffer and K. West) at filling factors close to $\nu = 5/2$. Features in longitudinal resistance around $\nu = 5/2$ is very sensitive to temperature, and can be used as a metric for electron temperature. Fig. B.2, taken from Ref. [128], shows the temperature dependence of R_{xx}.

Qualitative comparison between data in Fig. B.3 and data in Fig. B.2 suggests an electron temperature in excess of 100 mK in the original configuration of the fridge. After modification, we see a sharp reduction of R_{xx} at $\nu = 5/2$. However, it does not reach 0 as it should at temperatures below 20 mK (Fig. B.2). We estimate our final electron temperature to be somewhere around 30 mK.

With extensive modifications to the coldfinger and sample holder, it is possible to reach electron temperatures of sub 20 mK in these cryo-free dilution refrigerators [126]. Fortunately, the superconductivity related experiments carried out in Marcus 3 are relatively insensitive to temperatures below 50 mK.

Electron temperature aside, I would like to note the importance of the RF filter box and the 80 MHz π^7 filter in the RC filter box. Because the initial setup of the RC filters was too aggressive, we once removed the RC filter box completely. To our dismay, the transition in the IV curve between the superconducting branch and the normal state branch of an InAs Josephson junction was smoothened out. Additionally, the superconducting branch of the IV curve had a finite gradient. The effects were somewhat offset by applying additional VLFX-80 filters to the breakout box at room temperature, or by reinstalling the RC filter with just the 80 MHz π^7 filter (without R and C components). This suggested to us that high frequency noise (above the MHz range) was making its way down onto the sample, and that a single stage of RF filtering was insufficient. The 80 MHz π^7 filter in the RC box acted as a secondary RF filter stage and was sufficient to maintain sharp transitions and a flat IV curve when the Josephson junction was superconducting.

B.1.2 Triton 1 & 3

When the lab moved from Harvard to QDev, Oxford Instruments made extensive modifications to the existing cryo-free units. Additional loom, coaxes, and a new coldinger/sample puck assembly were installed. Unfortunately, this meant that the shielded coldfinger was replaced with a coldfinger that didn't provide any shielding at all.

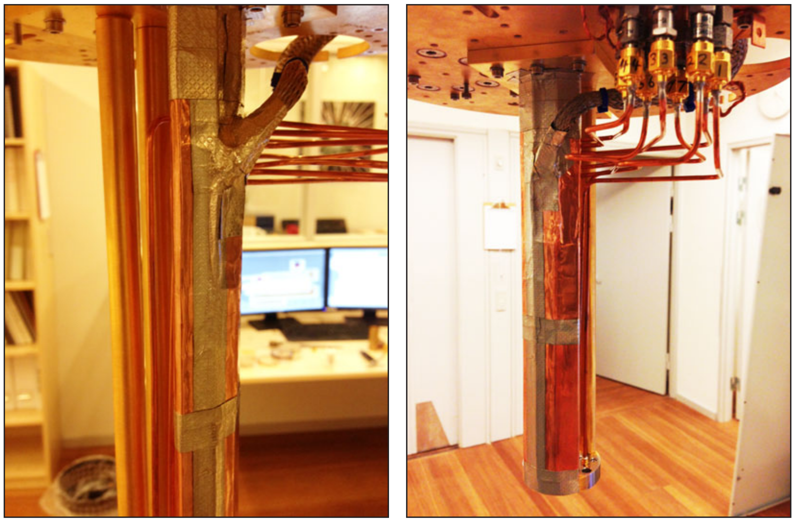

Figure B.4: New coldfinger of Triton 1, modified by wrapping sheet copper around the coldfinger struts to contain the DC looms traveling between the sample puck and the rest of the mixing chamber plate.

To counter this deficiency, I added sheet copper around the support struts of the coldfinger to make an 'encased' region through which the DC loom was threaded

(Fig. B.4). The enclosure is extended onto the mixing chamber plate by wrapping the loom in tinned copper braids. Starting from the coldfinger towards the breakout box, the loom goes through two sapphire boxes, a copper powder filter, a RC filter, a RF filter, and a couple of copper thermalization posts at higher stages of the fridge. This arrangement is largely similar to the one used in Marcus 3. Further shielding, up to the beginning of the RF filter, is achieved by folding sheet copper over connectors between the numerous filter boxes (Fig. B.5).

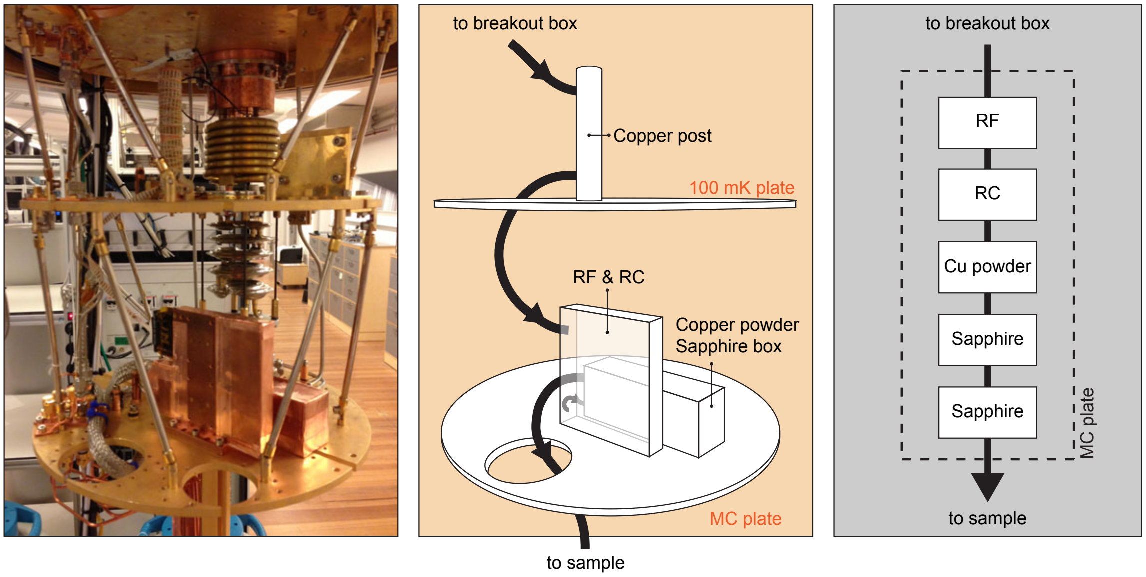

Figure B.5: (Left panel) Photo of the cold plate and mixing chamber plate of Triton 1 after installation of shielding and filtering. (Center panel) Simplified schematic of the photo to highlight the positioning of the filter and thermalization boxes. (Right panel) Layout of filters.

The additional loom that runs between the puck-end of the coldfinger and the mixing chamber plate is disconnected and shielded with tinned copper braids. Since the experiments do not require radio-frequency signals, coupling to the coaxes is terminated by removing the SMP bullets on the sample puck.

B.2 RF filters

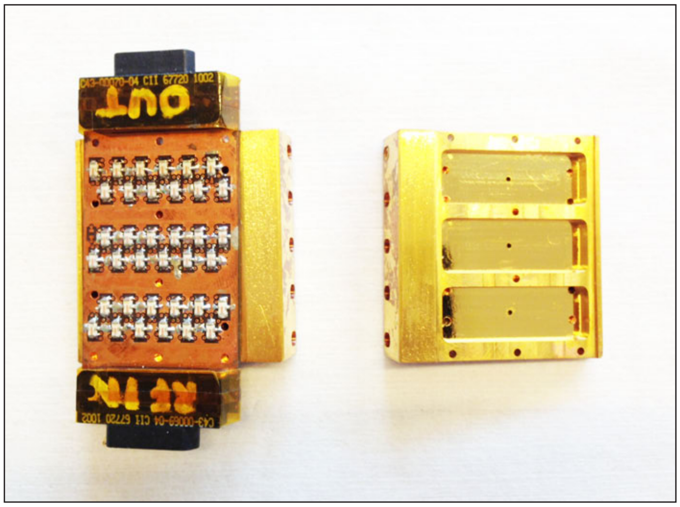

Figure B.6: Photo of disassembled RF filter. Each DC line goes through 3 stages of π^7 filters with cutoff frequencies at 80 MHz, 1.4 GHz, and 5 GHz.

The components of the RF filter are identical to the components that make up a VLFX-80 filter from Mini-Circuits®. Three Mini-Circuits® π^7 filters are mounted in series on a PC-board designed by Ferdinand Kuemmeth (Fig. B.6). These are LC low-pass filters with cutoff frequencies at 5 GHz, 1.4 GHz, and 80 MHz. The boards have 24 lines terminated with 25-pin mini D-sub connectors.

The whole assembly is then encased in two gold-plated copper covers (Fig. B.6). These covers provide electrical shielding, thermalization to the cryostat, and mounting holes. Further details on the construction of the RF filters can be found on the QDev wiki.

B.3 RC filters

Like the RF filters, the RC filters have 3 stages of filtering on 24 lines. The first component is a Mini-Circuit π^7 filter with a 80 MHz cutoff frequency. The next two stages are customizable resistor-capacitor circuits. Depending on the desired cutoff frequency, different surface-mount resistors and capacitors can be chosen.

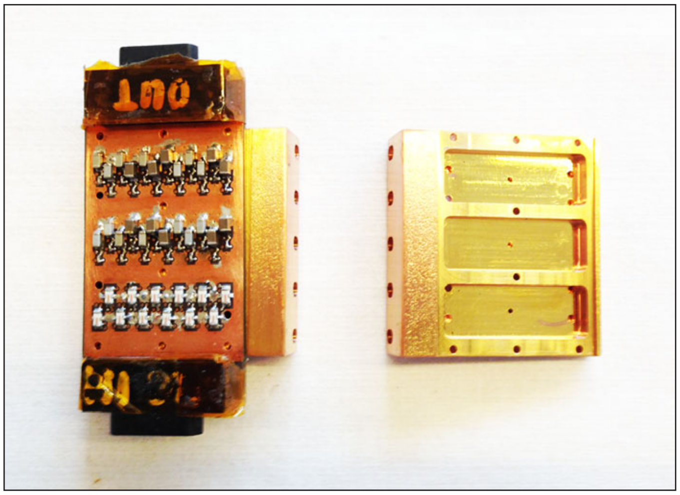

Figure B.7: Photo of disassembled RC filter. Each DC line goes through a 80 MHz π^7 filter and two stages of RC filters. R and C values are up to the discretion of the experimentalist.

The initial setup for each stage of my RC filter was a 2 kΩ resistor and a 100 nF capacitor, giving a cutoff frequency of 512 Hz. However, this setup quickly became problematic because the moment a large bias resistor (of order 1 MΩ) was added to the measurement circuit, the cutoff frequency became ridiculously low.

The RC components were then changed to 1 kΩ and 1 nF for all lines, which lifted the cutoff frequency and gave much more flexibility in measurement circuit arrangement.

B.4 Copper powder filters

The idea behind a metal powder filter, reported in Refs. [129–133], is to surround an insulated wire in close proximity with a large-surface-area conductor. To do so, we pack coiled and insulated copper wires into a copper enclosure and fill the enclosure with fine-grain copper powder. The copper powder provides a large surface area and produces significant skin-effect damping of high frequency signals in the copper wire.

However, such a filter box provides challenges to the vacuum environment of a dilution refrigerator. Fine grain copper powder in an enclosed space meant that a lot of air would be trapped. To overcome this problem, we pack the copper powder and the central wire into an epoxy 'ravioli' (or 'dumpling', if you wish). The epoxy enclosed 'ravioli' would then prevent the copper powder filter from outgassing into the vacuum chamber of the fridge.

Unfortunately, I do not have any pictures of a disassembled copper powder filter box, since the lids are epoxy-ed shut. To assemble one, we coil fine insulated copper wires with a handheld power drill. The cylindrical surface of the drill bit helps to coil the wire efficiently and with a constant diameter.

The coiled wires are then soldered on both ends to mini D-sub connectors that are already mounted on the copper powder enclosure (see QDev wiki for their CAD drawings). Next, we close the lid of the copper box on one side, and line the bottom and walls with Stycast® 2850 FT epoxy. This epoxy has the added advantage of being thermally conductive, and so helps in the thermalization of the central wires. Once the epoxy has set and dried, we fill the 'half-ravioli' with copper powder (copper, and not stainless steel, to prevent stray magnetism). To compactify the copper powder, we apply a handheld vibrator to the copper enclosure. After sufficient quantities of copper powder have been packed in, we seal the top of the copper box with more epoxy, and screw the lid on. Before the epoxy 'lid' can set, we place the copper powder filter box into a vacuum chamber and pump on it with a wet pump. This removes air pockets trapped between the copper grains and the epoxy.

B.5 Sapphire boxes

Sapphire boxes are highly crucial for electron thermalization below 1 K. The operating principle is simple: let warm electrons from the measurement circuit come into contact with a cold surface for an extended period of time. The coldest surface in the fridge would be the mixing chamber plate. However, since it is electrically conducting, it would be impossible to directly thermalize more than one measurement line. To solve this problem, we attach sapphire plates to high-conductivity copper boxes. Sapphire is an electrical insulator, and an excellent thermal conductor at low temperatures [127].

A disassembled sapphire box is shown in Fig. B.8. Two sapphire plates are mounted on opposing sides of the copper box. Each sapphire plate has 12 meanders to give a total of 24 DC measurement lines. The meanders are made by evaporating a 30/250 nm Cr/Au film onto the entire surface of the sapphire plate. They are then defined with photolithography and subsequently etched to remove unwanted metals. Finally, the sapphire plate with evaporated meanders are then annealed at high temperatures. The recipe can be found in Angela's thesis, Ref. [126], and also on the QDev wiki.

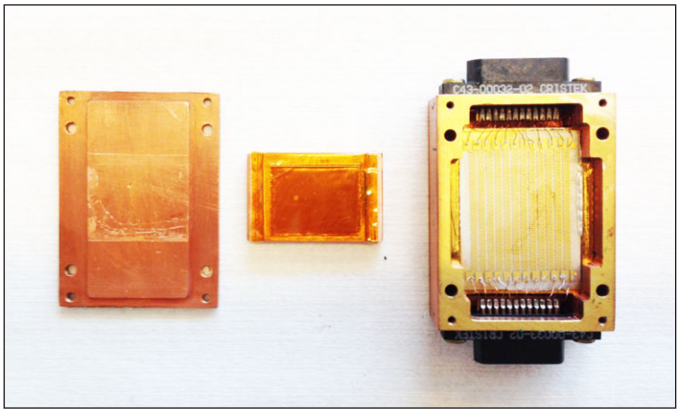

Figure B.8: Photo of disassembled sapphire filter box. The sapphire plate with photolithographically defined meanders are glued to the spine of the copper box with silver paint. An additional press-plate (object in the middle) is sandwiched between the lid (leftmost object) and the sapphire, thereby applying pressure to the sapphire plate.

The fabricated sapphire plate is then attached to the copper box with conductive silver paint (from SPI supplies®). It is important to let the silver paint dry completely. In general, we bake the glued assembly on a hotplate at 60 degrees C overnight.

To electrically connect the meanders to the mini D-sub connectors, we wirebond between the bondpads on the sapphire plate and the top of the U-shaped pins of the D-sub connector. This is an extremely tricky process and it is a fantastic exercise in patience and dexterity. It suffices to say that one can consider oneself an expert at wirebonding after making at least 48 bonds between the bondpads and the D-sub connector pins. Unfortunately, the sapphire box in Fig. B.8 is not an example of extreme wirebonding. Instead, the bondpads on the sapphire plate were connected with wires and silver paint.

Traditionally, the biggest problem with sapphire boxes is the tendency for the silver paint to crack after multiple thermal cycles. To counter this problem, Angela improved the design and added a copper press to the sapphire box assembly (the object in the center of Fig. B.8). The press is slightly thicker than the available space between the copper lid and the sapphire plate, so it applies an even pressure on the sapphire plate when the box is fully assembled. To prevent the copper press from electrically shorting the different meanders, we add Kapton tape to its surface.

B.6 Copper thermalization posts

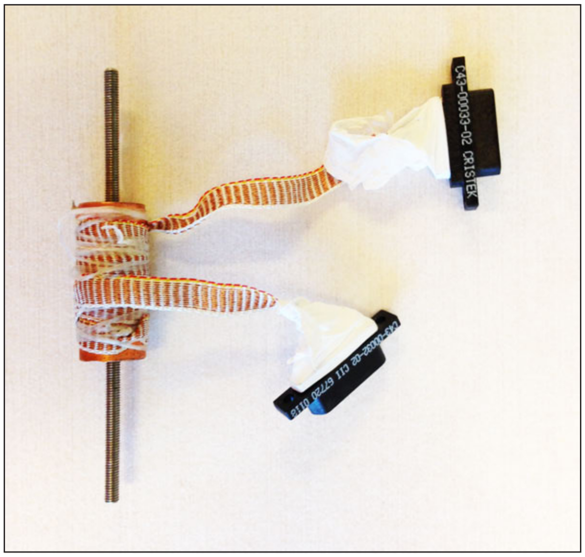

Figure B.9: Photo of a copper thermalization post. A DC loom is coiled around a high conductivity copper post and then lathered in GE varnish.

At higher stages in the fridge, we use high-conductivity copper posts to thermalize the electrons. We wrap constantan looms around the copper posts and set them in place with GE varnish (very effective for cryogenic heat-sinking). Tying dental floss to the copper posts further stabilizes the loom wrapping. Mini D-sub connectors are then soldered to both ends of the loom to make the whole copper thermalization post modular. An example of the final product is shown in Fig. B.9 (the posts are usually longer than this particular example).

Bibliography

[1] R. Holm and W. Meissner, *Einige kontaktwiderstandsmessungen bei tiefen temperaturen*, Z. Phys. **86**, 787 (1933).

[2] H. Meissner, *Superconductivity of contacts with interposed barriers*, Phys. Rev. **117**, 672 (1960).

[3] L. Fu and C. L. Kane, *Superconducting proximity effect and Majorana fermions at the surface of a topological insulator*, Phys. Rev. Lett. **100**, 096407 (2008).

[4] L. Fu and C. L. Kane, *Josephson current and noise at a superconductor/quantum-spin-Hall-insulator/superconductor junction*, Phys. Rev. B **79**, 161408 (2009).

[5] A. Cook and M. Franz, *Majorana fermions in a topological-insulator nanowire proximity-coupled to an s-wave superconductor*, Phys. Rev. B **84**, 201105 (2011).

[6] A. Y. Kitaev, *Unpaired Majorana fermions in quantum wires*, Phys. Usp. **44**, 131 (2001).

[7] R. M. Lutchyn, J. D. Sau, and S. Das Sarma, *Majorana fermions and a topological phase transition in semiconductor-superconductor heterostructures*, Phys. Rev. Lett. **105**, 077001 (2010).

[8] Y. Oreg, G. Refael, and F. von Oppen, *Helical liquids and Majorana bound states in quantum wires*, Phys. Rev. Lett. **105**, 177002 (2010).

[9] J. D. Sau, R. M. Lutchyn, S. Tewari, and S. Das Sarma, *Generic new platform for topological quantum computation using semiconductor heterostructures*, Phys. Rev. Lett. **104**, 040502 (2010).

[10] J. Alicea, *Majorana fermions in a tunable semiconductor device*, Phys. Rev. B **81**, 125318 (2010).

[11] A. Kitaev, *Fault-tolerant quantum computation by anyons*, Ann. Phys. **303**, 2 (2003).

[12] C. Nayak, S. H. Simon, A. Stern, M. Freedman, and S. Das Sarma, *Non-Abelian anyons and topological quantum computation*, Rev. Mod. Phys. **80**, 1083 (2008).

[13] J. Alicea, Y. Oreg, G. Refael, F. von Oppen, and M. P. A. Fisher, *Non-abelian statistics and topological quantum information processing in 1D wire networks*, Nat. Phys. **7**, 412 (2011).

[14] J. D. Sau, S. Tewari, and S. Das Sarma, *Universal quantum computation in a semiconductor quantum wire network*, Phys. Rev. A **82**, 052322 (2010).

[15] B. van Heck, A. R. Akhmerov, F. Hassler, M. Burrello, and C. W. J. Beenakker, *Coulomb-assisted braiding of Majorana fermions in a Josephson junction array*, New J. Phys. **14**, 035019 (2012).

[16] C. Nayak, S. H. Simon, A. Stern, M. Freedman, and S. Das Sarma, *Non-Abelian anyons and topological quantum computation*, Rev. Mod. Phys. **80**, 1083 (2008).

[17] F. Wilczek, *Majorana returns*, Nat. Phys. **5**, 614 (2009).

[18] V. Mourik, K. Zuo, S. M. Frolov, S. R. Plissard, E. P. A. M. Bakkers, and L. P. Kouwenhoven, *Signatures of Majorana fermions in hybrid superconductor-semiconductor nanowire devices*, Science **336**, 1003 (2012).

[19] A. Das, Y. Ronen, Y. Most, Y. Oreg, M. Heiblum, and H. Shtrikman, *Zero-bias peaks and splitting in an Al-InAs nanowire topological superconductor as a signature of Majorana fermions*, Nat. Phys. **8**, 887 (2012).

[20] M. T. Deng, C. L. Yu, G. Y. Huang, M. Larsson, P. Caroff, and H. Q. Xu, *Anomalous zero-bias conductance peak in a Nb-InSb nanowire-Nb hybrid device*, Nano Lett. **12**, 6414 (2012).

[21] A. D. K. Finck, D. J. Van Harlingen, P. K. Mohseni, K. Jung, and X. Li, *Anomalous modulation of a zero-bias peak in a hybrid nanowire-superconductor device*, Phys. Rev. Lett. **110**, 126406 (2013).

[22] H. O. H. Churchill, V. Fatemi, K. Grove-Rasmussen, M. T. Deng, P. Caroff, H. Q. Xu, and C. M. Marcus, *Superconductor-nanowire devices from tunneling to the multichannel regime: Zero-bias oscillations and magnetoconductance crossover*, Phys. Rev. B **87**, 241401 (2013).

[23] M. T. Björk, A. Fuhrer, A. E. Hansen, M. W. Larsson, L. E. Fröberg, and L. Samuelson, *Tunable effective g factor in InAs nanowire quantum dots*, Phys. Rev. B **72**, 201307 (2005).

[24] Y. A. Bychkov and E. I. Rashba, *Oscillatory effects and the magnetic susceptibility of carriers in inversion layers*, J. Phys. C Solid State **17**, 6039 (1984).

[25] S. Estévez Hernández, M. Akabori, K. Sladek, C. Volk, S. Alagha, H. Hardtdegen, M. G. Pala, N. Demarina, D. Grützmacher, and T. Schäpers, *Spin-orbit coupling and phase coherence in InAs nanowires*, Phys. Rev. B **82**, 235303 (2010).

[26] D. Liang and X. P. Gao, *Strong tuning of Rashba spinorbit interaction in single InAs nanowires*, Nano Lett. **12**, 3263 (2012).

[27] A. E. Hansen, M. T. Björk, C. Fasth, C. Thelander, and L. Samuelson, *Spin relaxation in InAs nanowires studied by tunable weak antilocalization*, Phys. Rev. B **71**, 205328 (2005).

[28] C. Fasth, A. Fuhrer, L. Samuelson, V. N. Golovach, and D. Loss, *Direct measurement of the spin-orbit interaction in a two-electron InAs nanowire quantum dot*, Phys. Rev. Lett. **98**, 266801 (2007).

[29] S. Nadj-Perge, S. M. Frolov, E. P. A. M. Bakkers, and L. P. Kouwenhoven, *Spin-orbit qubit in a semiconductor nanowire*, Nature **468** (2010).

[30] Y.-J. Doh, J. A. van Dam, A. L. Roest, E. P. A. M. Bakkers, L. P. Kouwenhoven, and S. De Franceschi, *Tunable supercurrent through semiconductor nanowires*, Science **309**, 272 (2005).

[31] L. O. Olsson, C. B. M. Andersson, M. C. Håkansson, J. Kanski, L. Ilver, and U. O. Karlsson, *Charge accumulation at InAs surfaces*, Phys. Rev. Lett. **76**, 3626 (1996).

[32] C. A. Mead and W. G. Spitzer, *Fermi level position at semiconductor surfaces*, Phys. Rev. Lett. **10**, 471 (1963).

[33] D. B. Suyatin, C. Thelander, M. T. Björk, I. Maximov, and L. Samuelson, *Sulfur passivation for ohmic contact formation to InAs nanowires*, Nanotechnology **18**, 105307 (2007).

[34] S. Abay, D. Persson, H. Nilsson, H. Q. Xu, M. Fogelstrm, V. Shumeiko, and P. Delsing, *Quantized conductance and its correlation to the supercurrent in a nanowire connected to superconductors*, Nano Lett. **13**, 3614 (2013).

[35] N. L. B. Ziino, P. Krogstrup, M. H. Madsen, E. Johnson, J. B. Wagner, C. M. Marcus, J. Nygård, and T. S. Jespersen, *Epitaxial aluminum contacts to InAs nanowires*, ArXiv e-prints (2013).

[36] E. J. H. Lee, X. Jiang, M. Houzet, R. Aguado, C. M. Lieber, and S. De Franceschi, *Spin-resolved Andreev levels and parity crossings in hybrid superconductor-semiconductor nanostructures*, Nat. Nanotechnol. **9**, 79 (2014).

[37] R. M. Lutchyn, T. D. Stanescu, and S. Das Sarma, *Search for Majorana fermions in multiband semiconducting nanowires*, Phys. Rev. Lett. **106**, 127001 (2011).

[38] M. Tinkham, *Introduction to Superconductivity: Second Edition*, Dover Books on Physics (Dover Publications, 2004).

[39] T. Klapwijk, *Proximity effect from an Andreev perspective*, J. Supercond. **17**, 593 (2004).

[40] B. Pannetier and H. Courtois, *Andreev reflection and proximity effect*, J. Low Temp. Phys. **118**, 599 (2000).

[41] C. Beenakker, *Three "universal" mesoscopic Josephson effects*, in *Transport Phenomena in Mesoscopic Systems*, edited by H. Fukuyama and T. Ando, Springer Series in Solid-State Sciences, Vol. 109, 235–253 (Springer Berlin Heidelberg, 1992).

[42] C. Beenakker and H. van Houten, *The superconducting quantum point contact*, in *Nanostructures and Mesoscopic Systems*, edited by W. P. Kirk and M. A. Reed, 481 – 497 (Academic Press, 1992).

[43] L. Bretheau, *Localized excitations in superconducting atomic contacts: Probing the Andreev doublet*, Ph.D. thesis, CEA-Saclay (2013).

[44] G. E. Blonder, M. Tinkham, and T. M. Klapwijk, *Transition from metallic to tunneling regimes in superconducting microconstrictions: Excess current, charge imbalance, and supercurrent conversion*, Phys. Rev. B **25**, 4515 (1982).

[45] J. C. Hammer, J. C. Cuevas, F. S. Bergeret, and W. Belzig, *Density of states and supercurrent in diffusive SNS junctions: Roles of nonideal interfaces and spin-flip scattering*, Phys. Rev. B **76**, 064514 (2007).

[46] T. Klapwijk, G. Blonder, and M. Tinkham, *Explanation of subharmonic energy gap structure in superconducting contacts*, Physica B & C **109 110, Part 3**, 1657 (1982), 16th International Conference on Low Temperature Physics.

[47] E. N. Bratus', V. S. Shumeiko, and G. Wendin, *Theory of subharmonic gap structure in superconducting mesoscopic tunnel contacts*, Phys. Rev. Lett. **74**, 2110 (1995).

[48] J. Xiang, A. Vidan, M. Tinkham, R. M. Westervelt, and C. M. Lieber, *Ge/Si nanowire mesoscopic Josephson junctions*, Nat. Nanotechnol. **1**, 208 (2006).

[49] G. Eilenberger, *Transformation of Gorkov's equation for type II superconductors into transport-like equations*, Z. Phys. **214**, 195 (1968).

[50] K. D. Usadel, *Generalized diffusion equation for superconducting alloys*, Phys. Rev. Lett. **25**, 507 (1970).

[51] W. L. McMillan, *Tunneling model of the superconducting proximity effect*, Phys. Rev. **175**, 537 (1968).

[52] A. A. Golubov and M. Y. Kupriyanov, *Josephson effect in SNlNS and SNIS tunnel structures with finite transparency of the sn boundaries*, Zh. Éksp. Teor. Fiz. **96**, 1420 (1989).

[53] W. Belzig, C. Bruder, and G. Schön, *Local density of states in a dirty normal metal connected to a superconductor*, Phys. Rev. B **54**, 9443 (1996).

[54] W. Belzig, F. K. Wilhelm, C. Bruder, G. Schön, and A. D. Zaikin, *Quasiclassical green's function approach to mesoscopic superconductivity*, Superlattice Microst. **25**, 1251 (1999).

[55] D. A. Ivanov, R. von Roten, and G. Blatter, *Minigap in a long disordered SNS junction: Analytical results*, Phys. Rev. B **66**, 052507 (2002).

[56] S. Guéron, H. Pothier, N. O. Birge, D. Esteve, and M. H. Devoret, *Superconducting proximity effect probed on a mesoscopic length scale*, Phys. Rev. Lett. **77**, 3025 (1996).

[57] N. Moussy, H. Courtois, and B. Pannetier, *Local spectroscopy of a proximity superconductor at very low temperature*, Europhys. Lett. **55**, 861 (2001).

[58] L. Serrier-Garcia, J. C. Cuevas, T. Cren, C. Brun, V. Cherkez, F. Debontridder, D. Fokin, F. S. Bergeret, and D. Roditchev, *Scanning tunneling spectroscopy study of the proximity effect in a disordered two-dimensional metal*, Phys. Rev. Lett. **110**, 157003 (2013).

[59] W. Chang, V. E. Manucharyan, T. S. Jespersen, J. Nygård, and C. M. Marcus, *Tunneling spectroscopy of quasiparticle bound states in a spinful Josephson junction*, Phys. Rev. Lett. **110**, 217005 (2013).

[60] F. Zhou and B. Spivak, *Resistance of superconductor-normal-metal-superconductor (SNS) junctions*, J. Exp. Theor. Phys. Lett. **65**, 369 (1997).

[61] H. le Sueur, P. Joyez, H. Pothier, C. Urbina, and D. Esteve, *Phase controlled superconducting proximity effect probed by tunneling spectroscopy*, Phys. Rev. Lett. **100**, 197002 (2008).

[62] J. Reutlinger, L. Glazman, Y. V. Nazarov, and W. Belzig, *"Smile" gap in the density of states of a cavity between superconductors*, Phys. Rev. Lett. **112**, 067001 (2014).

[63] A. Levchenko, *Crossover in the local density of states of mesoscopic superconductor/normal-metal/superconductor junctions*, Phys. Rev. B **77**, 180503 (2008).

[64] E. Vecino, A. Martín-Rodero, and A. L. Yeyati, *Josephson current through a correlated quantum level: Andreev states and π junction behavior*, Phys. Rev. B **68**, 035105 (2003).

[65] T. Domański and A. Donabidowicz, *Interplay between particle-hole splitting and the Kondo effect in quantum dots*, Phys. Rev. B **78**, 073105 (2008).

[66] T. Meng, S. Florens, and P. Simon, *Self-consistent description of Andreev bound states in Josephson quantum dot devices*, Phys. Rev. B **79**, 224521 (2009).

[67] A. Martín-Rodero and A. Levy Yeyati, *Josephson and Andreev transport through quantum dots*, Adv. Phys. **60**, 899 (2011).

[68] M. Grobis, I. G. Rau, R. M. Potok, and D. Goldhaber-Gordon, *Kondo effect in mesoscopic quantum dots*, eprint arXiv:cond-mat/0611480 (2006).

[69] L. Yu, *Bound state in superconductors with paramagnetic impurities*, Acta Phys. Sin. **21**, 75 (1965).

[70] H. Shiba, *Classical spins in superconductors*, Prog. Theor. Phys. **40**, 435 (1968).

[71] A. I. Rusinov, *Theory of gapless superconductivity in alloys containing paramagnetic impurities*, Sov. Phys., JETP **29**, 1101 (1969).

[72] S. de Franceschi, L. Kouwenhoven, C. Schonenberger, and W. Wernsdorfer, *Hybrid superconductor-quantum dot devices*, Nat. Nanotechnol. **5**, 703 (2010).

[73] D. Goldhaber-Gordon, H. Shtrikman, D. Mahalu, D. Abusch-Magder, U. Meirav, and M. A. Kastner, *Kondo effect in a single-electron transistor*, Nature **391**, 156 (1998).

[74] A. V. Balatsky, I. Vekhter, and J.-X. Zhu, *Impurity-induced states in conventional and unconventional superconductors*, Rev. Mod. Phys. **78**, 373 (2006).

[75] T. Soda, T. Matsuura, and Y. Nagaoka, *s-d Exchange interaction in a superconductor*, Prog. Theor. Phys. **38**, 551 (1967).

[76] H. Shiba and T. Soda, *Superconducting tunneling through the barrier with paramagnetic impurities*, Prog. Theor. Phys. **41**, 25 (1969).

[77] K. Satori, H. Shiba, O. Sakai, and Y. Shimizu, *Numerical renormalization group study of magnetic impurities in superconductors*, J. Phys. Soc. Jpn **61**, 3239 (1992).

[78] J. Simonin and R. Allub, *Rare-earth impurity in a superconductive matrix*, Phys. Rev. Lett. **74**, 466 (1995).

[79] J. Bauer, A. Oguri, and A. C. Hewson, *Spectral properties of locally correlated electrons in a Bardeen Cooper Schrieffer superconductor*, J. Phys-Condens. Mat. **19**, 486211 (2007).

[80] K. J. Franke, G. Schulze, and J. I. Pascual, *Competition of superconducting phenomena and Kondo screening at the nanoscale*, Science **332**, 940 (2011).

[81] M. R. Buitelaar, T. Nussbaumer, and C. Schönenberger, *Quantum dot in the Kondo regime coupled to superconductors*, Phys. Rev. Lett. **89**, 256801 (2002).

[82] L. I. Glazman and K. A. Matveev, *Resonant Josephson current through Kondo impurities in a tunnel barrier*, JETP Lett. **49**, 659 (1989).

[83] B. I. Spivak and S. A. Kivelson, *Negative local superfluid densities: The difference between dirty superconductors and dirty Bose liquids*, Phys. Rev. B **43**, 3740 (1991).

[84] A. V. Rozhkov, D. P. Arovas, and F. Guinea, *Josephson coupling through a quantum dot*, Phys. Rev. B **64**, 233301 (2001).

[85] A. V. Rozhkov and D. P. Arovas, *Interacting-impurity Josephson junction: Variational wave functions and slave-boson mean-field theory*, Phys. Rev. B **62**, 6687 (2000).

[86] Y. Tanaka, A. Oguri, and A. C. Hewson, *Kondo effect in asymmetric Josephson couplings through a quantum dot*, New J. Phys. **9**, 115 (2007).

[87] J. A. van Dam, Y. V. Nazarov, E. P. A. M. Bakkers, S. De Franceschi, and L. P. Kouwenhoven, *Supercurrent reversal in quantum dots*, Nature **442**, 667 (2006).

[88] J. P. Cleuziou, W. Wernsdorfer, V. Bouchiat, T. Ondarçuhu, and M. Monthioux, *Carbon nanotube superconducting quantum interference device*, Nat. Nanotechnol. **1**, 53 (2006).

[89] H. I. Jørgensen, T. Novotný, K. Grove-Rasmussen, K. Flensberg, and P. E. Lindelof, *Critical current 0-π transition in designed Josephson quantum dot junctions*, Nano Lett. **7**, 2441 (2007).

[90] A. Eichler, R. Deblock, M. Weiss, C. Karrasch, V. Meden, C. Schönenberger, and H. Bouchiat, *Tuning the Josephson current in carbon nanotubes with the Kondo effect*, Phys. Rev. B **79**, 161407 (2009).

[91] R. Maurand, T. Meng, E. Bonet, S. Florens, L. Marty, and W. Wernsdorfer, *First-order 0-π quantum phase transition in the Kondo regime of a superconducting carbon-nanotube quantum dot*, Phys. Rev. X **2**, 011009 (2012).

[92] D. J. Luitz, F. F. Assaad, T. Novotný, C. Karrasch, and V. Meden, *Understanding the Josephson current through a Kondo-correlated quantum dot*, Phys. Rev. Lett. **108**, 227001 (2012).

[93] T. Dirks, T. L. Hughes, S. Lal, B. Uchoa, Y.-F. Chen, C. Chialvo, P. M. Goldbart, and N. Mason, *Transport through Andreev bound states in a graphene quantum dot*, Nat. Phys. **7**, 386 (2011).

[94] R. S. Deacon, Y. Tanaka, A. Oiwa, R. Sakano, K. Yoshida, K. Shibata, K. Hirakawa, and S. Tarucha, *Tunneling spectroscopy of Andreev energy levels in a quantum dot coupled to a superconductor*, Phys. Rev. Lett. **104**, 076805 (2010).

[95] R. S. Deacon, Y. Tanaka, A. Oiwa, R. Sakano, K. Yoshida, K. Shibata, K. Hirakawa, and S. Tarucha, *Kondo-enhanced Andreev transport in single self-assembled InAs quantum dots contacted with normal and superconducting leads*, Phys. Rev. B **81**, 121308 (2010).

[96] E. J. H. Lee, X. Jiang, R. Aguado, G. Katsaros, C. M. Lieber, and S. De Franceschi, *Zero-bias anomaly in a nanowire quantum dot coupled to superconductors*, Phys. Rev. Lett. **109**, 186802 (2012).

[97] J.-D. Pillet, C. H. L. Quay, P. Morfin, C. Bena, A. L. Yeyati, and P. Joyez, *Andreev bound states in supercurrent-carrying carbon nanotubes revealed*, Nat. Phys. **6**, 965 (2010).

[98] T. S. Jespersen, M. Aagesen, C. Sørensen, P. E. Lindelof, and J. Nygård, *Kondo physics in tunable semiconductor nanowire quantum dots*, Phys. Rev. B **74**, 233304 (2006).

[99] A. V. Kretinin, H. Shtrikman, D. Goldhaber-Gordon, M. Hanl, A. Weichselbaum, J. von Delft, T. Costi, and D. Mahalu, *Spin-1/2 Kondo effect in an InAs nanowire quantum dot: Unitary limit, conductance scaling, and Zeeman splitting*, Phys. Rev. B **84**, 245316 (2011).

[100] C. H. L. Quay, J. Cumings, S. J. Gamble, R. d. Picciotto, H. Kataura, and D. Goldhaber-Gordon, *Magnetic field dependence of the spin-1/2 and spin-1 Kondo effects in a quantum dot*, Phys. Rev. B **76**, 245311 (2007).

[101] V. Koerting, B. M. Andersen, K. Flensberg, and J. Paaske, *Nonequilibrium transport via spin-induced subgap states in superconductor/quantum dot/normal metal cotunnel junctions*, Phys. Rev. B **82**, 245108 (2010).

[102] A. V. Rozhkov and D. P. Arovas, *Josephson coupling through a magnetic impurity*, Phys. Rev. Lett. **82**, 2788 (1999).

[103] A. Oguri, Y. Tanaka, and J. Bauer, *Interplay between Kondo and Andreev-Josephson effects in a quantum dot coupled to one normal and two superconducting leads*, Phys. Rev. B **87**, 075432 (2013).

[104] D. Goldhaber-Gordon, J. Göres, M. A. Kastner, H. Shtrikman, D. Mahalu, and U. Meirav, *From the Kondo regime to the mixed-valence regime in a single-electron transistor*, Phys. Rev. Lett. **81**, 5225 (1998).

[105] S. Takei, B. M. Fregoso, H.-Y. Hui, A. M. Lobos, and S. Das Sarma, *Soft superconducting gap in semiconductor Majorana nanowires*, Phys. Rev. Lett. **110**, 186803 (2013).

[106] T. D. Stanescu, R. M. Lutchyn, and S. Das Sarma, *Soft superconducting gap in semiconductor-based Majorana nanowires*, ArXiv e-prints (2013).

[107] D. Rainis and D. Loss, *Majorana qubit decoherence by quasiparticle poisoning*, Phys. Rev. B **85**, 174533 (2012).

[108] M. Cheng, R. M. Lutchyn, and S. Das Sarma, *Topological protection of Majorana qubits*, Phys. Rev. B **85**, 165124 (2012).

[109] P. Krogstrup, J. Yamasaki, C. B. Sørensen, E. Johnson, J. B. Wagner, R. Pennington, M. Aagesen, N. Tanaka, and J. Nygrd, *Junctions in axial III-V heterostructure nanowires obtained via an interchange of group III elements*, Nano Lett. **9**, 3689 (2009), pMID: 19842690.

[110] C. W. J. Beenakker, *Quantum transport in semiconductor-superconductor microjunctions*, Phys. Rev. B **46**, 12841 (1992).

[111] A. F. Andreev, *Thermal conductivity of the intermediate state of superconductors*, Soviet Phys., JETP **46**, 1823 (1964).

[112] S. Chuang, Q. Gao, R. Kapadia, A. C. Ford, J. Guo, and A. Javey, *Ballistic InAs nanowire transistors*, Nano Lett. **13**, 555 (2013).

[113] A. C. Ford, S. B. Kumar, R. Kapadia, J. Guo, and A. Javey, *Observation of degenerate one-dimensional sub-bands in cylindrical InAs nanowires*, Nano Lett. **12**, 1340 (2012).

[114] O. Wunnicke, *Gate capacitance of back-gated nanowire field-effect transistors*, Appl. Phys. Lett. **89**, 083102 (2006).

[115] Y.-J. Doh, J. A. van Dam, A. L. Roest, E. P. A. M. Bakkers, L. P. Kouwenhoven, and S. De Franceschi, *Tunable supercurrent through semiconductor nanowires*, Science **309**, 272 (2005).

[116] T. S. Jespersen, M. L. Polianski, C. B. Sørensen, K. Flensberg, and J. Nygård, *Mesoscopic conductance fluctuations in InAs nanowire-based SNS junctions*, New J. Phys. **11**, 113025 (2009).

[117] R. C. Dynes and T. A. Fulton, *Supercurrent density distribution in Josephson junctions*, Phys. Rev. B **3**, 3015 (1971).

[118] L. D. Landau, *Theory of superconductivity*, Phys. Z. Sowjet **11**, 129 (1937).

[119] B. Béri, J. H. Bardarson, and C. W. J. Beenakker, *Splitting of Andreev levels in a Josephson junction by spin-orbit coupling*, Phys. Rev. B **77**, 045311 (2008).

[120] M. Wimmer, A. R. Akhmerov, J. P. Dahlhaus, and C. W. J. Beenakker, *Quantum point contact as a probe of a topological superconductor*, New J. Phys. **13**, 053016 (2011).

[121] W. A. Little and R. D. Parks, *Observation of quantum periodicity in the transition temperature of a superconducting cylinder*, Phys. Rev. Lett. **9**, 9 (1962).

[122] I. Sternfeld, E. Levy, M. Eshkol, A. Tsukernik, M. Karpovski, H. Shtrikman, A. Kretinin, and A. Palevski, *Magnetoresistance oscillations of superconducting Al-film cylinders covering InAs nanowires below the quantum critical point*, Phys. Rev. Lett. **107**, 037001 (2011).

[123] A. Altland and M. R. Zirnbauer, *Nonstandard symmetry classes in mesoscopic normal-superconducting hybrid structures*, Phys. Rev. B **55**, 1142 (1997).

[124] A. Altland and M. R. Zirnbauer, *Random matrix theory of a chaotic Andreev quantum dot*, Phys. Rev. Lett. **76**, 3420 (1996).

[125] R. Barends, J. Wenner, M. Lenander, Y. Chen, R. C. Bialczak, J. Kelly, E. Lucero, P. O'Malley, M. Mariantoni, D. Sank, H. Wang, T. C. White, Y. Yin, J. Zhao, A. N. Cleland, J. M. Martinis, and J. J. A. Baselmans, *Minimizing quasiparticle generation from stray infrared light in superconducting quantum circuits*, Appl. Phys. Lett. **99**, 113507 (2011).

[126] A. Kou, *Microscopic properties of the fractional quantum Hall effect*, Ph.D. thesis, Harvard University (2013).

[127] F. Pobell, *Matter and methods at low temperatures*, Vol. 2 (Springer, 1996).

[128] J. B. Miller, I. P. Radu, D. M. Zumbuhl, E. M. Levenson-Falk, M. A. Kastner, C. M. Marcus, L. N. Pfeiffer, and K. W. West, *Fractional quantum Hall effect in a quantum point contact at filling fraction 5/2*, Nat. Phys. **3**, 561 (2007).

[129] J. M. Martinis, M. H. Devoret, and J. Clarke, *Experimental tests for the quantum behavior of a macroscopic degree of freedom: The phase difference across a Josephson junction*, Phys. Rev. B **35**, 4682 (1987).

[130] A. Fukushima, A. Sato, A. Iwasa, Y. Nakamura, T. Komatsuzaki, and Y. Sakamoto, *Attenuation of microwave filters for single-electron tunneling experiments*, IEEE T Instrum. Meas. **46**, 289 (1997).

[131] K. Bladh, D. Gunnarsson, E. Hürfeld, S. Devi, C. Kristoffersson, B. Smålander, S. Pehrson, T. Claeson, P. Delsing, and M. Taslakov, *Comparison of cryogenic filters for use in single electronics experiments*, Rev. Sci. Instrum. **74**, 1323 (2003).

[132] F. Milliken, J. Rozen, G. Keefe, and R. Koch, *50 Ω characteristic impedance low-pass metal powder filters*, Rev. Sci. Instrum. **78**, 024701 (2007).

[133] A. Lukashenko and A. Ustinov, *Improved powder filters for qubit measurements*, Rev. Sci. Instrum. **79**, 014701 (2008).